UNIVERSITY OF CALIFORNIA SAN DIEGO

Addressing complexity of materials behavior under extreme dynamic conditions using numerical modeling

A dissertation submitted in partial satisfaction of the
requirements for the degree Doctor of Philosophy

in

Engineering Sciences (Applied Mechanics)

by

Pedro Franco Navarro

Committee in charge:

Professor Vitali F. Nesterenko, Chair
Professor David J. Benson, Co-Chair
Professor Prabhakar Bandaru
Professor Yuri Bazilevs
Professor Katja Lindenberg

2018

The Dissertation of Pedro Franco Navarro is approved, and it is acceptable in quality and form for publication on microfilm and electronically:

Co-Chair

Chair

University of California San Diego

2018

DEDICATION

For all their support, I dedicate this work to my loved ones: My father Pedro, my mother Cuquita, my sisters Haydee and Ingrid and my girlfriend Caitlin, without them this would have been impossible.

TABLE OF CONTENTS

Signature page iii

Dedication iv

Table of contents v

List of figures ix

List of tables xxi

Acknowledgements xxii

Vita xxiv

Abstract of the dissertation xxv

Chapter 1 : Introduction 1

1.1 Chapter References 5

Chapter 2 : Nature of short, high-amplitude compressive stress pulses in a periodic dissipative laminate 8

2.1 Introduction 8

2.2 Simulations 16

2.3 Results of Numerical Simulations 22

2.3.1 2 + 2 Al-W laminate, impact by 8-mm Al plate 23

2.3.2 2 + 2 Al-W laminate with artificially small Y_{max}, impact by 8-mm Al plate 26

2.3.3 1 + 1 Al-W laminate, impact by 8-mm Al plate 33

2.3.4 1 + 1 Al-W laminate with artificially small Y_{max}, impact by 8-mm Al plate 36

2.3.5 0.5 + 0.5 Al-W laminate, impact by 8-mm Al plate 37

2.3.6 2 + 2 Al-W laminate, Al impactor with thickness of 2 mm 41

2.3.7 1 + 1 Al-W laminate, impact by 2-mm Al plate 44

2.3.8 0.5 + 0.5 Al-W laminate, impact by 2-mm Al plate 46

2.3.9 Comparison of solitarylike wave shapes created by different initial conditions 49

2.3.10 Head-on collision of solitarylike waves 51

2.4 Theoretical Approach 55

2.5 Chapter conclusions 67

2.6 Chapter references 69

Chapter 3 : Multiple scales of shock waves in dissipative laminate materials 73

3.1 Introduction 73

3.2 Simulations 79

3.3 Results of numerical calculations 81

3.3.1 A 2+2 laminate impacted by an 80-mm Al flyer plate (t_r=25) ... 82

3.3.2 A 2+2 laminate impacted by an 800-mm Al flyer plate (t_r=254) 86

3.3.3 A 1+1 laminate impacted by an 80-mm Al flyer plate (tr=51) ... 90

3.3.4 A 1+1 laminate impacted by an 800-mm Al flyer plate (tr=508) ... 94

3.3.5 A 0.5+0.5 laminate impacted by an 80-mm Al flyer plate (tr=102) ... 97

3.3.6 A 0.5+0.5 laminate impacted by an 800-mm Al flyer plate (tr=1016) ... 99

3.4 Scaling of shockwave parameters using the dissipative KdV equation ... 103

3.5 Chapter conclusions ... 113

3.6 Chapter references ... 114

Chapter 4 : Instability in the collapse of highly heterogeneous mixtures ... 117

4.1 Introduction ... 117

4.2 Experiments ... 120

4.3 Numerical Simulations ... 128

4.4 Chapter Conclusions ... 143

4.5 Chapter References ... 145

Chapter 5 : Shear band patterning and post-critical behavior in AISI 4340 steel with different microstructure ... 149

5.1 Introduction ... 149

5.2 Experimental procedures and results 153

5.3 Numerical calculations.....165

5.3.1 Influence of the number of defects on shear localization and post-critical behavior of AISI 4340.....170

5.3.2 Shear localization and post-critical behavior of heat treated AISI 4340 175

5.4 Chapter conclusions 180

5.5 Chapter references.....182

Chapter 6 : Conclusions.....188

LIST OF FIGURES

Figure 2-1: Geometry of the Laminate 17

Figure 2-2: Stress pulse evolution in 2 + 2 laminate; data correspond to the interfaces of Al-W layers at different depths: (a) 0, 4, 8, and 12 mm; (b) 68, 72, 76, and 80 mm; (c) 140, 144, 148, and 152 mm; (d) 208, 212, 216, and 220 mm. The pulse was generated by the impact.....24

Figure 2-3: Stress pulse evolution in 2+2 laminate with artificially small $Ymax$; data correspond to the interfaces of Al-W layers at different depths: (a) 0, 4, 8, and 12 mm; (b) 68, 72, 76, and 80 mm; (c) 140, 144, 148, and 152 mm; (d) 208, 212, 216, and 220 mm. 27

Figure 2-4: Stress pulse evolution in 2 + 2 laminate; data correspond to the interfaces of Al-W layers at different depths: (a) 0, 4, 8, and 12 mm; (b) 68, 72, 76, and 80 mm; (c) 140, 144, 148, and 152 mm; (d) 208, 212, 216, and 220 mm.The pulse was generated by the impact.....29

Figure 2-5: Comparison of wave shape at same stress amplitude of 58 GPa generated by the impact of an Al plate with thickness 8 mm for the case of a 2 + 2 laminate with real dissipative properties, laminate with an artificially small $Ymax$, and laminate with elastic behavior. 30

Figure 2-6: Comparison of attenuating stress traveling waves generated by the impact of an Al plate with 8 mm thickness in a 2 + 2 laminate and their corresponding temperatures in Al layer: (a, c) Laminate with real material properties and (b, d) laminate with an artificially small $Ymax$.....31

Figure 2-7: Stress pulse evolution in 1 + 1 laminate; data correspond to the interfaces of Al-W layers at different depths: (a) 0, 4, 8, and 12 mm; (b) 68, 72, 76, and 80 mm; (c) 140, 144, 148, and 152 mm; (d) 208, 212, 216, and 220 mm. The pulse was generated by the impact.....34
Figure 2-8: Stress pulse evolution in 1+1 laminate with artificially small $Ymax$; data correspond to the interfaces of Al-W layers at different depths: (a) 0, 4, 8, and 12 mm; (b) 68, 72, 76, and 80 mm; (c) 140, 144, 148, and 152 mm; (d) 208, 212, 216, and 220 mm. The pulse was generated.....37
Figure 2-9: Stress pulse evolution in 0.5 + 0.5 laminate; data correspond to the interfaces of Al-W layers at different depths: (a) 0, 4, 8, and 12 mm; (b) 68, 72, 76, and 80 mm; (c) 140, 144, 148, and 152 mm; (d) 208, 212, 216, and 220 mm. The pulse was generated by the impact.....38
Figure 2-10: Stress pulse evolution in 2 + 2 laminate; data correspond to the interfaces of Al-W layers at different depths: (a) 0, 4, 8, and 16 mm; (b) 68, 72, 76, and 80 mm; (c) 140, 144, 148, and 152 mm; (d) 208, 212, 216, and 220 mm. The pulse was generated by the impact.....42
Figure 2-11: Comparison of shapes of solitarylike wave and leading part of the pulse both formed in 2 + 2 laminates with real dissipative properties excited by impact of an Al plate with different thickness, 2 and 8 mm, correspondingly. 43
Figure 2-12: Stress pulse evolution in 1 + 1 laminate; data correspond to the interfaces of Al-W layers at different depths: (a) 0, 4, 8, and 12 mm; (b) 68, 72, 76,

and 80 mm; (c) 140, 144, 148, and 152 mm; (d) 208, 212, 216, and 220 mm. The pulse was generated by the impact.....45
Figure 2-13: Stress pulse evolution in 0.5 + 0.5 laminate; data correspond to the interfaces of Al-W layers at different depths: (a) 0, 4, 8, and 12 mm; (b) 68, 72, 76, and 80 mm; (c) 140, 144, 148, and 152 mm; (d) 208, 212, 216, and 220 mm. The pulse was generated by the impact.....47
Figure 2-14: Comparison between the profiles of stress in solitarylike waves with similar amplitudes in Al-W laminates with different cell sizes and dissipative properties generated by two different impactors with thickness of 2 and 8 mm, respectively.....50
Figure 2-15: Laminate impacted at both ends to investigate collision of solitarylike waves.....51
Figure 2-16: (a) Traveling wave at 60 mm depth from the left end of the laminate with real properties. (b) Traveling wave at 60 mm depth from the right end of the laminate. Both waves are shown before collision.....52
Figure 2-17: Resulting pulse due to collision of two waves propagating in the opposite direction at the middle of the laminate (at 101 mm depths from both ends). 53
Figure 2-18: (a) Traveling wave at 142 mm depth from the left end of the laminate with real properties. (b) Traveling wave at 142 mm depth from the right end of the laminate. Both waves are shown after collision.....54

Figure 2-19: (a) The phase shift between two initially identical solitarylike waves created by the impact on the left end traveling the same distance of 122 mm without collision and after head-on collision; (b) the same waves are superposed to demonstrate their similar profiles. 55
Figure 2-20: Nonlinear stress-strain relations for Al (a), and W (b) based on Hugoniot curves, static compression based on third order elastic constants, zero Kelvin curves, isotherm and approximation of Hugoniot curves using terms only with second power law of strains, Eq(16).....59
Figure 2-21: Single cell with unit area made of material a and b. 60
Figure 2-22: Comparison of KdV solitary solution with nonlinearity parameters taken from Hugoniot curve (Eq.18) to the shapes of solitary like waves found on numerical simulations: (a) The wave in numerical simulation corresponding to the depth 72 mm in the 2+2 laminate.....64
Figure 2-23: Comparison of KdV solitary solution with nonlinearity parameters taken from an approximated Hugoniot curve [Eq. (16)] to the wave found on numerical simulations. 65
Figure 2-24: Dependence of the speed of the localized wave in Al-W 2+2, 1+1, and 0.5+0.5 laminates found in numerical calculations on maximum stress (on the interface between Al and W) and corresponding Eq. 33 for the speed of KdV solitary wave. 66
Figure 3-1: Three characteristic time scales related to the established stationary shock profile detected at some point inside the laminate far enough from the

impacted end. The three time scales identified in the graph are described as follows: time of propagation $t_1 – t_0$ when shock.....77
Figure 3-2: Geometry of laminate Al/W material. Black dots indicate points in Al layers adjacent to the interfaces where the stress is calculated. 80
Figure 3-3: Stress pulse evolution in 2+2 laminate impacted by 80 mm Al flyer plate at 2800 m/s at different distances from impacted end (a) 0, 4, 8 and 12 mm (b) 68, 140, 152, 220 mm. 83
Figure 3-4: 2+2 laminate impacted by 80 mm Al flyer plate at 2800 m/s (a) Maximum stress on the leading front of the shock versus distance from impacted end; (b) Leading front width versus distance from impacted end. 84
Figure 3-5: Comparison of a solitary-like wave (solid line) and leading part of a shock wave (empty dots) in the same 2+2 Al-W laminate. The solitary-like wave was created by the impact of an 8 mm Al flyer plate [7,8] while the shock wave was created by the impact of an 80-mm Al flyer plate. 85
Figure 3-6: Stress pulse evolution in 2+2 laminate impacted by 800 mm Al flyer plate at 2800 m/s at different distances from impacted end (a) 0, 4, 8 and 12 mm (b) 68, 140, 152, 220 mm. 86
Figure 3-7: 2+2 laminate impacted by 800 mm Al flyer plate at 2800 m/s (a) Maximum stress in the leading peak vs. propagation distance (b) leading front width versus propagation distance. 87
Figure 3-8: 2+2 Al laminate impacted by 800 mm Al flyer plate at 2800 m/s. (a) Shock front width vs. traveled distance (b) Superposition of stress profile and

effective plastic strain, the inflection point on the plastic strain curve (right Y-axis) indicates the point where the oscillations become purely elastic. 88
Figure 3-9: Stress pulse evolution in 1+1 laminate impacted by 80 mm Al flyer plate at 2800 m/s at different distances from impacted end (a) 0, 4, 8 and 12 mm (b) 68, 140, 152, 220 mm. Compare these profiles with the waves structure in 2+2 laminate excited by the same Al plate.....91
Figure 3-10: Establishment of the stationary amplitude in the leading front in the 1+1 laminate impacted by an 80-mm Al flyer plate at 2800 m/s: (a) maximum stress in the leading peak vs propagation distance and (b) leading front width versus propagation distance.....92
Figure 3-11: Establishment of the stationary shock front width with traveled distance in a 1+1 Al laminate impacted by an 80-mm Al flyer plate at 2800 m/s.93
Figure 3-12: Stress pulse evolution in a 1+1 laminate impacted by an 800-mm Al flyer plate with a velocity of 2800 m/s 94
Figure 3-13: (a) Maximum stress in the leading peak and (b) leading front width versus propagation distance in a 1+1 laminate impacted by an 800-mm Al flyer plate at 2800 m/s. 95
Figure 3-14: Shock front width vs traveled distance in the 1+1 Al laminate impacted by an 800-mm Al flyer plate at 2800 m/s.....96
Figure 3-15: Stress pulse evolution in a 0.5+0.5 laminate impacted by an 80-mm Al flyer plate at 2800 m/s at different distances from the impacted end: (a) 0, 4, 8, and 12 mm and (b) 68, 140, 152, and 220 mm. 97

Figure 3-16: A 0.5+0.5 laminate impacted by an 80-mm Al flyer plate at 2800 m/s: (a) maximum stress in the leading peak vs propagation distance and (b) leading front width versus propagation distance.....98
Figure 3-17: Shock front width vs traveled distance in a 0.5+0.5 Al laminate impacted by an 80-mm Al flyer plate at 2800 m/s. 99
Figure 3-18: Evolution of stress wave profiles in a 0.5+0.5 laminate impacted by an 800-mm Al flyer plate at 2800 m/s at different distances from the impacted end: (a) 0, 4, 8, and 12 mm and (b) 68, 140, 152, and 220 mm.....100
Figure 3-19: (a) Maximum stress in the leading peak vs propagation distance and (b) leading front width versus propagation distance in a 0.5+0.5 laminate impacted by an 800-mm Al flyer plate at 2800 m/s.....101
Figure 3-20: Shock front width vs traveled distance in a 0.5+0.5 laminate impacted by an 800-mm Al flyer plate at 2800 m/s.....102
Figure 3-21: Comparison of KdV solitary solution to the shape of localized stress pulse (excited by impact of 8 mm Al flyer plate) and leading part of the shock wave with similar amplitude excited by impact of 80 mm Al flyer plate and 800 mm Al flyer plate. 110
Figure 3-22: (a) Decay rate of the first part four oscillations on the leading shock on 2+2, 1+1 and 0.5+05 laminate. (b) Oscillating shock on 2+2 laminate that shows the decay of the oscillations until a quasi-equilibrium state has been reached. 112
Figure 4-1: (a) Failure of SS304L through shear band formation and interaction as presented in [22] and (b) Optical micrograph of collapsed Cu showing suppression

of shear band formation through deformation along crystal orientation as presented in [24]. 119
Figure 4-2: (a) Failure through microcracking in TWC collapsed SiC specimen (b) Mechanism of cooperative buckling in Al-W laminate cylinder. Pedro, replace (a) with pattern of shear bands. 120
Figure 4-3: Schematic configuration used to create high accuracy Al-W powder samples using Cold Isostatic Pressing with oil as pressurizing media. The base was attached to the SS tube by six screws. Top and bottom rubber plugs were secured by clamps to prevent oil penetration inside assembly during CIPing... 121
Figure 4-4: Sample after CIPing. The scale on the bottom is in millimeters. 122
Figure 4-5: Thick Walled Cylinder test assembly 123
Figure 4-6: (a) Al-coarse W sample and (b) Al-fine W sample. The central copper rod was created by the collapsed copper stopper tube. The collapse in both samples is quite stable and the cylindrical symmetry of the sample has been preserved in both inner and outer surface (compare with Figs. 1 and 2. 124
Figure 4-7: Al-coarse W sample before (a) and after (b) TWC tests, on right is the interface between the sample and copper driver tube. 125
Figure 4-8: Plastic flow of Al particles between Al grains 125
Figure 4-9: Al-fine W sample before (a) and after (b) TWC test. 126
Figure 4-10: Closer look of the Al-W composite microstructure after TWC tests: (a)-(b) Al-fine W, (b) Al-coarse W. During the collapse, soft Al particles flow around the coarse 128

Figure 4-11: Sample mesh on quarter circle with particle size 100 μm. In this case the sample is fully densified (no porosity). 129
Figure 4-12: Simulation of quarter circle Al-W powder of 400 μm in size, 70% Al 30% W by volume, sample was initially fully dense. Multiple instances of collapse are shown. 133
Figure 4-13: Plastic strain field of quarter circle Al-W powder of 400 μm in size, 70% Al 30% W by volume, initially fully dense. Multiple instances of collapse are shown. 134
Figure 4-14: Simulation of quarter circle Al-W powder of 100 μm in size, 70% Al 30% W by volume, sample was initially fully dense. Multiple instances of collapse are shown. 135
Figure 4-15: Plastic strain field of quarter circle Al-W powder of 100 μm in size, 70% Al 30% W by volume, initially fully dense. Multiple instances of collapse are shown. 136
Figure 4-16: Simulation of quarter circle Al-W powder of 40 μm in size, 70% Al 30% W by volume, sample was initially fully dense. Multiple instances of collapse are shown. 138
Figure 4-17: Plastic strain field of quarter circle Al-W powder of 40 μm in size, 70% Al 30% W by volume, initially fully dense. Multiple instances of collapse are shown. 139
Figure 4-18: Illustration of process utilized to create a sample with initial porosity 13.9% that resembles samples utilized in experiment. 140

Figure 4-19: Simulation of quarter circle Al-W powder of 100 μm in size, with initial porosity 13.9%. Multiple instances of collapse are shown. 141
Figure 4-20: Plastic strain field of quarter circle Al-W powder of 100 μm in size, with initial porosity 13.9%. Multiple instances of collapse are shown. 143
Figure 5-1: The microstructure of as-received AISI 4340 (ferrite is white and pearlite is dark gray) - (a) and hardened AISI 4340 steel with martensite microstructure- (b).....155
Figure 5-2: Pictures of the collapsed AISI 4340 samples (as-received) at a different strain in the inner surface: (a) strain 0.53, initial wall thickness of the copper stopper tube 1 mm and (b) strain 0.80, initial wall thickness of the copper stopper tube 0.5 mm. 159
Figure 5-3: Pattern of nucleating shear bands in the vicinity of the contact with copper stopper tube in collapsed AISI 4340 (as-received) samples at different values of strain in the inner surface: (a) strain 0.53, initial wall thickness of the copper stopper tube 160
Figure 5-4: Pictures of the collapsed AISI 4340 samples (hardened) at a different strain in the inner surface: (a) strain 0.56, initial wall thickness of a copper stopper tube 1 mm and (b) collapse steel sample corresponding to the initial wall thickness of a copper stopper tube 0.5 mm. 160
Figure 5-5: Microstructures of the collapsed AISI 4340 (hardened) sample with strain 0.56 in the inner surface (initial wall thickness of the stopper copper tube 1

mm). Just nucleated and well-developed shear bands are presented in (a); a white-etched nucleated shear band.....162
Figure 5-6: Microstructures of bifurcated shear band split into two transformed shear bands and later into crack, at different magnifications in the collapsed hardened AISI 4340 sample at strain in the inner surface 0.83 (initial wall thickness of the copper stopper tube 0.5 mm). Sample was etched with 2% nital.....163
Figure 5-7: Shear bands in the collapsed AISI 4340 (as-received) sample etched with 2% natal at different values of strain in the inner surface: (a) strain 0.53, initial wall thickness of the copper stopper tube 1 mm and (b) strain 0.80, initial wall thickness of copper stopper tube 0.5 mm. 164
Figure 5-8: (a) Geometry of the Thick-Walled Cylinder method (b) Pressure dependence on time corresponding to the boundary conditions used in numerical calculations. 167
Figure 5-9: Collapsed AISI 4340 steel cylinder at (a) small global strain (1 mm wall thickness copper stopper) and (b) large global strain (0.5 mm wall thickness copper stopper). The colors on right correspond to different level of effective plastic strains. 169
Figure 5-10: Total velocity of inner surface in numerical simulations of steel specimen on Thick-Walled Cylinder experiment of AISI 4340 (blue line) and heat treated 4340 (red line).....170
Figure 5-11: Fringe plots of effective plastic strain in the collapsed AISI 4340 samples with nominal properties in the majority of mesh elements and variable

percentages (a) 5%, b) 2.5%, c) 1.5%, and d) 0.5%) of mesh elements with a different initial yield strength. 172
Figure 5-12: Fringe plot of the effective plastic strain in AISI 4340 Steel with (a) 1 mm and (b) 0.5 mm wall thickness of copper stopper tube corresponding to similar outer diameter of samples to experiments (see Table 2), percentage of elements with the scaled strength 174
Figure 5-13: Fringe plot of the effective plastic strain on hardened 4340 Steel (percentage of defects 0.5%) with 1 mm wall copper stopper tube at different stages of collapse (a) 5 μs (b) 7.88 μs (same effective strain as Fig. 12(b)) (c) 10 μs. Outer diameters 177
Figure 5-14: Fringe plot of the effective plastic strain on hardened 4340 Steel (0.5% defects) with 0.5 mm wall copper stopper tube at different times (a) 5 μs (b) 8.74 μs (same effective strain as Fig. 10(b)) (c) 10 μs. Outer diameters in (a) 15.58 mm, in (b) 13.44 mm and in (c) 12.7 mm. 179

LIST OF TABLES

Table 2-1: Material Properties.....20

Table 3-1: The speed of shock waves with different amplitude, strains in their leading maximum, a final mean strain in quasi-equilibrium states, their ratio obtained in numerical calculations, theoretical values of speed for shock-like stress wave and the difference between theoretical.....108

Table 4-1: Experimental results of sample properties after processing.....122

Table 4-2: Material parameters used in numerical simulations [32-35]. 131

Table 5-1: Mechanical properties of as-received and hardened AISI4340 steels [47] 156

Table 5-2: Final diameters of the AISI 4340 samples, which have identical initial O.D. (17.02 mm) and I.D. (12.07 mm), and the corresponding effective strains (ε_{eff}). 157

Table 5-3: Material parameters for Johnson-Cook material model [54,55]. 168

ACKNOWLEDGEMENTS

I would like to thank professors Vitali Nesterenko and David Benson for their continuous guidance and patience through my studies, their support has been paramount to accomplish this tremendous step. It has been through their example, that I learned what's needed to be an excellent researcher and mentor.

To my friends in San Diego, thank you for helping me navigate some stressful times and to teach me how to better enjoy life.

To Caitlin, thanks for being an amazing partner who has unconditionally supported me through this endeavor, I cannot wait to keep enjoying the rest of my life with you.

To my family, it is extremely hard to express in words what you have helped me accomplish. Sacrifices, support and love are just three words that come to mind, but that only begins to describe it all. I love you all.

I would also like to thank CONACYT-UCMEXUS for the funding provided that made all this work possible.

Chapter 2, in full, is a reprint of the material as it appears in Physical Review E, Franco Navarro, P., Benson, D.J. and Nesterenko, V.F., American Physical Society 2015. The dissertation author was the primary investigator and author of this paper.

Chapter 3, in full, is a reprint of the material as it appears in Physical Review E, Franco Navarro, P., Benson, D.J. and Nesterenko, V.F., American Physical

Society 2016. The dissertation author was the primary investigator and author of this paper.

Chapter 4, in part is currently being prepared for submission for publication of the material. Franco Navarro, P., Benson, D.J., Nesterenko, V.F., The dissertation author was the primary investigator and author of this material.

Chapter 5, in full, is a reprint of the material as it appears in International Journal of Impact Engineering, Franco Navarro, P., Chiu, P.H., Higgins, A., Serge, M., Benson, D.J. and Nesterenko, V.F., Elsevier 2018. The dissertation author was the primary investigator and author of this paper.

VITA

2009 Bachelor of Science, Instituto Tecnológico y de Estudios Superiores de Monterrey, Monterrey.

2010 Mechanical Design Engineer, Honeywell Aerospace, Mexicali.

2011 Mechanical Design Engineer, PACCAR Inc, Mexicali.

2013 Master of Science, University of California San Diego.

2018 Doctor of Philosophy, University of California San Diego.

REFEREED PUBLICATIONS

P. Franco Navarro, D. J. Benson, and V. F. Nesterenko, Nature of short, high-amplitude compressive stress pulses in a periodic dissipative laminate, Phys. Rev. E **92**, 062917 (2015).

P. Franco Navarro, D. J. Benson, and V. F. Nesterenko, Multiple scales of shock waves in dissipative laminate materials, Phys. Rev. E **94**, 033002 (2016).

P. Franco Navarro, D. J. Benson, and V. F. Nesterenko, Shear band patterning and post-critical behavior in AISI4340 steel with different microstructure, Int. Journal of Impact Engineering **112**, 144 (2018).

ABSTRACT OF THE DISSERTATION

Addressing complexity of materials behavior under extreme dynamic conditions using numerical modeling

by

Pedro Franco Navarro

Doctor of Philosophy in Engineering Sciences (Applied Mechanics)

University of California San Diego 2018

Professor Vitali F. Nesterenko, Chair
Professor David J. Benson, Co-Chair

Heterogeneous materials under dynamic loading exhibit dramatic transformations resulting in self-organization and in situ microstructural changes due to the complex interaction of nonlinearity, dispersion, different mechanisms of softening, and fracture. We use numerical simulations to explain the diverse mechanisms of deformation, localization and in situ patterning exhibited by these

materials and compare them to experimental results and phenomenological models.

In Chapters 2 and 3 we study dissipative Al-W laminates with unit cells 1, 2 and 4 mm under high velocity impact loading of different durations. Depending on the duration of the loading pulse, a qualitatively new solitarylike wave, a train of such waves or a quasistationary shockwave is formed in these dissipative laminates. A phenomenological model based on the Korteweg-de Vries equation is formulated introducing important space/time scaling for solitary and shock waves depending on materials properties.

In Chapter 4, Thick-Walled Cylinder experiments were conducted with highly heterogeneous porous mixtures of Al and W granular materials. Results were compared with numerical simulations to explore the effects of grain size and porosity on the mechanism of cavity instability. Numerical simulations demonstrated that a shear localization phenomena occurs along weak paths created by softer Al particles. The samples with initial porosity, delayed this mechanism of instability. Samples with grain sizes 400 and 100 micron demonstrated loss of cylindrical symmetry during collapse and sample with grain size 40 micron collapsed with mostly preserved cylindrical symmetry. This was consistent with experimental observation of cavity collapse in mixtures with 40 and 1 micron W particles.

In Chapter 5, explosively driven Thick-Walled Cylinder experiments were conducted with samples of 4340 steel having variable microstructures achieved

through heat treatment. It was observed experimentally that the change in the initial microstructure resulted in completely different dynamic behavior and self-organization of shear bands/cracks. The heat treated sample, catastrophically failed due the formation and interaction of shear bands developing into cracks. Numerical simulations are compared to the experimental results. It was shown that the inclusion of artificial defects is necessary to reproduce self-organized pattern of shear bands and cracks observed in experiments.

Chapter 1 : Introduction

The objective of this dissertation is to explore diverse complex phenomena, caused by dynamic loading in heterogeneous materials (metal composites, metallic alloys with natural defects and porous heterogeneous mixtures) focusing on numerical simulations, and phenomenological approaches which are compared with experiments when available. The main goal of this work is to help elucidate the diverse mechanisms that are present in dynamic loading events and are involved in high amplitude pulse formation, propagation as well as the main culprits that determine the stability of collapse.

The first part of this dissertation (Ch. 2 & 3) is focused on the study of the nature of short and long high amplitude pulses in a dissipative Al-W laminate material excited by high velocity impact.

The study of material response to high amplitude shock loading is normally based on the assumption that the shockwave inside the material has reached a steady state. This is assumed to happen once the shock travels inside the materials at least a few shock widths [1,2]. When this condition is fulfilled, the use of conservation laws across the shock front result in the Rankine-Hugoniot equations. These equations connect the states in front and behind the stationary shock, when the pulse is long enough [1-3].

A much-accepted relation in shock physics developed by Grady, assuming a steady shock propagating in homogeneous materials, connects the stress and strain rate in the shock front in the form $\sigma \, \alpha \, \dot{\epsilon}^4$ [4,5]. Through experimental

observations, it was discovered, that laminate materials are better described by a relation of the form $\sigma \alpha \dot{\epsilon}^2$ [6]. This relation still assumes the existence of a steady shock propagating in the laminate. Nevertheless, in the latter case, we are presented with a challenge to assume the steady state of the shock propagation. Numerous studies have shown that the establishment of the steady state of the shock might be complicated to achieve due to the combination of material properties and characteristics of the loading pulse. Examples of loading conditions that never reach a steady state in laminate materials can be found, for example in short duration pulses as is the case in: extremely powerful lasers [7,8], loading by impactors comparable to the size of the laminate cell or contact explosion created by thin layers of explosive [2,9,10]. In all these cases, the stationary shocks are not formed in the investigated materials. Another observed phenomena, which contradicts predictions based on acoustic approximations is that, close to impact or loading zone the traveling pulse exhibits an increase in amplitude before start decaying [11].

Although the loading conditions are an important part of the establishment of a steady shock, it is important to mention the influence of the properties of the laminate material. Materials under high amplitude loading can observe nonlinear behavior and due to the periodicity of laminate and dissimilar speeds of sound; strong dispersive effects can be observed [12]. The balance of these mechanisms can result in solitary waves in diverse systems [13,14].

In the work presented in Ch. 2, it is shown that in the case of Al-W laminate material that have been loaded by a short high-amplitude pulse accompanied by significant dissipation; the balance of the nonlinear behavior of components and the periodicity of the material creates a new qualitatively solitarylike wave. This pulse was investigated numerically and a phenomenological approach, based on the Korteweg de Vries equation, was developed. A nondimensional quantity named “time ratio” is used as an indicator when to expect a solitarylike pulse, a train of solitarylike pulses or in some cases a quasistationary shock.

In Ch. 3, the effects of long high amplitude stress pulses in the same Al-W laminate are explored. Through numerical calculations it was observed, that when the duration of the loading pulse is considerably longer than the characteristic cell size of the laminate (high time ratio), the establishment of a quasisteady shock is possible. The proposed phenomenological model from Ch. 2 is modified to include a viscous dissipation coefficient which allows for shock solutions. This shock solution can predict time and space characteristics of the quasisteady shock in the laminate. This could help with the design of layered composites with desirable tunable characteristics, e.g. pulse shaping to create shockless compression or amplitude mitigation of the shock.

Ch. 4 & 5 are centered around experimental and numerical results of Thick-Walled Cylinder (TWC) results with 4340 steel and Al-W granular composite.

The explosively driven TWC technique, developed by Nesterenko and his collaborators [15-20], was created to investigate the generation of spontaneous

instabilities and the formation, interaction, and patterning of shear bands in solid and granular materials, in reproducible strain controlled conditions in three dimensional environment. This is accomplished using a tunable explosive that allows for the soft collapse of the assembly driven by a thick walled tube which prevents geometric instability. This allows to investigate shear instability caused by material behavior. This helps to dictate the dynamics of the collapse without having to retune the experiment when multiple samples want to be studied.

Ch. 4 presents results of the investigation of the stability of cavity collapse in an Al-W granular material using the TWC technique. The main interest was to better understand what mechanisms are involved in the cavity collapse in granular materials, which could be relevant to the formation of hotspots in energetic materials or help elucidate mechanisms involved in cosmology [21,22]. Experiments revealed that for small grain sizes (less than 40 μm) the cavity collapse was stable despite the high level of heterogeneity in the Al-W granular mixture. Numerical simulations were used to investigate of the effects particle size and porosity on the stability of cavity collapse. Voronoi tessellations were used to represent the Al and W particles with grain sizes of 400, 100 and 40 μm. The smaller sizes of particles were impossible to investigate due to extremely long computational time. The results show that bigger grain sizes are responsible for bigger kinks at the interface of the sample and copper stopper tube. These kinks appear to be nucleation sites for instabilities that resemble shear bands observed in metals and uniform granular materials, e.g., SiC and Al_2O_3. The inclusion of

initial porosity in the numerical simulations prevented and/or retarded the formation of the shear instabilities observed in the samples that started as fully dense.

In Ch. 5, using the TWC technique, a study of shear band formation and patterning in steel 4340 with different microstructures is carried on. In the experiments, it was observed, that as-received steel was resilient to the phenomena of shear localization within the explored levels of global strain. When the 4340 specimens were heat treated, a completely different behavior was observed. Catastrophic failure, through the formation and interaction of shear bands occurred. Numerical simulations were used to better understand the formation, self-organization and pattern of shear bands in this steel.

It was found that material imperfections, modeled by the introduction of the right amount of “material defects” in numerical simulations, in combination with the right material constants in the frame of viscoplastic Johnson-Cook model, were sufficient to reproduce shear instabilities and post-critical behavior in this steel.

1.1 Chapter References

[1] R. Kinslow, *High-Velocity Impact Phenomena* (Elsevier, New York, 2012).

[2] V. F. Nesterenko, *Dynamics of Heterogeneous Materials* (Springer Science & Business Media, New York, 2001).

[3] R. McQueen, S. Marsh, and J. Fritz, Hugoniot equation of state of twelve rocks, J. Geophys. Res. **72**, 4999 (1967).

[4] D. E. Grady, Structured shock waves and the fourth-power law, J. Appl. Phys. **107**, 013506 (2010).

[5] D. E. Grady, Unifying role of dissipative action in the dynamic failure of solids, J. Appl. Phys. **117**, 165905 (2015).

[6] S. Zhuang, G. Ravichandran, and D. E. Grady, An experimental investigation of shock wave propagation in periodically layered composites, J. Mech. Phys. Solids **51**, 245 (2003).

[7] C. Wei, B. Maddox, A. Stover, T. Weihs, V. Nesterenko, and M. Meyers, Reaction in Ni-Al laminates by laser-shock compression and spalling, Acta Mater. **59**, 5276 (2011).

[8] C. Wei, V. Nesterenko, T. Weihs, B. Remington, H.-S. Park, and M. Meyers, Response of Ni/Al laminates to laser-driven compression, Acta Mater. **60**, 3929 (2012).

[9] V. Nesterenko, V. Fomin, and P. Cheskidov, Damping of strong shocks in laminar materials, J. Appl. Mech. Tech. Phys. **24**, 567 (1983).

[10] V. Nesterenko, V. Fomin, and P. Cheskidov, Attenuation of strong shock waves in laminar materials, *Nonlinear Deformation Waves* (Springer-Verlag, Berlin, 1983), p. 191.

[11] D. Benson and V. Nesterenko, Anomalous decay of shock impulses in laminated composites, J. Appl. Phys. **89**, 3622 (2001).

[12] N. K. Akhmadeev and R. K. Bolotnova, Propagation of stress waves in layered media under impact loading (acoustical approximation), J. Appl. Mech. Tech. Phys. **26**, 114 (1985).

[13] D. H. Yong and R. J. LeVeque, Solitary waves in layered nonlinear media, SIAM J Appl. Math. **63**, 1539 (2003).

[14] J. Engelbrecht, A. Berezovski, and A. Salupere, Nonlinear deformation waves in solids and dispersion, Wave Motion **44**, 493 (2007).

[15] Nesterenko VF, Lazaridi AN, Pershin SA. Localization of deformation in copper by explosive compression of hollow cylinders. Fiz. Goreniya Vzryva 1989;25(4):154–5.

[16] Nesterenko VF, Bondar' MP. Localization of deformation in collapse of a thick walled cylinder. Combust Explosion Shock Waves 1994;30(4):500–9.

[17] Nesterenko VF, Bondar' MP. Investigation of deformation localization by the “thick- walled cylinder” method. DYMAT J 1994;1(3):245–51.

[18] Xue Q, Nesterenko VF, Meyers MA. Evaluation of the collapsing thick-walled cylinder technique for shear band spacing. Int J Impact Eng 2003;28(3):257–80.

[19] Nesterenko VF, Meyers MA, Chen HC, LaSalvia JC. Controlled high-rate localized shear in porous reactive media

[20] Chiu PH, Olney KL, Higgins A, Serge M, Benson DJ, Nesterenko VF. The mechanism of instability and localized reaction in the explosively driven collapse of thick walled Ni-Al laminate cylinders. Appl Phys Lett 2013;102(24):241912.

[21] A. Kapahi and H. S. Udaykumar, Dynamics of void collapse in shocked energetic materials: Physics of void-void interactions, Shock Waves **23**, 537 (2013).

[22] P.A. Bland, G.S. Collins, T.M. Davison, N.M. Abreu, F.J. Ciesla, A.R. Muxworthy and J. Moore, Pressure–temperature evolution of primordial solar system solids during impact-induced compaction, Nature communications,**5**, 5451 (2014).

Chapter 2 : Nature of short, high-amplitude compressive stress pulses in a periodic dissipative laminate

2.1 Introduction

The response of materials to high-amplitude shock wave loading is usually analyzed based on the assumption that the shock wave has reached a steady state which is assumed to happen when the shock wave propagates a distance of a few shock front widths [1]. This assumption allows the use of the conservation laws across the shock front, resulting in the Rankine-Hugoniot equations connecting the states in front of and behind the stationary shock wave, if the duration of the pulse is long enough [1–3].

The case of laminated materials presents a challenge for such an approach, and the first studies to characterize the behavior of these materials in the acoustic realm, including their dispersive properties due to periodic mesostructure, can be found in [4–6]. For example, in [6] the authors propose a one-dimensional lattice model that includes geometrical dispersion. Their model agrees with the results of ultrasonic experiments. The behavior of an Al-W composite (W fibers placed in Al matrix) under impact by a thick Al plate, generating a semi-infinite loading pulse to avoid the formation of release waves on the back of the flyer plate, was investigated in [7]. The experimental results related to shock rise time show good

agreement with the numerical modeling based on the lattice model and nonlinear elastic-plastic response. The structuring of the wave front occurred near the impact surface. The formation of a steady shock wave profile in laminate materials can require much longer distances because the establishment of steady state behind shock can be delayed due to the longer mechanical and thermal relaxation processes. This is clearly illustrated in periodic systems composed from metal or glass plates with gaps between them where establishment of the steady state behind the shock wave happened after about ten reverberations of waves behind the leading part of the pulse [8,9]. In the case when laminate materials are loaded by a long duration incoming disturbance (especially for small size of the cell in laminate material) the stationary shock wave can be formed, and the final state can still be described in the frame of Hugoniot approach if conditions of thermal and mechanical equilibrium hold. In this case the Hugoniot curve is not sensitive to the mesostructural properties of material, e.g., cell size.

In some applications laminates are subjected to very short duration loading pulses, created, for example, by powerful lasers. But in the case of the short incoming pulse, caused by impact of a thin plate with thickness comparable to the thickness of a cell in the laminate or contact explosion of a thin layer of explosive [9], or by laser excitation [10,11], the stationary shock wave is not formed in the laminate. In this case the Hugoniot curve does not describe the states of dynamically compressed components and their response can be very sensitive to the pulse length and material mesostructure. For example, at short duration of

incoming pulse interesting phenomena such as anomalous dependence of leading shock amplitude on the cell size (increase of amplitude with decrease of cell size) were observed in experiments and in numerical calculations [9,12–14], being in contradiction with behavior expected from acoustic approximation [15]. Nonlinearity in the stress-strain relation was responsible for these deviations from linear elastic behavior.

In the case of relatively short duration of loading pulse a combination of dispersive properties and nonlinearity in layered media give rise to a qualitatively new, solitarylike pulses numerically investigated in [16–22].

The paper [16] considers the evolution of nonlinear elastic waves in a nondissipative layered media excited by the motion of the boundary and explores the effects of impedance mismatch between layers, which is a cause for a dispersion. They observed numerically that at the investigated boundary conditions the impedance mismatch coupled with the nonlinearities, introduced by nonlinear stress-strain dependence of components, resulted in a transformation of an incoming pulse into a train of localized pulses. The authors called them *stegotons* since it was not clear whether these localized pulses were formally solitons. They noticed that the width of each stegoton is about ten layers and it is independent of the size of the layers, but it depends on the wave amplitude. Their speed was equal to the effective sound speed for the linearized medium plus a term linearly depending on the amplitude. Their shape was roughly approximated by the sech2 function of time; both properties are characteristic for the Korteweg–

de Vries (KdV) solitons. Two stegotons with different amplitudes were excited at the boundary and the stegoton with the higher amplitude travels faster and eventually overtakes the first one with a smaller amplitude. As in the case of an interacting solitary wave the colliding stegotons roughly assumed their initial shape after separation with some phase shift.

In [16] the authors considered a comparison between a nonlinear laminate material with one of the layers having very small density and bulk elastic modulus (ratio of densities being equal to 10^{-3} and ratio of bulk moduli being equal to 2.5×10^{-4}) with the Toda lattice where particles of similar masses alternate with springs. They selected the unit cell in the Toda lattice being equal to the unit cell of the laminate (composed from the two different layers) and masses of particles being equal to the average density of the layered medium. The force in effective springs had exponential dependence on the strain mimicking force in the Toda lattice with the coefficient in exponent related to the smallest bulk modulus. This interaction force resulted in a correct effective sound speed in a linearized medium. In this special limited choice of parameters of laminate material, the authors found that solitarylike behavior of laminate can be modeled directly by the Toda lattice. The authors also introduce a set of homogenized equations which support the solitarylike solutions similar to the direct solutions of the original hyperbolic system.

The paper [17] emphasized that the microstructure of materials characterized by intrinsic space scales, e.g., lattice period, size of crystalline grain, thickness of layers in laminates, and distance between microcracks, is responsible

for the effects of dispersion and being combined with nonlinear behavior results in phenomena like solitons. The authors considered a discrete and continuum approach for the modeling of the effects of microstructure and nonlinearity following the Mindlin analysis [18]. Depending on the initial and boundary conditions they demonstrated formation of a single solitarylike pulse or a train of these pulses. They obtained good agreement with experimental data [19] of the stress history in the laminate polycarbonate (layer thickness 0.39 mm)–stainless steel (0.19 mm) at the distance 3.44 mm from the impacted face using a finite-volume algorithm and nonlinear parameter only for the polycarbonate. The simplified boundary conditions in calculations modeling plate impact in experiments, were given by a step function with the velocity amplitude equal to the velocity of the impacted plate (1043 m/s) with thickness 2.87 mm. However, the amplitude of the particle velocity in experiments on the interface with the laminate (having polycarbonate as the first layer) and polycarbonate impactor with velocity 1043 m/s should be equal to half of this value—521.5 m/s. Also it is not clear what duration was selected of the used step function (the authors probably used a rectangular function) as a boundary conditions modeling impact by a plate with finite thickness, which was able to provide a good fit to experimental data.

The propagation and head-on collisions of localized initial pulses were numerically investigated in [20] for microstructural materials with different values of microscale nonlinearity parameter. It was found that the interaction between localized waves is not completely elastic. The phase shift observed in such

interactions is increased when the amplitudes are dissimilar and with a longer observation time. Over short time intervals and small number of collisions the behavior of these localized pulses was close to the solitonic behavior in all considered cases.

The emergence of two solitary trains from the localized initial condition was numerically investigated using a Boussinesq-type equation [21] for nonlinear microstructured solids also following the Mindlin approach [18]. On the long time scale they observed establishment of the stationary amplitudes of each emerging localized pulse in the train with linear dependence of their speed on the amplitude. The speed and amplitudes of localized pulses were traced after their multiple collisions. They display the main characteristics of classical soli- tons though their interaction is not fully elastic, especially at the low amplitudes. Thus the authors suggested using the term “quasisolitons” to distinguish them from “pure solitons” characteristic for highly idealized nonlinear dispersive systems.

The propagation of nonlinear longitudinal strain waves in the case of uniaxial strain state in a layered material was studied using a macroscopic Boussinesq-type wave equation that has been derived in a long wave approximation through a high-order asymptotic homogenization method [22]. The derived coefficients in this equation are related to the linear and nonlinear elastic moduli, densities, and volume fractions of the components. The dispersion relation in the linearized Boussinesq-type wave equation was close to the exact dispersion relation obtained using the Floquet-Bloch approach for two laminate materials (a

low-contrast steel-aluminium laminate and a high-contrast laminate of steel and carbon-filled epoxy) at a ratio of cell size to characteristic wavelength less than 0.4; better agreement was obtained for high-contrast laminate. The authors also obtained the speed and width of the localized supersonic bell-shaped compression solitary wave as functions of nonlinear properties of materials and the amplitude of the solitary wave. In the case of physically linear elastic materials the geometric nonlinearity in combination with dispersion support only tension solitary waves.

The authors of [22] numerically investigated the nonstationary dynamic processes integrating macroscopic Boussinesq-type wave equation focusing on the evolution of nonlinear waves caused by different initial excitations. The initial conditions were taken as a rectangular profile with different nondimensional width δ. In case of a relatively narrow pulse of compression (δ = 5) the nonlinear excitation with given amplitude resulted in two solitary waves propagating symmetrically in opposite directions with a scattering backward radiation. It is important that at given parameters of laminates and amplitudes of excitation the formation of steady-shape solitary waves required a spatial interval three orders of magnitude larger than the cell size. A wider pulse of initial compression (δ = 20) with the same amplitude resulted in a train of four solitary waves with noticeable amplitudes. The properties of these solitary waves emerging from the initial conditions were similar to the stationary solitary wave solutions of the Boussinesq-type wave equation. The narrow pulse of tension (δ = 5) with the same amplitude

did not evolve into a steady-shape wave producing instead a delocalization of the initial excitation.

In this paper we investigate the nature of relatively short pulses in the laminate Al-W (with the cell size equal to 1, 2, and 4 mm) generated by impact of 8- and 2-mm impactors with velocity 2800 m/s, which created realistic initial and boundary conditions reproducible in physical experiments such as loading by short and powerful lasers [10,11], contact explosion [12,13], or impacts that could be expected from space debris. The dynamic response of materials at this level of stresses is characterized by significant viscoplastic dissipation which was not considered in the previous papers related to the propagation of solitarylike pulses (stegotons) in laminates [16–22]. The dissipation can suppress the formation of these solitarylike pulses because the disturbance must travel a relatively long distance from the point of excitation before this localized pulse is formed; e.g., in [22] the formation of steady-shape solitarylike waves in a nondissipative laminate required a spatial interval three orders of magnitude larger than cell size.

We investigated the characteristic length traveled by the pulses when single solitarylike pulses (or their trains) were formed under realistic, experimentally reproducible plate impact conditions (at various thicknesses of impactor) and their subsequent rate of attenuation in the presence of dissipation.

We also investigated the head-on collisions of solitarylike pulses impacting laminates from both sides. It was proven that after interaction the most prominent

change is a phase shift which agrees with the expected behavior of solitarylike waves.

We introduce a phenomenological model combining the dispersive properties of laminates, due to their periodic structure, and physical nonlinear properties of materials based on their shock adiabat (Hugoniot) instead of using third order elastic constants as in [22]. The Hugoniot curve is representing inherent nonlinear behavior of materials in a stationary shock wave at a very broad range of pressures. The combination of dispersive and nonlinear properties resulted in a KdV solitary wave. Based on this approach equations relating speed and widths of these solitarylike pulses to the geometrical and physical properties of materials in laminates were presented. The shape of the KdV solitary wave provided satisfactory fit to the shape of the localized pulses observed in numerical calculations. The speeds of KdV solitary waves also were close to the speed of localized pulses in the laminate at similar maximum pressures.

2.2 Simulations

We apply LS-DYNA's simulations to analyze propagation of high-amplitude dissipative nonlinear waves generated by plate impact in a one-dimensional (1D) laminate material. LS-DYNA is a general-purpose finite-element software [23]; its main strength is the capability to solve highly nonlinear transient dynamic problems by explicit integration. Figure 1 represents the geometry used in our numerical modeling, where L_c is the total length of the laminate composite, L_i is the length of

the impactor, and a and b are the respective thicknesses of the aluminum (Al) and tungsten (W) layers in the periodic composite material.

In this paper, all layers have the same thickness ($a = b$). For the purposes of this study we selected L_c = 280 mm for all cases. The duration of the incoming pulses was determined by the thickness of the impactor equal to 2 and 8 mm to produce stress waves with different durations and to investigate their properties.

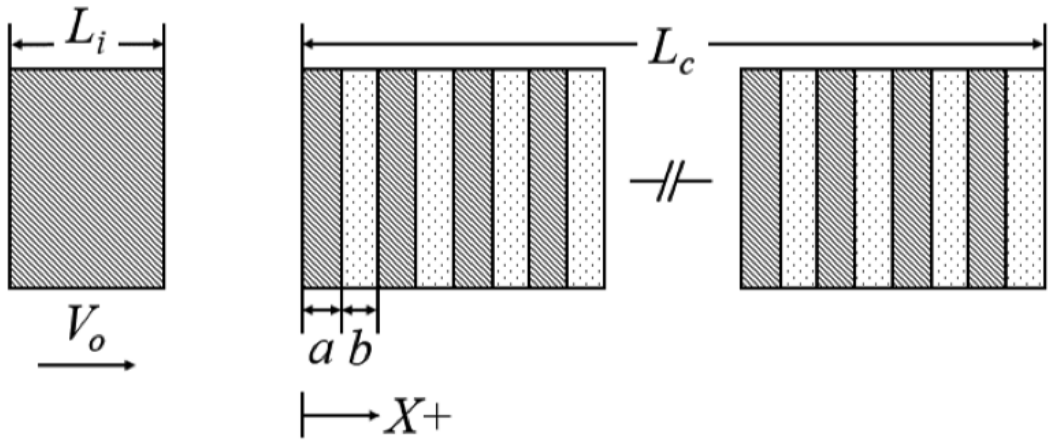

Figure 2-1: Geometry of the Laminate

The impactor in the current study was an aluminum plate having high initial velocity of 2800 m/s in the X+ direction. In all cases, the layers of the laminate are perfectly bonded and the end of the composite is free. It is expected that the bonding between layers does not affect the compression stress wave structure and the properties of the final state behind them because we are considering only compression waves similar to [12–14].

The material model used to characterize the behavior is the well-known Steinberg-Guinan model [24,25] coupled with the Grüneisen's equation of state; this rate independent model is described as follows:

$$G = G_0\left[1 + AP\eta^{-1/3} - B\left(\frac{E-E_c}{C_p} - 300\right)\right], \quad (1)$$

where G and G_0 are current and initial shear moduli, P is the pressure, $\eta = V_0/V$, V and V_0 are current and initial specific volumes, A is a coefficient in the pressure dependence of the shear modulus, B is the coefficient in the temperature dependence of the shear modulus, and E is the total internal energy per unit volume. The cold energy of the system per unit volume E_c is defined as

$$E_c = \int_{V_0}^{V} PdV - 300C_p \exp\left\{a\left(1 - \frac{1}{\eta}\right)\right\}\eta^{\gamma_0 - a}, \quad (2)$$

where the integral in the first term is along the 300 K adiabat [24].

The melting energy (in the code it is used to check if material reached the melting conditions during the dynamic deformation) is defined as

$$E_m = E_c + C_p T_m, \quad (3)$$

The dependence of melting temperature T_m on specific volume based on a modified Lindemann law is expressed as

$$T_m = T_{m0}\exp\left\{2a\left(1 - \frac{1}{\eta}\right)\right\}\eta^{2(\gamma_0 - a - 1/3)}, \quad (4)$$

where γ_0 is the original Grüneisen gamma, and a is the coefficient of the volume dependence of the Grüneisen's gamma.

The yield strength (Y) of the material including dependence on pressure and effects of strain hardening and thermal softening is given by

$$Y = \frac{Y_0}{G_0}\left[1 + \beta(\epsilon_i + \epsilon_p)\right]^n \left[1 + AP\eta^{-1/3} - B\left(\frac{E - E_c}{C_p} - 300\right)\right], \quad (5)$$

where

$$Y_0\left[1 + \beta(\epsilon_i + \epsilon_p)\right]^n \leq Y_{max}. \quad (6)$$

In Eq. (5) Y_0 is the initial yield strength and Y_{max} is the value of saturated yield strength, ϵ_i is the initial plastic strain, ϵ_p is the equivalent plastic strain added under dynamic loading, and β and n are work-hardening parameters.

Based on the Grüneisen's equation of state the pressure can be expressed as

$$P = \frac{\rho_0 C_0^2 \mu\left[1 + \left(1 - \frac{\gamma_0}{2}\right)\mu\right]}{1 - (S_1 - 1)\mu} + \gamma_0 E, \quad (7)$$

$$\mu = \frac{\rho}{\rho_0} - 1, \quad (8)$$

where ρ_0, ρ refer to the initial and density in deformed state.

The following materials parameters for Al and W used in calculations are presented in Table 1; they were taken from [25]. Another important variable to have in mind is the modification to Y_{max} in order to reduce material dissipation; the value used in that case was two orders of magnitude smaller than the real value.

Table 2-1: Material Properties

Parameters	Aluminum	Tungsten
G_0 (GPa)	27.6	160
Y_0 (GPa)	0.29	2.2
Y_{max} (GPa)	0.76	4
β	125	24
η	0.1	0.19
A (GPa^{-1})	652	9380
B (K^{-1})	$6.16 \cdot 10^{-4}$	$1.38 \cdot 10^{-4}$
T_{m0} (K)	1220	4520
C_p (J/kg·K)	287.67	43
γ_0	1.97	1.67
a	1.5	1.3
ρ_0 (kg/m^3)	2785	19300
C_0 (m/s)	5328	4030
S_1	1.338	1.237

The mesh size in all cases was equal 1×10^{-5} m = 0.01 mm and selected artificial viscosity resulted in a shock width in Al, W being at least ten times smaller than the smallest-layer thickness in the laminate (0.5 mm). This assures that a steady state is reached behind shock waves when they propagate inside each layer on the initial stage of pulse formation following the impact. Of course, it is

desirable that the shock width is similar to the one found in experiments [26–28], but the width of the shock front is not important for the parameters of the final state as long as the shock width is significantly smaller than the layer thickness. This ensures that the material reaches Hugoniot states at shock loading in each layer. The Hugoniot states are characteristic for stationary shocks and are independent of the specific mechanisms of dissipation defining resulting shock width. The plastic shock width (Δx) and the rise time (Δt) at a shock stress of 70 GPa were equal to Δt = 3.72×10^{-9} and Δx = 3.38×10−^{5}m for aluminum and Δt = 9.69 × 10^{-9} and Δx = 4.79 × 10^{-5} m for tungsten. Both of the shock widths are about ten times smaller than the smallest-layer thickness in the laminate (0.5 mm), which assures that Hugoniot states behind the shock are reached inside each of the layers on the initial stage of pulse formation.

We validated results of LS-DYNA calculations with selected material properties based on comparison of the final thermodynamic states behind shock waves with available Hugoniot data. The comparison demonstrated that the model used correctly predicts the stress and specific volume in the simulation of single shock in individual materials. Even more important is that the simulations correctly predict the temperatures on the Hugoniots and also the temperatures after unloading for Al and W. This numerical approach was used to investigate the nature of relatively short, high-amplitude stress pulses in the Al-W laminate.

2.3 Results of Numerical Simulations

The nature of the short stress pulses of different durations excited by the impact of an Al plate with thicknesses of 2 and 8 mm propagating in the laminate materials with different cell sizes at various distances from the impact side is presented below. The main focus is on the nature of the pulses generated at various conditions of loading and to discover the nature of propagating pulses and scaling that might be generated by the interplay between duration of impact controlled by the thickness of impactor and cell in the laminate materials. The main characteristic time scaling is determined by the ratio (t_r) of the duration of the incoming pulse and the duration of propagation time through the cell approximated by

$$t_r = \frac{2d_{imp}}{C_{imp}} \Big/ \frac{d_{lam}}{C_{lam}}, \tag{9}$$

where d_{imp} and d_{lam} are the size of the impactor and size of the cell in the laminate respectively; c_{imp} and c_{lam} refer to the sound speed of the impactor and the laminate. For the sound speed in the laminate, we use the definition for the average sound speed in a laminate found in [16,29]. This definition is later used in the theoretical approach developed in this paper. The final expression for the time ratio is

$$t_r = \frac{2d_{imp}}{C_{imp}} \sqrt{\frac{d_{Al}^2}{C_{Al}^2} + \frac{d_W^2}{C_W^2} + \left(\frac{Z_{Al}}{Z_W} + \frac{Z_W}{Z_{Al}}\right)\left(\frac{d_{Al}d_W}{C_{Al}C_W}\right)}, \tag{10}$$

where d_{Al} and d_W refer to the Al and W layer sizes of the laminate, Z_{Al} and Z_W ($Z_i = \rho_i C_i$) represent the acoustic impedance of each layer, and finally C_Al and

C_W are the corresponding sound speeds of each layer. For all our studied cases C_{imp} = C_{Al} but d_{imp} has values of either 2 or 8 mm. From here on, the laminated materials are referred to as 2 + 2, 1 + 1, and 0.5 + 0.5 laminates, corresponding to 4−, 2−, and 1-mm cells. All the laminates were loaded by impact of the Al plate at velocity 2800 m/s and FWHM refers to full width at half maximum.

2.3.1 2 + 2 Al-W laminate, impact by 8-mm Al plate

The impact loading of the 2 + 2 laminate by Al impactor with the thickness 8 mm corresponds to the value of tr equal to 2.5. In these calculations real materials properties presented in the Table I were used. Figures 2(a)–2(d) show that these conditions of impact did not result in a steady state shock wave in the laminate because the duration of the incoming pulse was too short.

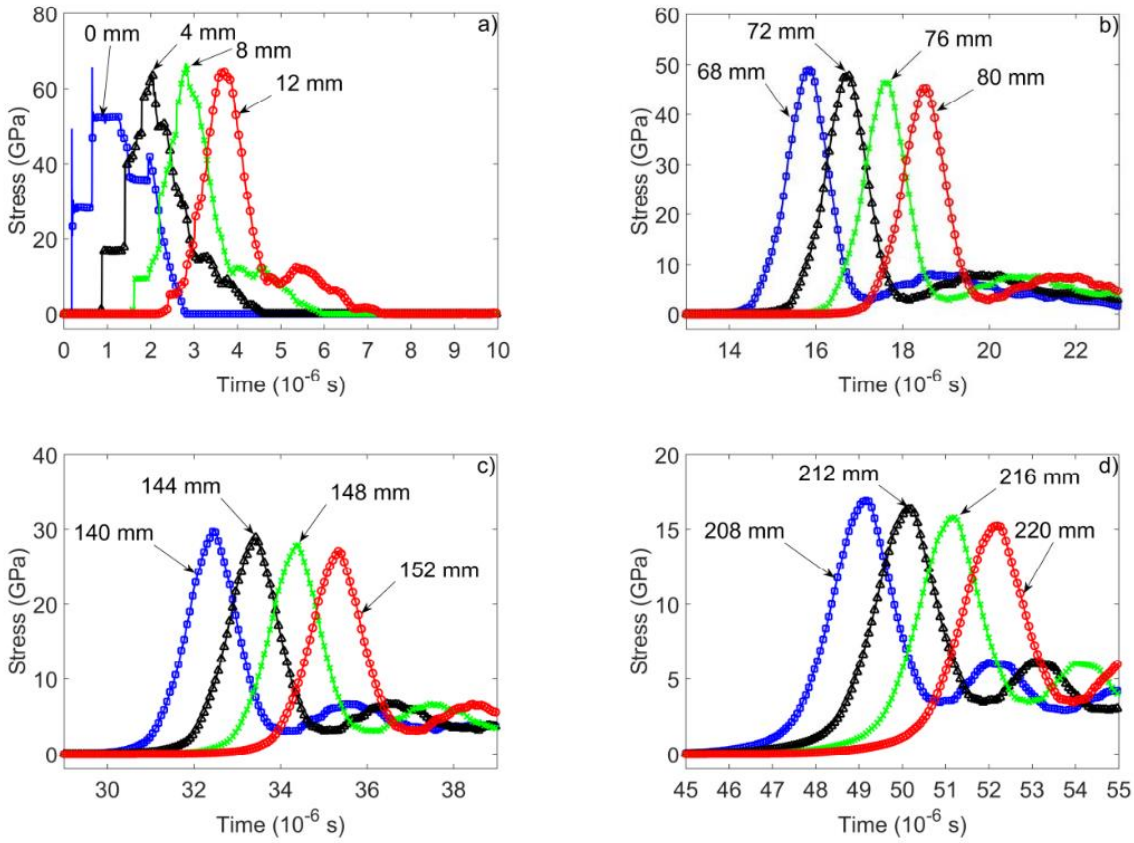

Figure 2-2: Stress pulse evolution in 2 + 2 laminate; data correspond to the interfaces of Al-W layers at different depths: (a) 0, 4, 8, and 12 mm; (b) 68, 72, 76, and 80 mm; (c) 140, 144, 148, and 152 mm; (d) 208, 212, 216, and 220 mm. The pulse was generated by the impact of an 8-mm Al plate at velocity of 2800 m/s.

Shock waves in each of the layers are clearly distinguishable at depths up to 8 mm from the impacted end. We observe the formation of a qualitatively unique pulse (not a shock wave) mainly formed at the distance 12 mm from the impacted end [Fig. 2(a)]. It has a width close to only three cell sizes with a small amplitude tail. It is clear from Figs. 2(a)–2(d) that formation of the main pulse is caused by multiple reflection of leading stress pulses on Al-W interfaces mostly balanced by nonlinearities of the Al and W behavior. The tail is due to the dissipative properties

of the materials. The dispersion originates from multiple shock wave re- flections from interfaces clearly seen in Fig. 2(a). The main pulse propagates with decreasing amplitude being equal to 65 GPa at a depth of 12 mm and about 15GPa at a depth of 220 mm. This decrease of amplitude is accompanied by an increase of the main pulse space width (FWHM increased about 40%). At larger depths the main pulse is accompanied by an oscillatory tail and at the relatively short distances, e.g., from 68 to 80 mm, the whole pulse can be considered as quasistationary with a similar profile but decreasing amplitude [Fig. 2(b)]. It is very important to remark that the observed main localized pulse with characteristic length comparable to the cell size of the laminate was formed in dissipative media. The rate of dissipation in our calculations matches real losses of energy, unlike in previous papers where no dissipation was taken into account [16–18,20–22]. It is essential to point out that this “real” dissipation does not prevent formation of a prime localized wave in our conditions of loading, and it only results in its attenuation. We can see that the mesostructure and nonlinear properties of a laminate resulted in dramatic transformation of the initial shock wave into a localized pulse with a different path of loading in comparison with the shock wave. As a result, temperatures corresponding to the maximum stresses are significantly different than at the same stresses in the shock wave. For example, a shock wave at a stress of 55 GPA in Al results in a temperature equal to 1471 K versus a temperature of 650 K in the localized pulse. We conducted simulations at relatively small amplitude of stress pulses generated by impact of 280 m/s flyer Al plate in

Al-W laminate with “normal” dissipation. The propagating stress pulse generated by this impact exhibits a tendency to localize, but attenuates very rapidly developing an attached oscillating tail instead of a quasistationary pulse observed at higher amplitudes of the stresses [Fig. 2(b)].

The formation of the localized pulse with a smooth front is beneficial for shock protection because it prevents spall on the free surface.

2.3.2 2 + 2 Al-W laminate with artificially small Y_{max}, impact by 8-mm Al plate

We now investigate the laminate with the same mesostructure but with reduced maximum yield strength Y_{max} of the materials thus causing plastic flow to occur at lower stress levels reducing dissipation. This case helps us to clarify the role of plastic deformation on the formation of the pulse. It is possible to observe that close to the impacted side the same dispersion and nonlinearity shapes the leading wave as in the previous case [compare Fig. 2(a) with Fig. 3(a)].

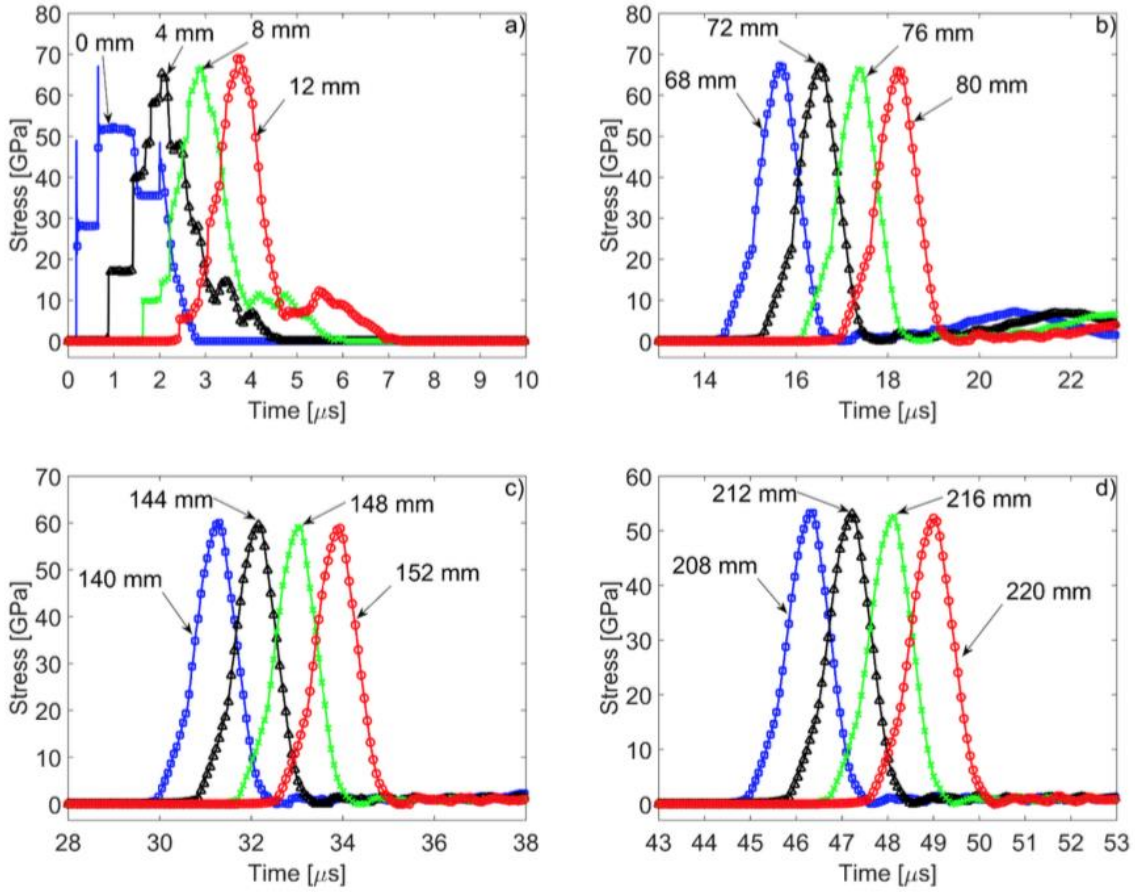

Figure 2-3: Stress pulse evolution in 2+2 laminate with artificially small Y_{max}; data correspond to the interfaces of Al-W layers at different depths: (a) 0, 4, 8, and 12 mm; (b) 68, 72, 76, and 80 mm; (c) 140, 144, 148, and 152 mm; (d) 208, 212, 216, and 220 mm.Pulse was generated by the impact of an 8-mm Al plate at velocity of 2800 m/s.

Figure 3(a) shows the initial steps in development of the solitarylike pulse through multiple shock reflections. Figure 3(b) demonstrates the persistence of the kinks on the fronts of practically formed solitarylike pulses and their slow separation from their tails, and Fig. 3(c) presents solitarylike pulses separated from their tails with relatively slow disappearance of kinks on the fronts of stress profiles at appropriate distances from the entrance. Finally, Fig. 3(d) shows the stationary

solitarylike pulses completely separated from their tails and without kinks on the front parts. In the case of material with real properties we formed a quasistationary attenuating oscillatory wave profile [Figs. 2(a)–2(d)], unlike solitarylike waves at low dissipation (Fig. 3).

It is interesting to compare pulses in material with real dissipative properties, near the impacted end; pulses with similar amplitude in artificially-low-dissipative materials; and pulses of similar amplitude where the laminate behaves elastically (Fig. 4). Figure 5 demonstrates that these pulses at similar maximum amplitudes (taken at different distances from the impacted side, 40 mm for real properties, 156 mm for artificially low dissipation, and 80 mm for the elastic case) are almost identical. In the case of the material with artificially low maximum yield strength there is a slight difference in the pulse shape—the front of the wave has a clear kink that does not disappear until the pulse has traveled about 200 mm [Fig. 3(d)]. To understand how these pulses propagate in a pure elastic laminate, we ran calculations with real dissipative properties up to the propagation distance where the quasistationary pulse was formed after traveling the distance of 64 mm and after that it transmitted into the pure elastic material with identical mesostructure. The pulse in pure elastic materials propagated initially with relatively small changes (amplitude increase from initial value of 55–59 GPa), quickly approaching the steady state after a distance of about 11 cells (Fig. 4).

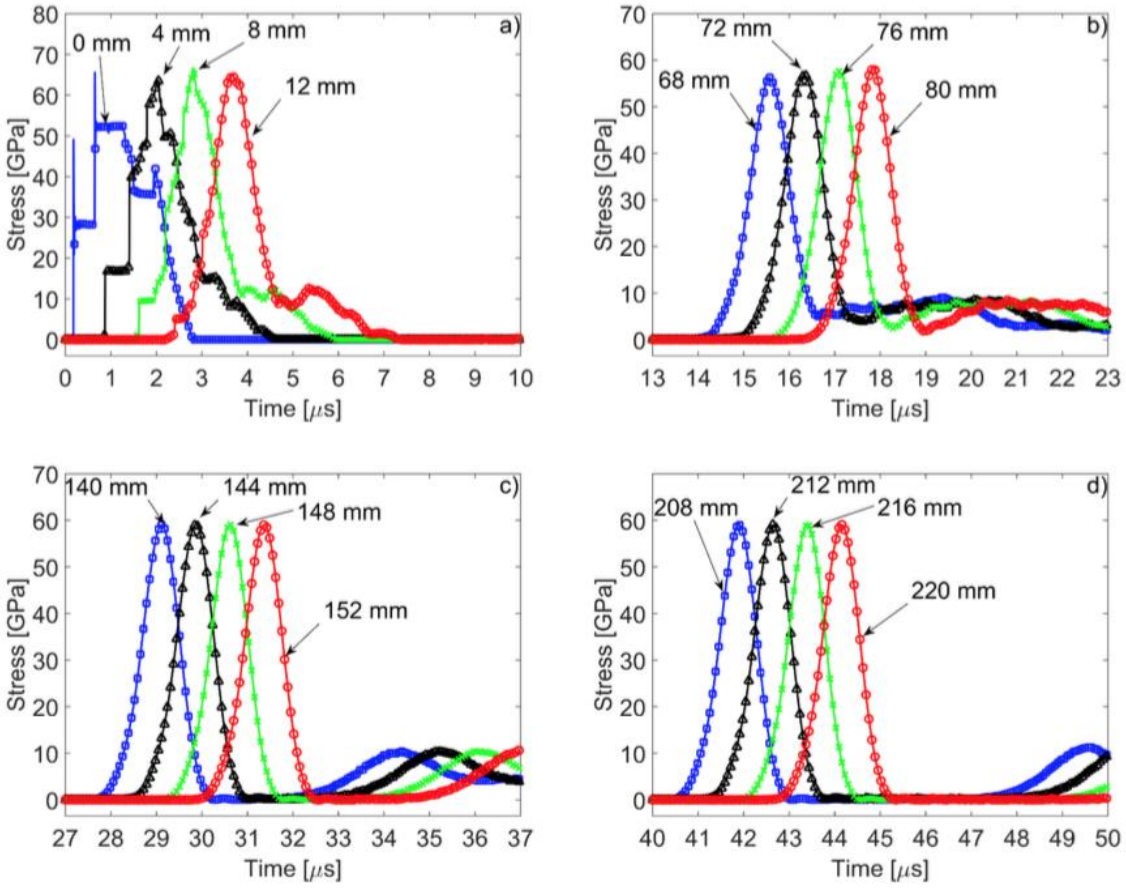

Figure 2-4: Stress pulse evolution in 2 + 2 laminate; data correspond to the interfaces of Al-W layers at different depths: (a) 0, 4, 8, and 12 mm; (b) 68, 72, 76, and 80 mm; (c) 140, 144, 148, and 152 mm; (d) 208, 212, 216, and 220 mm.The pulse was generated by the impact of an 8-mm Al plate at a velocity of 2800 m/s.Initial length of the laminate with real dissipative properties was 64 mm; it was in contact with a pure elastic laminate with identical mesostructure.

Thus it is possible to conclude that the leading pulse in a dissipative material even at relatively large distances from the impacted end (Figs. 2–4) is dominated by the combination of dispersion and nonlinearity, and cell size dictates the spatial dimension of this stress pulse (FWHM of the pulse is equal to 1.17 cell sizes).

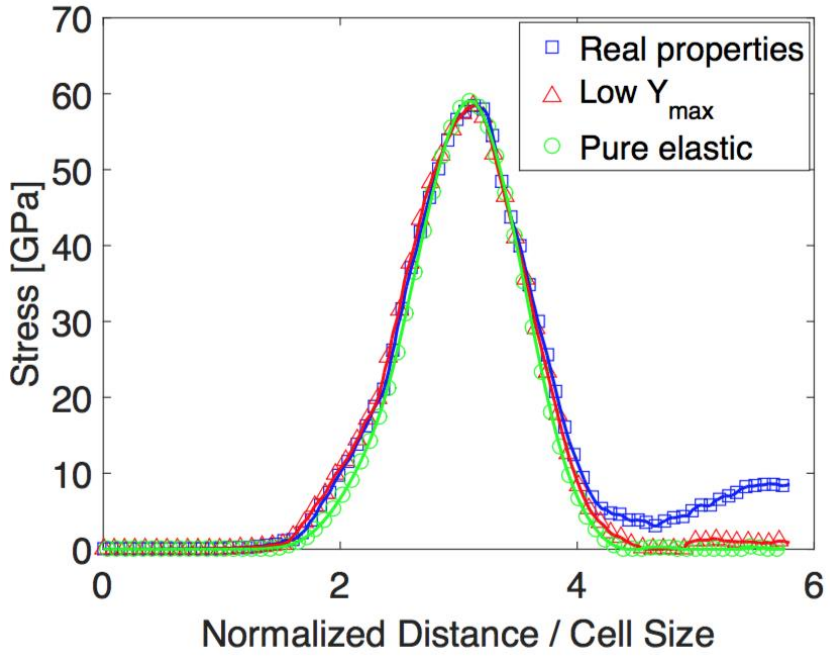

Figure 2-5: Comparison of wave shape at same stress amplitude of 58 GPa generated by the impact of an Al plate with thickness 8 mm for the case of a 2 + 2 laminate with real dissipative properties, laminate with an artificially small Y_{max}, and laminate with elastic behavior.

Despite the similarity of stress pulses (Fig. 5) we may observe different temperatures due to the difference in dissipative properties. The time dependence of the stresses and temperatures in the localized pulse propagating in the 2 + 2 laminates with different dissipative properties is presented in Fig. 6. It is clear that the amplitude decrease in both cases (less in the material with an artificially small Y_{max}) did not significantly change the pulse duration time and in the case of the material with smaller dissipative properties the shape of the pulse was maintained practically the same, with the FWHM change being only about 3%. This agrees with the previous conclusion that the pulse shape is determined mostly by nonlinearity and dispersion with dissipation affecting mostly amplitude.

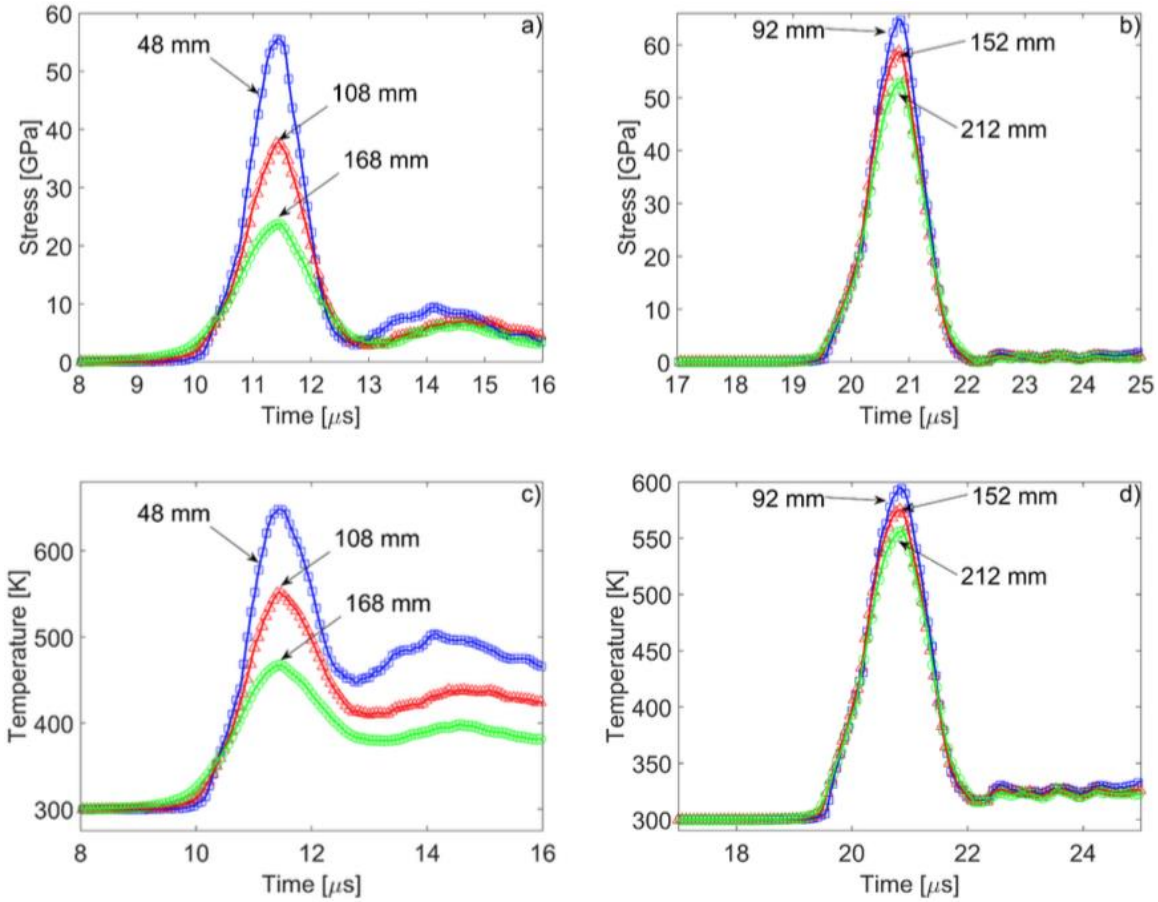

Figure 2-6: Comparison of attenuating stress traveling waves generated by the impact of an Al plate with 8 mm thickness in a 2 + 2 laminate and their corresponding temperatures in Al layer: (a, c) Laminate with real material properties and (b, d) laminate with an artificially small Y_{max}.

Though nonlinearity and periodic mesostructure in real materials are able to support the localized pulse with the shape similar to the less dissipative case, the important feature in the former laminate is the significant residual temperature, about half of the maximum temperature [Fig. 6(c)]. This behavior emphasizes the difference of this localized wave with classical solitary wave in which material returns to its initial state after being dynamically compressed.

It is very important to emphasize that the maximum temperatures at these waves are significantly smaller than temperatures in the shock waves at the same amplitude. In the material with real dissipative properties at maximum stress of 55 GPa in a quasistationary localized wave, increase of the Al temperature was 350 K [Fig. 6(c)], which is more than three times smaller than the increase of temperature in the shock wave in Al at the same pressure (1171 K); the initial temperature was 300 K.

The difference in temperature increase after unloading is also dramatic—after unloading of the quasistationary localized pulse with amplitude of 55 GPa, the increase of residual temperature over initial temperature was about 150 K, versus an increase of residual temperature being 493 K after shock loading with the same stress amplitude and subsequent unloading.

If we consider a whole pulse with leading amplitude of 55 GPa (including the tail) as a quasistationary shock wave then the estimate of the temperature increase at the tail with stress of 4 GPa [Fig. 6(a)] will be equal 30 K (corresponding to shock stress of 4 GPa), which is much smaller than 170 K in the tail of the localized wave [Fig. 6(c)]. Thus a complex quasistationary pulse with two maxima cannot be considered as a stationary shock wave.

These comparisons demonstrate that under considered impact loading the temperature estimations based on the Hugoniot of components using dynamic pressures are not adequate. Because the localized pulses provide shockless compression of Al and W it is interesting to compare the maximum calculated

temperatures with the temperature corresponding to isentropic compression. For Al at 55 GPa the estimate of the isentropic temperature increase is equal to 227 K [30], which is smaller than the calculated temperature increase of 350 K in a localized wave [Fig. 6(c)]. The estimated temperature in isentropic compression is much closer to the calculated temperature in localized wave than temperature at shock loading at the same pressures. Thus temperatures under isentropic compression give the reasonable lower estimate of the maximum temperatures in localized waves.

2.3.3 1 + 1 Al-W laminate, impact by 8-mm Al plate

It is interesting to determine if the shape and amplitude of the localized pulse observed in previous calculations is scaled with the size of the cell in laminates or is simply determined by the incoming pulse. To clarify this point we calculated the wave evolution inside a 1 + 1 mm laminate with real dissipative properties generated by the same impact as in the case of a 2 + 2 laminate. The thickness of the impactor was the same, but the time ratio of the impactor to the cell was larger than in the previous case. This also allows us to investigate if the number of localized pulses depends on the time ratio. For example, in the case of strongly nonlinear waves in granular materials [9] a single solitary wave was excited when the mass of the impactor was equal to the mass of the particle and multiple solitary waves were generated at the larger mass of the impactor.

However, the nature of the propagating pulse can be strongly influenced by the dissipative properties of the dispersive media [9,31,32].

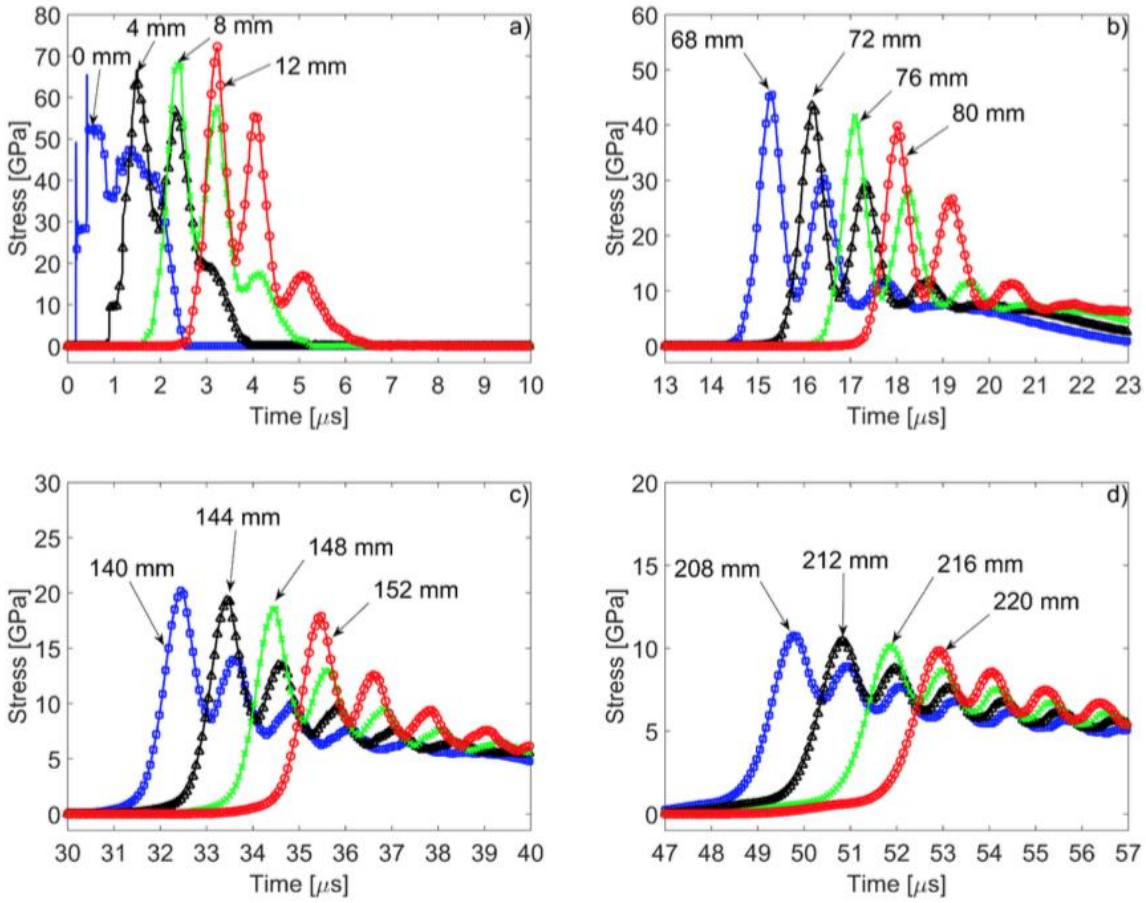

Figure 2-7: Stress pulse evolution in 1 + 1 laminate; data correspond to the interfaces of Al-W layers at different depths: (a) 0, 4, 8, and 12 mm; (b) 68, 72, 76, and 80 mm; (c) 140, 144, 148, and 152 mm; (d) 208, 212, 216, and 220 mm. The pulse was generated by the impact of an 8-mm Al plate at a velocity of 2800 m/s.

The impact of an 8-mm Al plate on this 1 + 1 laminate corresponds to the time ratio of the impactor to cell size being equal to 5.1, which is about two times larger than in the previous case of the 2 + 2 laminate. Also it is interesting to see if the decrease of the cell size at the same impactor mass results in faster formation

of localized pulses and if the corresponding distance for the formation of such pulses is scaled with the cell size.

The evolution of the wave at different depths is presented in Fig. 7. The impact with this impactor to cell time ratio of 5.1 demonstrated a tendency to the formation of multiple pulses close to the impacted end. Nevertheless, the dissipative properties of the material prevent the formation of the train of solitarylike waves. Instead an oscillatory triangular profile was observed at larger depths [Figs. 7(c) and 7(d)].

There is a difference between maximum amplitudes of stress in these pulses at similar depths of 220 mm. For example, the amplitude of the leading pulse is equal to 15.2 GPa for the 2 + 2 laminate versus 9.8 GPa for the 1 + 1 laminate, despite the same impact and the same average density of laminates. This difference is apparently due to the difference in their dispersive properties resulting in generation of multiple solitarylike waves in the laminate with smaller cell sizes. This demonstrates that amplitudes of the stress pulses can be decreased by decreasing cell size in laminates, which results in multiple solitarylike waves with small amplitude instead of a single one with a larger amplitude.

At the depths where the quasistationary pulse is observed (68–80 mm), the ratio of its characteristic scales to cell size (FWHM/d = 1.25 and (0.1 − 0.9) Δ/d = 1.15) are similar to those observed for the 2 + 2 laminate, demonstrating their scaling with the laminate cell size.

2.3.4 1 + 1 Al-W laminate with artificially small Y_{max}, impact by 8-mm Al plate

We saw in the previous section that dissipative properties may be responsible for the triangular oscillating wave profile preventing formation of a train of separate solitary waves. To clarify the role of dissipation we investigated the nature of the wave generated at the same impactor to cell time ratio (5.1), but introducing artificially small yield strength and the reduction of the dissipation. It is clear that reduced dissipative characteristics of the components facilitated the separation of the train of localized pulses (Fig. 8). They travel with different speeds depending on their amplitude and resemble a train of weakly attenuating solitarylike waves. This behavior is contrary to the previous case where a quasistationary strongly attenuating triangular oscillatory profile was formed at identical conditions of impact (Fig. 7).

We consider the formation of a quasistationary solitarylike wave when the stress in the wave reached 10% of its maximum on the release part. Following this agreement, we observed that its formation occurs fairly fast (at about 26 mm in depth) after traveling 13 cells. The apparently longer distance for establishing a stationary solitarylike pulse in this case, in comparison with impact on a 2 + 2 laminate, with the same thickness of impactor is due to the presence of the second wave following the first one.

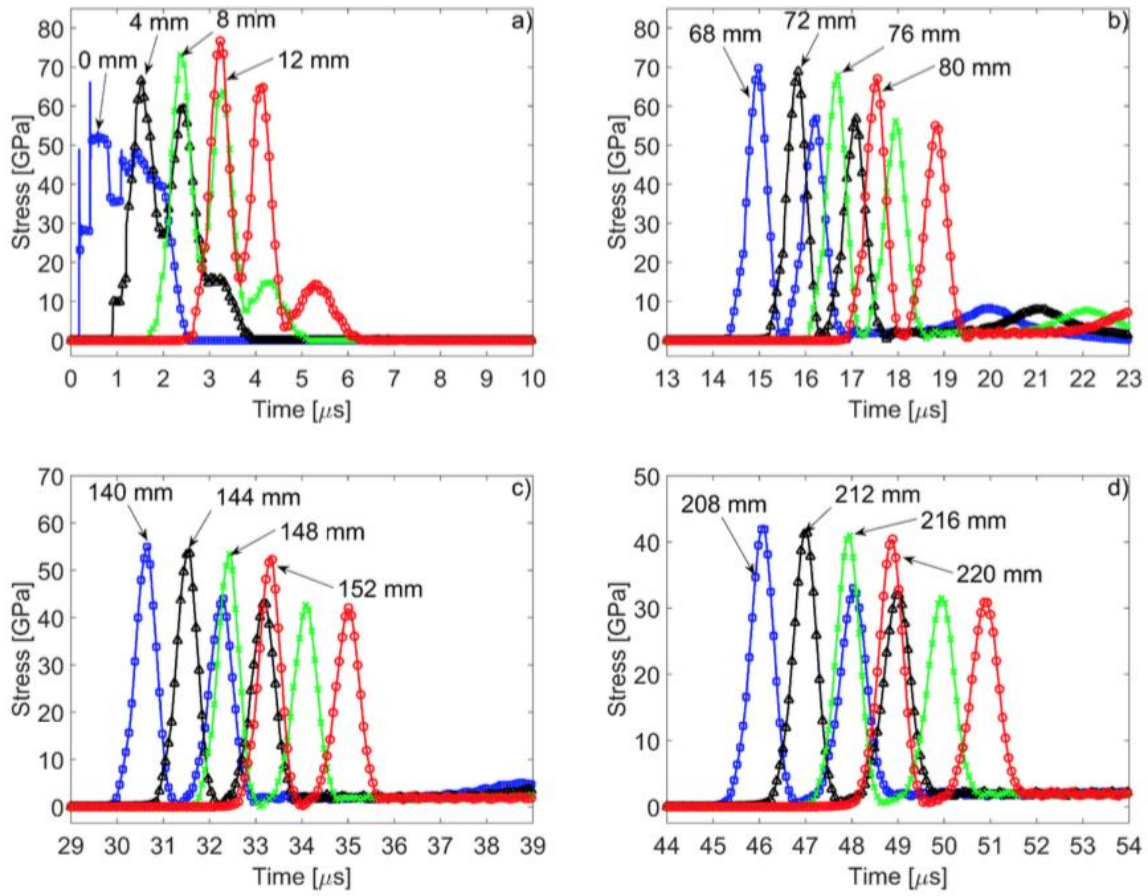

Figure 2-8: Stress pulse evolution in 1+1 laminate with artificially small Y_{max}; data correspond to the interfaces of Al-W layers at different depths: (a) 0, 4, 8, and 12 mm; (b) 68, 72, 76, and 80 mm; (c) 140, 144, 148, and 152 mm; (d) 208, 212, 216, and 220 mm. The pulse was generated by the impact of an 8-mm Al plate at a velocity of 2800 m/s.

The FWHM width of the localized pulse was equal to 1– 1.25 times the cell size depending on amplitude, which is similar to the width of the localized pulse in 2 + 2 laminate in nondissipative and dissipative cases (Fig. 8).

2.3.5 0.5 + 0.5 Al-W laminate, impact by 8-mm Al plate

It is interesting to investigate the characteristic scale of localized pulses in relation to cell size and their number and distance at which they are formed in the

laminate with reduced cell size under the same impact (duration of incoming pulse). The impactor to cell time ratio was increased to 10.2 by reducing the cell size to 1 mm (0.5 + 0.5 mm layered material) and keeping the duration of the incoming pulse the same (thickness of Al impactor, 8 mm). The results should be compared with the cases where 2 + 2 and 1 + 1 laminates were impacted by the 8-mm-thick Al plate at the same velocity (Figs. 2 and 7).

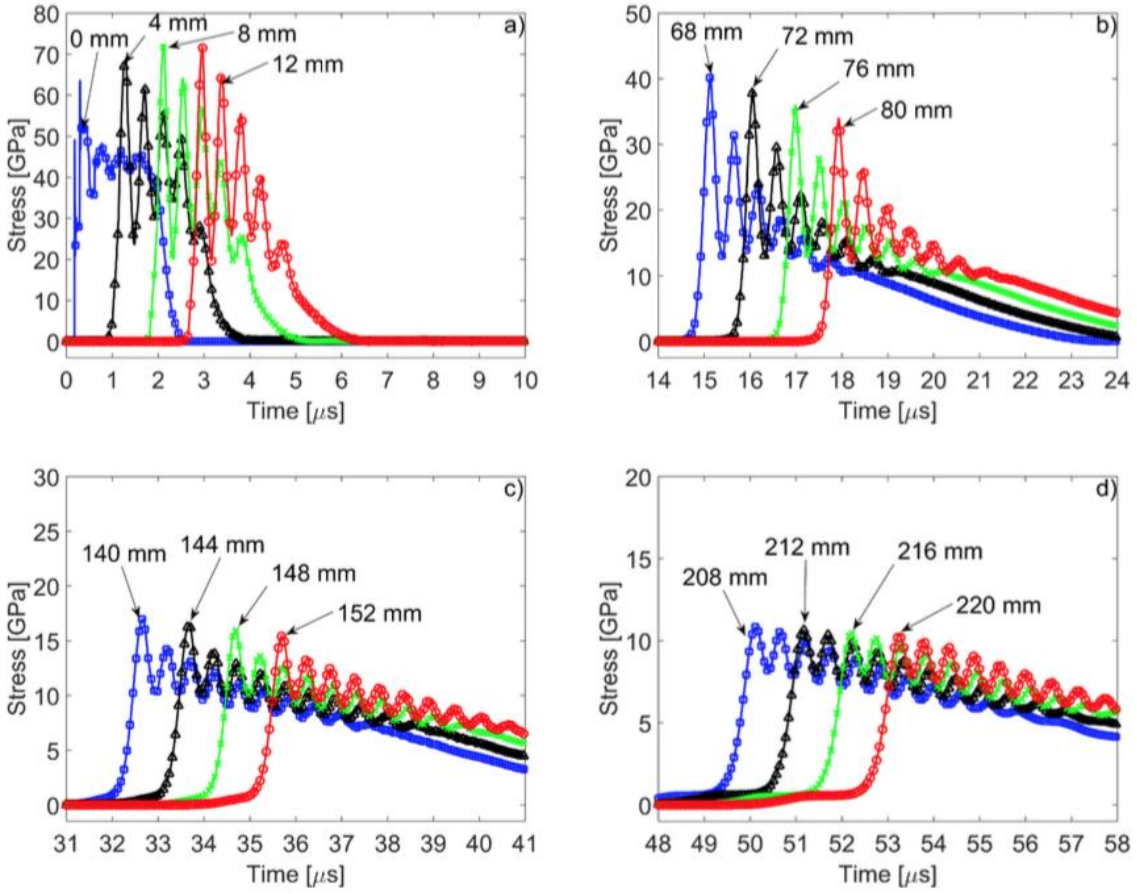

Figure 2-9: Stress pulse evolution in 0.5 + 0.5 laminate; data correspond to the interfaces of Al-W layers at different depths: (a) 0, 4, 8, and 12 mm; (b) 68, 72, 76, and 80 mm; (c) 140, 144, 148, and 152 mm; (d) 208, 212, 216, and 220 mm. The pulse was generated by the impact of an 8-mm Al plate at a velocity of 2800 m/s.

In the case of the 0.5 + 0.5 laminate, an oscillating triangular pulse was formed indicating the tendency to create the train of five localized waves Fig. 9(a), instead of one pulse (in the 2+2 laminate, t_r = 2.5) and three pulses (in the1+1 laminate, t_r = 5.1) in the previous cases, also with real dissipative properties of the components (Figs. 2 and 7). It should be mentioned that at a time ratio equal to 2.5 a single quasistationary pulse was formed (Fig. 2) and at a time ratio of 5.1 an oscillatory attenuating triangular pulse was observed (Fig. 7). These results prove that there is a strong correlation between shapes of wave profiles generated by the same impact at different time ratios. The time ratio determines the ratio of the characteristic time of the incoming load and the time scale determined by mesostructure, e.g., the time of wave propagation through the cell or the time duration of corresponding quasistationary pulses.

In weakly nonlinear and strongly nonlinear discrete materials there is a value of critical viscosity corresponding to the transition from oscillatory stationary shock profile to monotonous shock [33]. It seems that in the case of laminates there is a value of yield strength Y_{max} that will prevent splitting of the initial pulse into a train of solitary waves resulting in oscillatory or monotonous shocklike pulse.

Because different wave profiles were formed in laminates with different cell sizes at the same impact, it is interesting to compare the effectiveness of each laminate to decrease the amplitude of the leading pulse (it should be mentioned that decrease of cell size may result in the opposing effect and cause an increase of the amplitude of the leading pulse [14] [see also Figs. 2(a), 7(a), and 9(a)]. The

amplitudes of the leading pulses in laminates with different cell sizes, at the same depth of 220 mm, were equal to 15.2 GPa (2 + 2 laminate), 9.8 GPa (1 + 1 laminate), and 10.3 GPa (0.5 + 0.5 laminate). Although there is a small difference between the amplitudes for the 1 + 1 mm and 0.5 + 0.5 (with slight increase of amplitude in the latter case), the amplitude in the 2 + 2 layered composite is about 50% larger. This difference in the amplitudes of the leading wave can be explained due to the changes on dispersive properties of the laminate without changing the dissipative and nonlinear properties of the components. These data also demonstrate that amplitude of the leading pulse cannot be reduced indefinitely with reduction of the cell size.

Some very interesting phenomena of the increase of the duration of the triangular pulse in the 0.5 + 0.5 laminate should be mentioned (compare Figs. 7 and 9). We will see later that this is directly connected to the dispersive properties of the laminates.

The characteristic (0.1–0.9) space scale of the main leading front of the oscillating triangular wave at large depths is scaled with the cell size being equal to about 1.1 cell sizes [Fig. 9(b)]. This scaling is similar to the size of the leading front in the 1 + 1 laminate [Fig. 7(b), 1.1 cell size]. It is interesting that in this laminate we observe the dispersive elastic precursor whose length is increasing with propagation distance [Fig. 12(d)].

2.3.6 2 + 2 Al-W laminate, Al impactor with thickness of 2 mm

In the case of a 2 + 2 laminate with real material properties, under the impact of an 8-mm Al flyer plate, we observed that a slightly attenuating solitarylike pulse was generated from a relatively long incoming pulse (Fig. 2). It is interesting to see if a similar solitarylike wave could be generated in the same 2 + 2 laminate from different initial conditions (reduced duration of impact by using a 2-mm instead of 8-mm Al flyer plate; in this case the time ratio between the impactor and the cell is 0.6). We could expect that shorter duration impact may create a similar solitarylike pulse if the laminate under high- amplitude loading behaves as a classical weakly dissipative nonlinear dispersive medium.

Figures 10(a)–10(d) show the evolution of the stress profile as a result of the impact of the Al plate with a thickness of 2 mm on the 2 + 2 laminate. It is clear that the localized pulse is also formed at the distance of about 24 mm from impacted end (not shown in the figures). This process required a considerably longer distance than 12 mm in the 2 + 2 laminate impacted by an 8-mm Al plate (compare Fig. 10 with Fig. 2).

Contrary to what we observed in the case with an 8-mm impactor, the amplitude of the formed solitarylike pulse was smaller (compare Figs. 2 and 10). This could be due to the smaller linear momentum and energy in the case of a 2-mm Al striker, but as soon as a solitarylike pulse was formed (with FWHM equal to about two cells and 0.1–0.9 ramp size being close to two cells also) it was practically identical to the leading part of the same amplitude (10 GPa) pulse in the

same laminate formed under impact by 8 mm (Fig. 11). It is important to remark that once the amplitude has been greatly reduced (below 5 GPa at the depths larger than 140 mm) an elastic precursor can be observed and the shape of the pulse does not resemble a classic shape of a soliton [Figs. 10(c) and 10(d)].

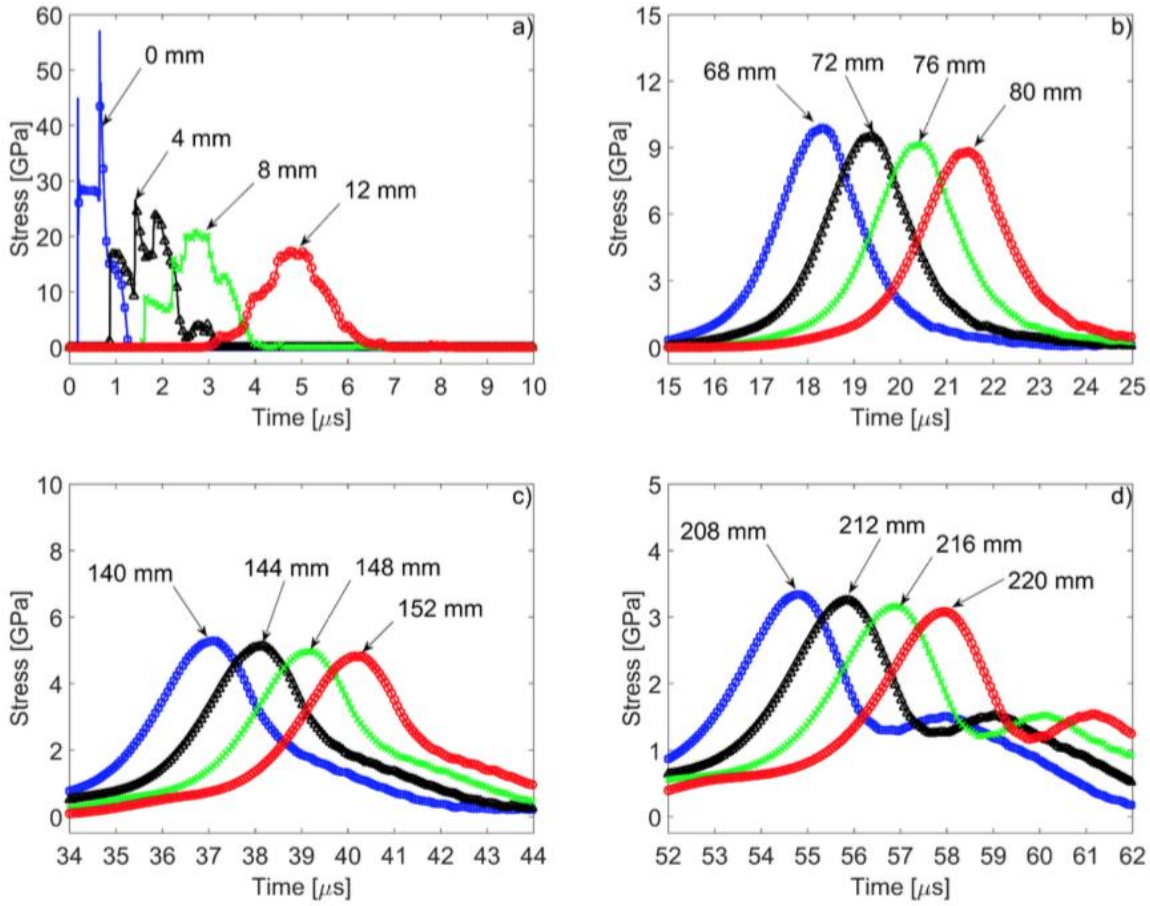

Figure 2-10: Stress pulse evolution in 2 + 2 laminate; data correspond to the interfaces of Al-W layers at different depths: (a) 0, 4, 8, and 16 mm; (b) 68, 72, 76, and 80 mm; (c) 140, 144, 148, and 152 mm; (d) 208, 212, 216, and 220 mm. The pulse was generated by the impact of a 2-mm Al plate at a velocity of 2800 m/s.

In this case, the solitarylike waves with low amplitudes at depths 68–80 mm have a FWHM = 2 cell sizes and a 0.1–0.9 ramp size (Δ) equal to 1.9 cell size.

It is important to compare localized pulses with similar amplitude propagating in a laminate with the same mesostructure, but excited with different initial conditions (impact by 2-mm Al plate versus 8-mm Al plate).

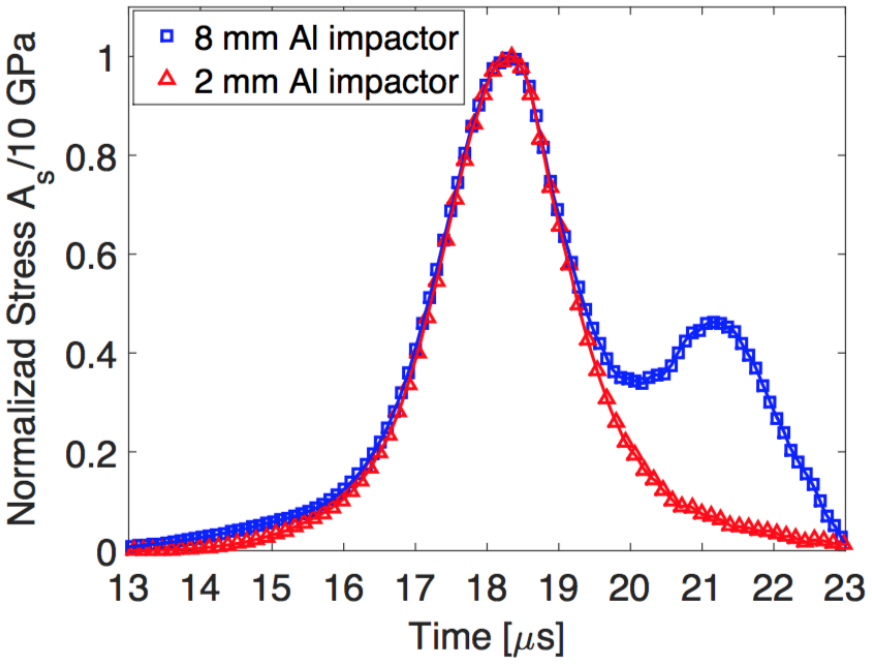

Figure 2-11: Comparison of shapes of solitarylike wave and leading part of the pulse both formed in 2 + 2 laminates with real dissipative properties excited by impact of an Al plate with different thickness, 2 and 8 mm, correspondingly.

Figure 11 presents this comparison. It is evident that the resulting attenuating localized pulse has a direct relation to the laminate mesostructure. It is interesting that the rising parts of the localized pulses in the 2 + 2 laminate are almost identical though they were excited by impacts of 8- and 2-mm Al plates.

2.3.7 1 + 1 Al-W laminate, impact by 2-mm Al plate

It is interesting to study if the localized pulses will be observed in laminates with different cell sizes under identical impact conditions (2-mm Al plate with velocity 2800 m/s) and if their space scale is scaled with the cell size also. The previous case with impactor to cell time ratio of 0.6 (2 + 2 laminate) resulted in a single solitarylike wave (Fig. 10).

Based on what has been observed in the 2 + 2 laminates impacted by 2- and 8-mm Al impactors, we can expect the formation of one or more solitarylike waves. In the case with a 1 + 1 laminate, impacted by a 2-mm Al impactor, the time ratio is 1.3. Figure 12 demonstrates that this laminate indeed supports the single solitarylike wave. The localized pulse is completely formed at a depth of about 8 mm [Fig. 12(a)] compared to 24 mm in the case of a 2 + 2 laminate impacted by the same 2-mm Al plate [compare Figs. 12(a) and 10(a) at the similar depths]. It is interesting that decrease of cell size by two times resulted in the three-times decrease in the travel distance required to form a solitarylike pulse.

It is clear that the shape of the pulse closely resembles a classic solitary wave (bell shape) at a relatively high amplitude of the maximum stress. At lower stress levels [below 5 GPa, Figs. 12(c) and 12(d)], an elastic precursor can be clearly identified and the shape of the wave does not resemble a classic solitary wave and the pulse propagates as an attenuating oscillatory wave. This is consistent with what was observed in the 2 + 2 laminate at low stress levels [Figs. 10(c) and 10(d)]. This occurrence can be explained by the unbalance that exists

between the nonlinearities and dispersion at low stress levels. Similar to what was observed before, at low amplitudes at depths of 68–80 mm, the FWHM = 1.8−2 cell sizes and Δ = 1.7−1.9 cell size, which is consistent with the scaling phenomena observed in past cases impacted by a 2- or 8-mm Al plate.

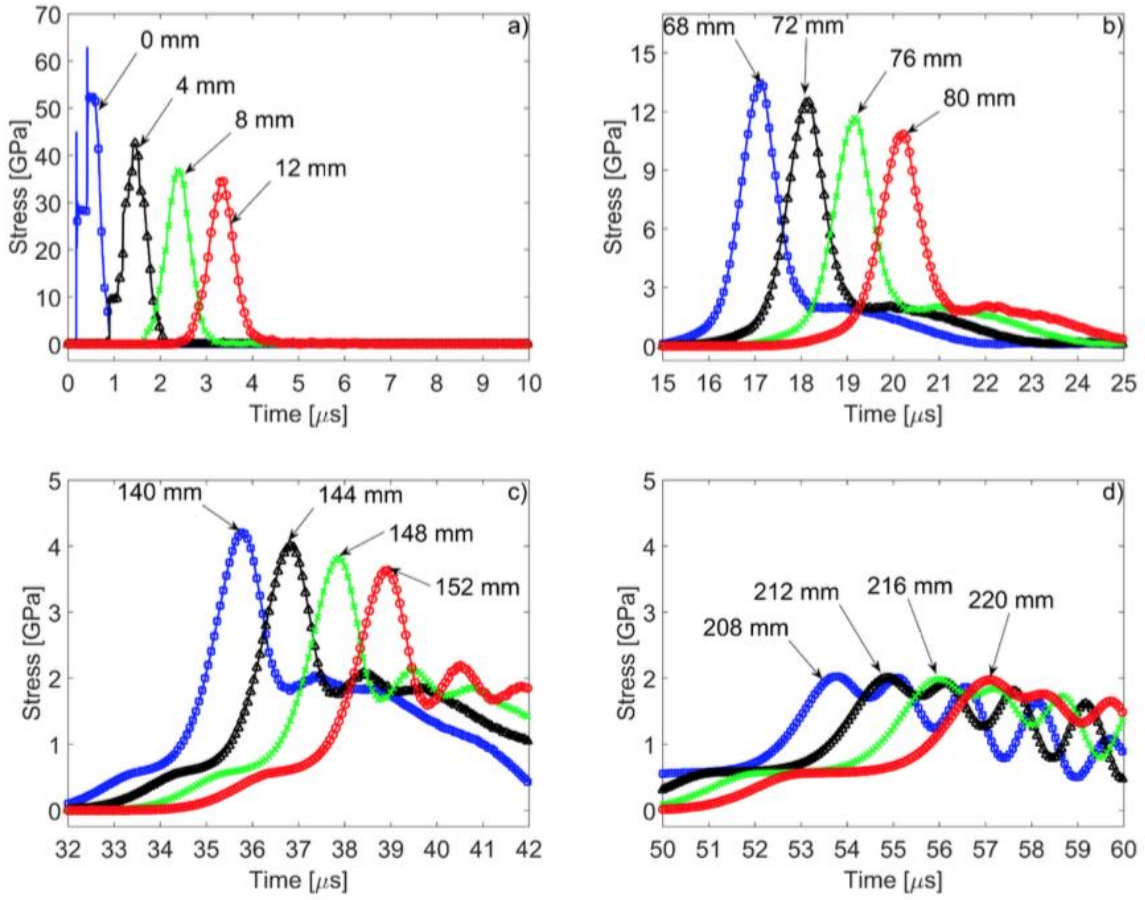

Figure 2-12: Stress pulse evolution in 1 + 1 laminate; data correspond to the interfaces of Al-W layers at different depths: (a) 0, 4, 8, and 12 mm; (b) 68, 72, 76, and 80 mm; (c) 140, 144, 148, and 152 mm; (d) 208, 212, 216, and 220 mm. The pulse was generated by the impact of a 2-mm Al plate at a velocity of 2800 m/s.

The incoming pulse was quickly transformed into a solitarylike wave at depths of 8 and 12 mm, and at larger depths we observe a leading solitarylike wave followed by a compression tail, if the amplitude of the former was above 10

GPa. This resembles the behavior of a discrete, strongly nonlinear granular chain [31,32] except that strong nonlinearity resulted in decoupling of the leading solitary wave from the compression wave, the latter being converted into a shock wave. The difference between the speed of a solitarylike wave and a compression wave with smaller amplitude in the Al-W laminate is not as large as in a strongly nonlinear granular chain preventing fast coupling of these waves before emerging of the elastic precursor. We can expect a similar behavior if one of the components in the laminate exhibits a strongly nonlinear behavior.

2.3.8 0.5 + 0.5 Al-W laminate, impact by 2-mm Al plate

Laminates (2 + 2 and 1 + 1) impacted by a 2-mm Al plate have shown the capability to form and propagate localized solitarylike pulses (Figs. 10 and 12). It is interesting to investigate if a 0.5 + 0.5 laminate will also support a single solitarylike pulse or their train and what is the travel distance necessary for their formation when impacted by a 2-mm Al flyer plate. In the case where the solitary wave is supported by this laminate, it is interesting to see its shape and characteristic space scale in relation to the cell size and rate of amplitude decay.

The ratio of the characteristic duration of the incoming pulse to the laminate time scale introduced by the mesostructure for this case is 2.5 which is identical to the case of a 2 + 2 laminate impacted by an 8-mm Al plate (Fig. 2). Therefore it is natural to expect the formation of a single solitarylike wave with a small tail behind

if the mentioned time ratio is the main parameter determining the outcome of impact. Evolution of the generated pulse is shown in Figs. 13(a) and 13(d)].

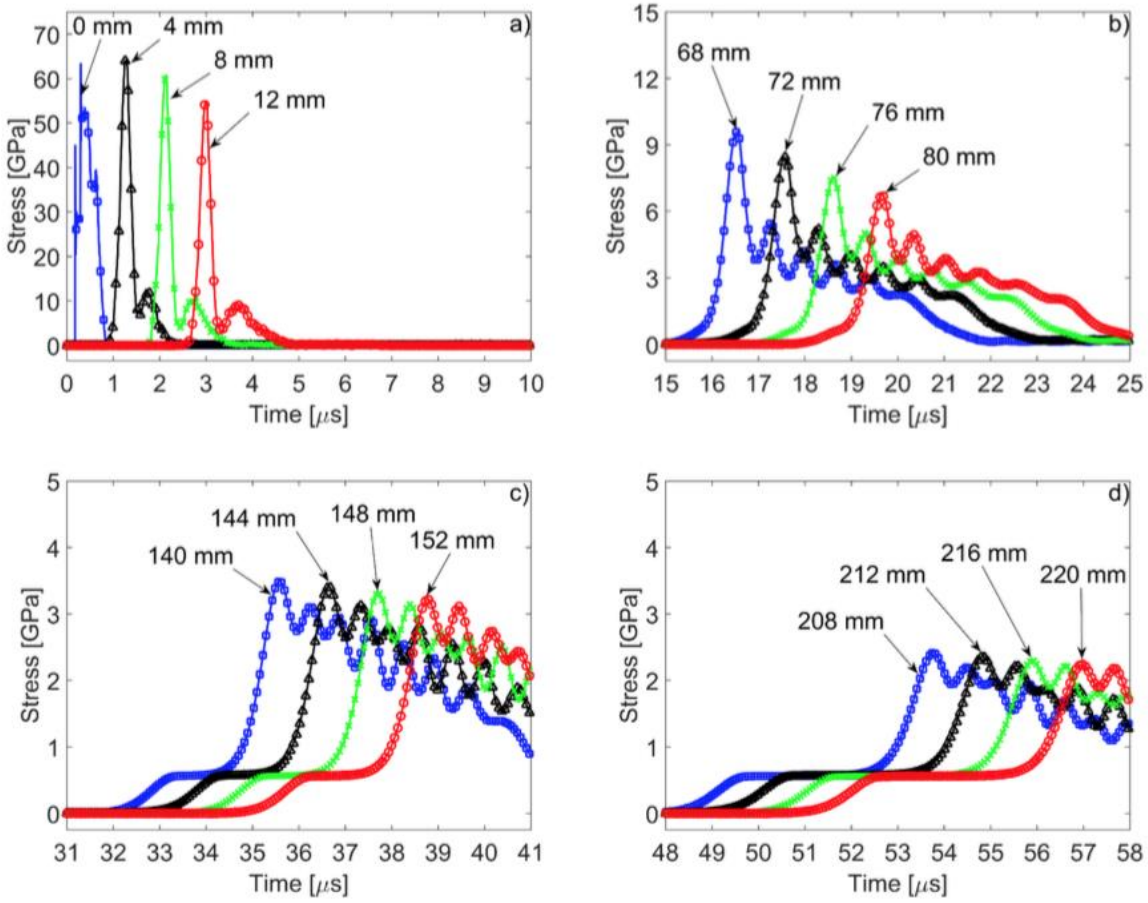

Figure 2-13: Stress pulse evolution in 0.5 + 0.5 laminate; data correspond to the interfaces of Al-W layers at different depths: (a) 0, 4, 8, and 12 mm; (b) 68, 72, 76, and 80 mm; (c) 140, 144, 148, and 152 mm; (d) 208, 212, 216, and 220 mm. The pulse was generated by the impact of a 2-mm Al plate at a velocity of 2800 m/s.

We can see that the incoming pulse was transformed into a fast attenuating leading solitarylike wave followed by a compression wave at a distance of about 4 mm away from the impacted end [Fig. 13(a)]. It is interesting that the traveled distance required to form a solitarylike pulse at the same characteristic duration of the incoming pulse (thickness of impactor) is scaled with the cell size; compare the

shapes of pulses in the 0.5 + 0.5 laminate at a traveled distance of 4 mm [Fig. 13(a)] in the 1 + 1 laminate at a distance of 8 mm [Fig. 12(a)], and in the 2 + 2 laminate at a distance of 16 mm [Fig. 10(a)].

This behavior resembles the formation of a two wave struc- ture in a discrete, strongly nonlinear granular chain [31,32] except that a strongly nonlinear interaction between grains resulted in the decoupling of a leading solitary wave from the compression wave, the latter being converted into a shock wave. The absence of separation of these waves in our case is probably due to a relatively small difference between the speed of a leading solitarylike wave and following it, a compression wave with smaller amplitude in the Al-W laminate in compar- ison with corresponding speeds in a strongly nonlinear chain. We can expect a similar behavior if one of the components in the laminate exhibits a strongly nonlinear behavior.

The strong attenuation of the leading pulse and probably dispersion prevents the formation of a train of localized stress pulses and creates an attenuating oscillatory shock–like profile [Figs. 13(b) and 13(d)] already evident at distances of about 68 mm. At very low stress levels (around 4 GPa) an elastic precursor dramatically changing the shape of the propagating pulse can be observed [Fig. 13(c) and 13(d)], similar to a previous case [Figs. 12(c) and 12(d)], although in the case of the 1 + 1 laminate, the elastic precursor appears closer to the impacted end. In this laminate, the scaling of the characteristic sizes of the

localized pulse can be observed. At 68–72 mm depth, FWHM = 1.8 − 2.2 cell size and Δ = 2.1−2.2 cell sizes.

2.3.9 Comparison of solitarylike wave shapes created by different initial conditions

It is interesting to compare solitarylike waves with similar amplitudes in the same laminate resulting from different initial conditions caused by impactors with different thicknesses. If these waves generated by different initial conditions are quasistationary and similar then it may indicate that they are the result of balancing nonlinear and dispersive properties of the material, as in the case with true solitary waves.

In Figs. 14(a) and 14(b)] normalized profiles of solitarylike waves with similar amplitudes propagating in the Al-W laminates (1+1 and 0.5+0.5) with different dissipative properties, excited by Al impactors with thickness of 8 and 2 mm, are presented. The profiles and durations of the corresponding incoming stress are quite different; for example, the total durations of incoming pulses presented in Figs. 7(a) and 12(a) are 2.35 and 0.74 microseconds, correspondingly.

Four solitarylike waves in normalized coordinates (distance divided by cell size) with very close stress amplitudes are shown in Fig. 14. Figure 14(a) represents the wave profiles propagating in 1 + 1 and 0.5 + 0.5 laminates with real dissipative properties and similar maximum stresses close to 35 GPa, which were generated by the impact of Al flyer plates with thicknesses of 2 and 8 mm. The

respective traveling distances to reach similar amplitudes in these pulses are 40 and 104 mm (1+1 laminate) and 32 and 120 mm (0.5+0.5 laminate).

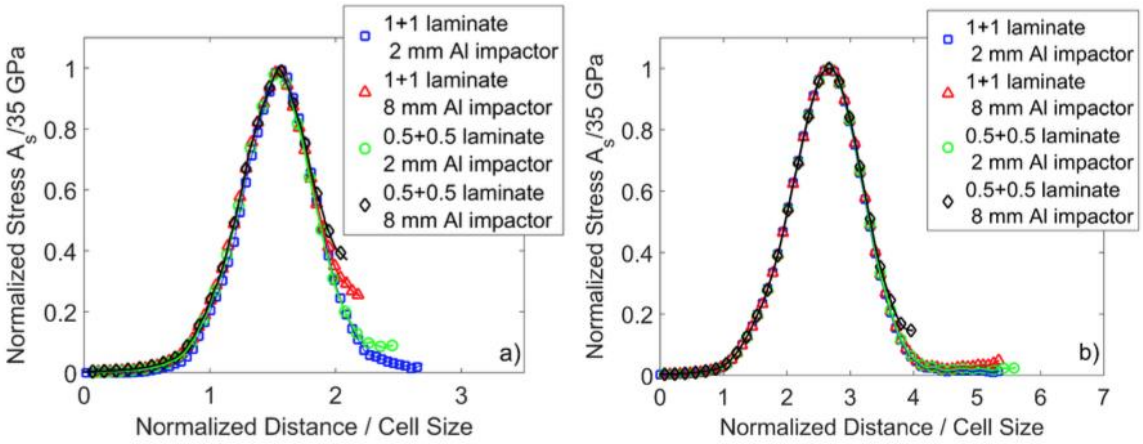

Figure 2-14: Comparison between the profiles of stress in solitarylike waves with similar amplitudes in Al-W laminates with different cell sizes and dissipative properties generated by two different impactors with thickness of 2 and 8 mm, respectively. The stress is normalized by the following wave amplitudes: (a) Lamanites with real dissipative properties: 1+1 laminate, impacted by 2-mm Al plate, stress amplitude 34.9 GPa; 1+1 laminate, impacted by an 8-mm Al plate, stress amplitude 34.8 GPa; 0.5+0.5 laminate, impacted by a 2-mm Al plate, stress amplitude 35.2 GPa; and 0.5+0.5 laminate, impacted by an 8-mm Al plate, stress amplitude 35 GPa. (b) Laminates with artificially low Y_{max}. 1+1 laminate, impacted by a 2-mm Al plate, stress amplitude 35.2 GPa; 1+1 laminate, impacted by an 8-mm Al plate, stress amplitude 35.9 GPa; 0.5+0.5 laminate, impacted by a 2-mm Al plate, stress amplitude 35 GPa; and 0.5+0.5 laminate, impacted by an 8-mm Al plate, stress amplitude 35 GPa.

Wave profiles with a stress amplitude of about 35 GPa are presented in Fig. 14(b) corresponding to the laminates with reduced dissipative properties (smaller Y_{max}), but with the same mesostructure as in Fig. 14(a). These profiles were formed at depths of 182 mm (1 + 1 laminate), 90 mm (1 + 1 laminate), 60 mm (0.5 + 0.5 laminate), and 92 mm (0.5 + 0.5 laminate), correspondingly, where these quasistationary pulses had similar stress amplitudes.

The comparison among the profiles of these waves demonstrates that they are similar in normalized coordinates despite differences in their dissipative

properties. For the case of the laminate with real properties, the FWHM = 1.3 and for the material with small Y_{max}, FWHM = 1.3. This comparison confirms that these waves indeed are a result of the material properties (balancing dispersion caused by the periodic mesostructure and nonlinearity) and do not depend on the initial conditions that generated them, similar to properties of true solitary waves.

2.3.10 Head-on collision of solitarylike waves

One of the main properties of true solitary waves is that they preserve their shapes after collision [9,16]. It is interesting if the solitarylike waves described in the previous section behave in a similar way. To investigate collisions of solitarylike waves the 2 + 2 laminate with real material properties was impacted on both ends as shown in Fig. 15. The length was L_c = 202 mm. The impactor's thickness was L_i = 6 mm. They had velocities V_a = 3500 m/s and V_b = 3200 m/s

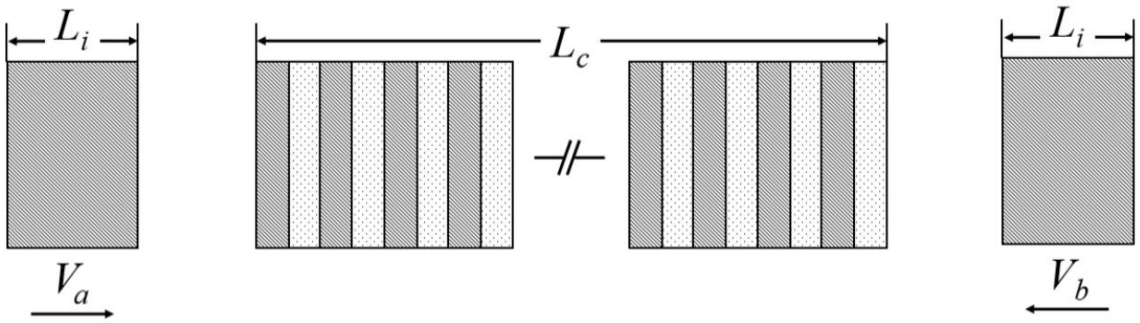

Figure 2-15: Laminate impacted at both ends to investigate collision of solitarylike waves.

Figures 16(a) and 16(b) show both localized waves before collision at 60 mm from the impacted ends. It is clear that they have an almost symmetrical shape

with small amplitude tails. The difference in their amplitudes is caused by the different velocities of impactors on corresponding ends.

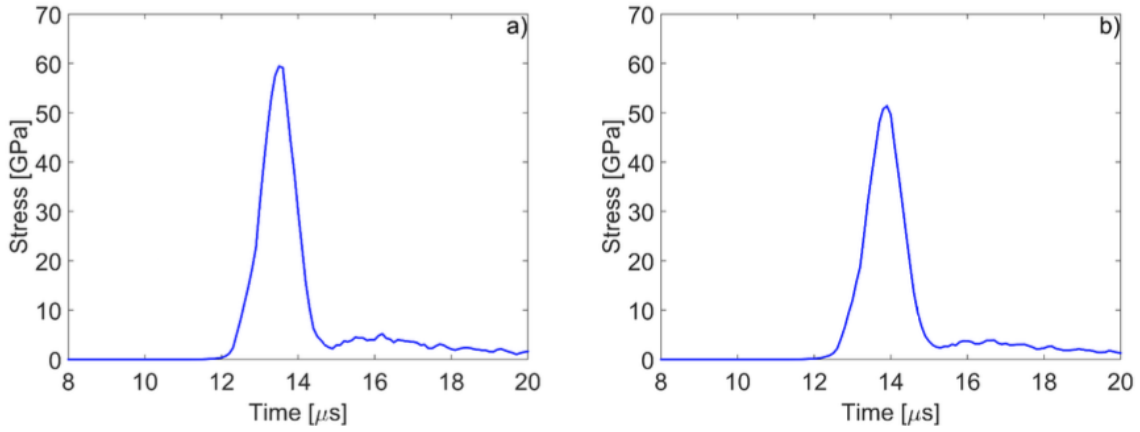

Figure 2-16: (a) Traveling wave at 60 mm depth from the left end of the laminate with real properties. (b) Traveling wave at 60 mm depth from the right end of the laminate. Both waves are shown before collision.

Figure 17 corresponds to the depths 101 mm from both ends of the laminate with real properties where the two waves propagating in the opposite directions meet. The amplitude of the resulting pulse is increased as well as the amplitude of the tail; its duration was close to the durations of the pulses before collision.

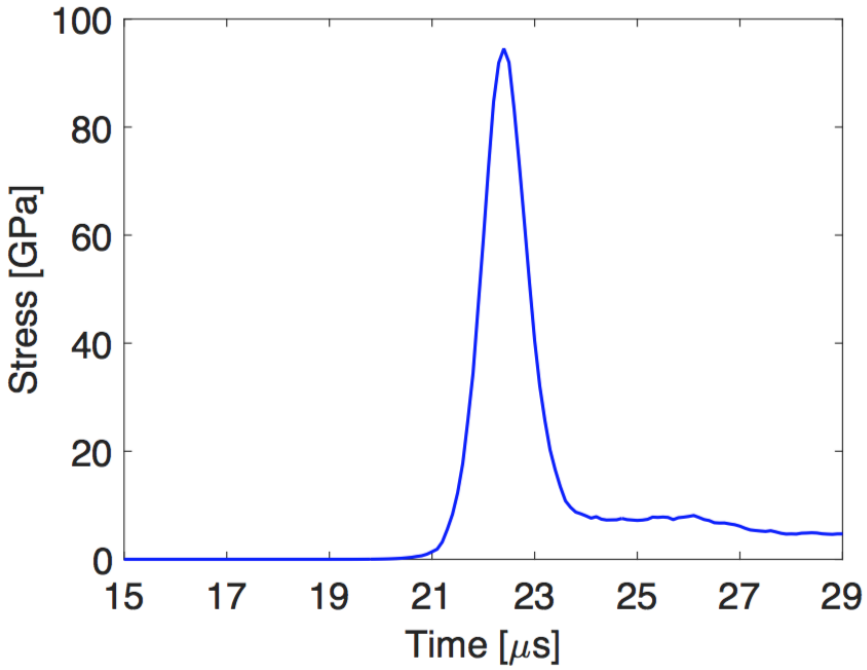

Figure 2-17: Resulting pulse due to collision of two waves propagating in the opposite direction at the middle of the laminate (at 101 mm depths from both ends).

Pulses after their collision are shown in Figs. 18(a) and 18(b) at distances 142 mm from the corresponding ends. We can see that after collision we have two localized waves with different amplitudes, which are smaller than the amplitudes before collision (Fig. 16), mostly because waves decay by traveling additional distances. It should be mentioned that the amplitudes of tails increased after collision due to dissipation.

Collisions of true solitary waves result in a phase shift [9,16]. To investigate if the phase shift is also characteristic for the collision of solitarylike waves, we compare two initially identical solitarylike waves created by the impact on the left end [shown in Fig. 16(a)], but traveling the same distance without collision. Figure

19(a) presents a comparison of the same wave traveling without collision and after a head-on collision at 122 mm from the left end. These two waves are superposed in Fig. 19(b) to demonstrate their similar profiles.

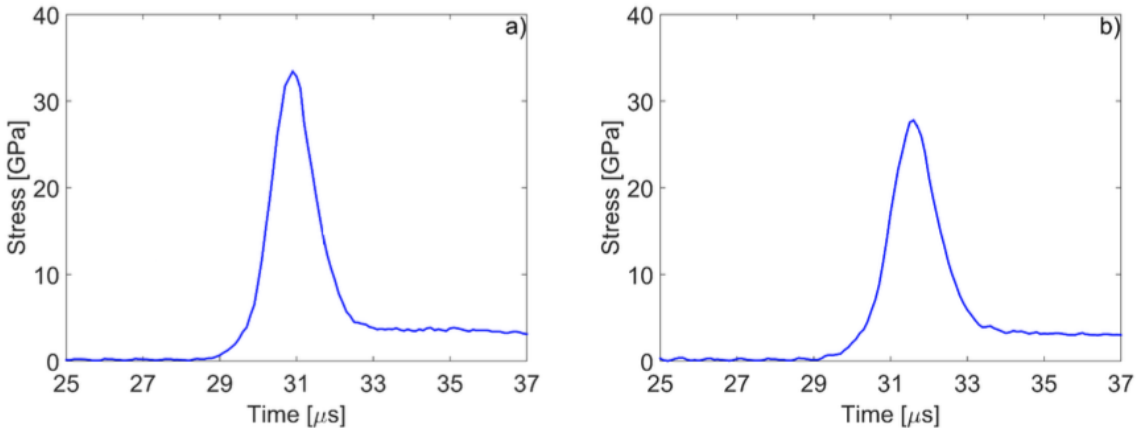

Figure 2-18: (a) Traveling wave at 142 mm depth from the left end of the laminate with real properties. (b) Traveling wave at 142 mm depth from the right end of the laminate. Both waves are shown after collision.

From Fig. 19(a) it is clear that a phase shift has occurred after collision, similar to the phase shift observed after collision of true solitary waves. The two superposed waves in Fig. 19(b) demonstrate that they are very similar resembling the behavior of classic solitons, which completely reconstruct their shapes after collision. The difference between these solitarylike waves and true solitary waves is caused by the decay of the former due to the significant influence of dissipation at this level of stress.

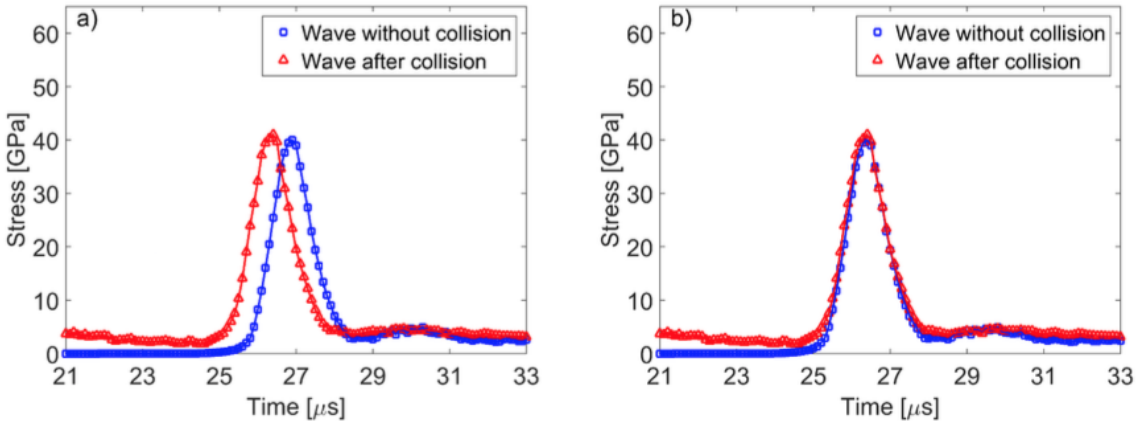

Figure 2-19: (a) The phase shift between two initially identical solitarylike waves created by the impact on the left end traveling the same distance of 122 mm without collision and after head-on collision; (b) the same waves are superposed to demonstrate their similar profiles.

2.4 Theoretical Approach

The considered laminate material has a periodic structure and also exhibits significantly nonlinear behavior mostly due to nonlinearity in a constitutive equation. A combination of these properties supports the propagation of solitarylike waves under certain conditions of dynamic loading as observed numerically in the previous sections. The papers [16,17,20–22] introduce long wave approximation resulting in a Boussinesq-like wave equation to describe propagation of nondissipative solitarylike wave in laminates with relatively small dynamic elastic strains, about 10^{-2}. Nonlinearity in these papers was introduced based on nonlinear elasticity.

In this section we will combine dispersive and nonlinear properties of laminates incorporating them into a KdV-type equation, which supports solitary waves, and compare them with results of numerical calculations of a discrete

system. Of course this approach, especially when it results in a stress pulse with dimensions comparable to the cell size of the laminate, needs verification by numerical calculations of a real discrete system. But if successful, it provides the scaling dependence of the parameters of a localized solitarylike stress pulse of high amplitude on physical and geometrical parameters of laminates.

The dispersion relation for laminated materials can be found in [29]; this expression considers the multiple reflections at the interfaces in the laminated material.

$$\cos(kd) = \cos\left(\frac{wd_a}{C_a}\right)\cos\left(\frac{wd_b}{C_b}\right) - \frac{1}{2}\left(\frac{Z_a}{Z_b} + \frac{Z_b}{Z_a}\right)\sin\left(\frac{wd_a}{C_a}\right)\sin\left(\frac{wd_b}{C_b}\right), \qquad (11)$$

where k is the wave number, w is wavelength, d_a and d_b are the respective sizes of each layer, cell size $d = d_a + d_b$, C_a and C_b refer to the respective sound speed in each layer, and Z_a and Z_b represent the respective impedances for each layer ($Z_i = \rho_i C_i$).In the limit of long wave approximation, $\lambda \gg d$, we get the following dispersion relation:

$$w^2 = \frac{k^2 d^2}{\left[\frac{d_a^2}{c_a^2} + \frac{d_b^2}{c_b^2} + \left(\frac{Z_a}{Z_b} + \frac{Z_b}{Z_a}\right)\left(\frac{d_a d_b}{C_a C_b}\right)\right]}\left[1 - \frac{k^2 d^2}{12}\right] = C_0^2 k^2\left(1 - \frac{k^2 d^2}{12}\right). \qquad (12)$$

The first term in Eq. (12) provides an explicit expression for C_0 for the laminate material, which is equivalent to the averaging approach presented in [16],

$$C_o^2 = \frac{d^2}{\frac{d_a^2}{c_a^2} + \frac{d_b^2}{c_b^2} + \left(\frac{Z_a}{Z_b} + \frac{Z_b}{Z_a}\right)\left(\frac{d_a d_b}{C_a C_b}\right)}. \qquad (13)$$

In our numerical calculations, which included dissipation and more than one order of magnitude larger strains than in [16,17,20–22] (about 10−2) we also

observed solitarylike, slowly attenuating localized waves. But at these much higher strains it is more appropriate to introduce nonlinearity using the Hugoniot relation. Hugoniot parameters naturally reflect the nonlinear properties of materials because the shock wave is a typical example of the phenomena supported by a combination of nonlinear and dissipative properties. It should be mentioned that temperatures in solitarylike waves are smaller compared to shock temperatures at similar stress amplitudes, but because in- put of temperature to the stress at a given specific volume is relatively small, the use of the Hugoniot curve is appropriate. To introduce nonlinearity in the constitutive equation for each of the materials in the laminate we consider the Hugoniot curves [Eq. (14)] in stress versus strain coordinates for Al and W and their corresponding approximations using the second powers of strains [Eq. (18)]. The stress along the Hugoniot is defined as

$$P = \frac{C_o^2(V_o - V)}{[V_o - s(V_o - V)]^2}, \tag{14}$$

where Vo and V correspond to the specific volume of the material at initial and deformed configuration, respectively, and s refers to the first coefficient of the Hugoniot curve on the D−u plane (shock-particle velocity relation) which has the form

$$D = C_0 + su. \tag{15}$$

In this equation a single coefficient s is representing nonlinear behavior of the material in shock wave conditions. Strain in the shock wave in terms of specific volume can be written as

$$\epsilon = \frac{V_o - V}{V_o}. \quad (16)$$

By combining Eqs. (14) and (16) we obtain the Hugoniot stress-strain relation

$$P = \frac{C_o^2}{V_o}\left[\frac{\epsilon}{(1 - s\,\epsilon)^2}\right]. \quad (17)$$

At relatively low values of strains (below 0.15 for Al and 0.1 for W) we can approximate the behavior of Al and W using the following equation with corresponding coefficients:

$$P = \frac{C_o^2}{V_o}[\epsilon(1 + 2s\epsilon)]. \quad (18)$$

The Hugoniot curves and their approximations by Eq. (18) are presented in Figs. 20(a) and 20(b). For comparison, zero Kelvin compression curves, isentrope (Al [30], W estimated from [34]), and curves based on third order elastic constants are also presented. The latter ones are described by the following equation:

$$\sigma = \gamma\epsilon + \frac{\beta}{2}\epsilon^2, \quad (19)$$

where coefficients γ and β are defined by

$$\gamma = \lambda + 2\mu, \quad (20)$$

$$\beta = 3(\lambda + 2\mu) + 2(A + 3B + C), \quad (21)$$

where λ and μ are the Lamé parameters and A, B, and C are the third order elastic constants [35].

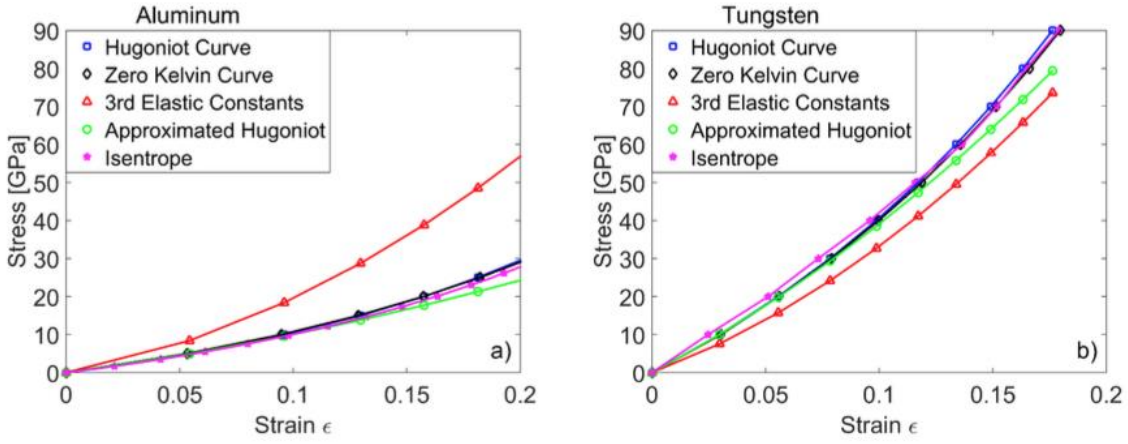

Figure 2-20: Nonlinear stress-strain relations for Al (a), and W (b) based on Hugoniot curves, static compression based on third order elastic constants, zero Kelvin curves, isotherm and approximation of Hugoniot curves using terms only with second power law of strains, Eq(16).

It is clear that using third order elastic constants in our range of stresses is not adequate. At the same time deviation of stresses on the Hugoniot curve from the values corresponding to zero Kelvin curve at the same strains are within a few percent for Al and W at stresses below 40 GPa (strains below 0.25 for Al and below 0.1 for W). Thus we can use the Hugoniot curves approximated by Eq. (18) as a reasonable representation of isentropic behavior. It is appropriate taking into account that on the steady state of the propagation of localized stress pulses materials experience isentropic compression paths, which are between the zero Kelvin curve and Hugoniot states. It should be emphasized that we are looking for a nondissipative description of the single stress pulse despite existing dissipation at this level of stress. Results of numerical calculations presented above demonstrate that dissipation, resulting in the pulse attenuation, does not change

the nature of the pulse coming from a balance of nonlinearity and dispersion similar to the case of strongly nonlinear solitary waves in granular lattices [9].

To find the nonlinearity coefficient in the stress-strain relation for the laminate material we consider its single cell with unit area as depicted in Fig. 21.

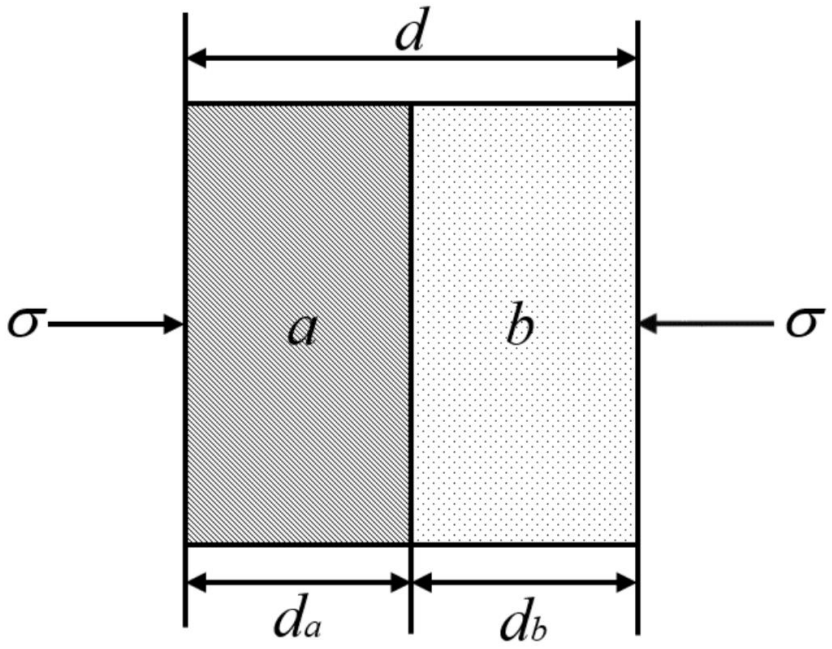

Figure 2-21: Single cell with unit area made of material a and b.

We need to find constants K_{eq}, α_{eq} describing the behavior of the unit cell under compression with effective total strain ϵ_t. We define the total strain of the deformed cell as:

$$\epsilon_t = \frac{(d_{Al}+d_W)-(d_{Al_o}+d_{W_o})}{d_{Al_o}+d_{W_o}} = \frac{d_{Al}-d_{Al_o}}{d_{Al_o}+d_{W_o}} + \frac{d_W-d_{W_o}}{d_{Al_o}+d_{W_o}} = \epsilon_a \left(\frac{d_{Al_o}}{d_{Al_o}+d_{W_o}}\right) +$$

$$\epsilon_{\mathrm{b}} \left(\frac{d_{W_o}}{d_{Al_o}+d_{W_o}}\right) = \epsilon_{Al}\, \tau + \epsilon_W (1-\tau), \qquad (22)$$

where d_{Al_o}, d_{W_o} represent the original length of Al, W and the symbols d_{Al}, d_W are related to a deformed cell. For the system being in equilibrium, $\sigma_{Al} = \sigma_W = \sigma_t$, where is the force applied to the cell. The equation for a total strain including a nonlinear term quadratic with respect to ϵ^2 is represented by the following expression

$$\sigma_t \approx \frac{K_{Al}K_W}{(1-\tau)K_{Al}+\tau K_W}\epsilon + \frac{(\tau K_W^3 \alpha_{Al}+(1-\tau)K_{Al}^3\alpha_W)}{((1-\tau)K_{Al}+\tau K_W)^3}\epsilon^2, \quad (23)$$

This gives us the expressions for coefficient of nonlinearity α_{eq} and linear elastic modulus K_{eq} representing the global response of the cell

$$\alpha_{eq} = \frac{(\tau K_W^3 \alpha_{Al}+(1-\tau)K_{Al}^3\alpha_W)}{((1-\tau)K_{Al}+\tau K_W)^3}, \quad (24)$$

$$K_{eq} = \frac{K_{Al}K_W}{(1-\tau)K_{Al}+\tau K_W}. \quad (25)$$

Apparently that coefficient of nonlinearity is the same for laminates with the same volume of components. The wave equation, being a long wave approximation of a discrete, nondissipative system and having the same dispersive relation and reflecting nonlinear behavior, is the Boussinesq equation

$$U_{tt} = C_o^2 U_{xx} + \beta U_{xxxx} - \psi U_x U_{xx}, \quad (26)$$

where coefficients and ψ are related to materials parameters in the following way:

$$\beta = \frac{d^2 C_o^2}{12}. \quad (27)$$

Unlike the coefficient of nonlinearity and sound speed which is the same for laminates with the same volume ratio of components, the coefficient of dispersion

depends on the characteristic scale of laminate d. Parameter ψ is the coefficient related to the nonlinear part of the force applied to the cell composed from the elements of the discrete system,

$$\psi = \frac{2\alpha_{eq}C_o^2}{K_{eq}}. \tag{28}$$

This equation can be converted to KdV equation in the same approximation:

$$\zeta_t + C_o\zeta_x + S\zeta_{xxx} + \nu\zeta\zeta_x = 0, \tag{29}$$

$$S = \frac{\beta}{2}, \tag{30}$$

$$\nu = \frac{\psi}{2C_o}. \tag{31}$$

The KdV equation has a solitary wave solution of the form

$$\zeta = \zeta_m \operatorname{sech}^2\left(\left(\frac{\psi\zeta_m}{12\beta}\right)^{\frac{1}{2}}(x - vt)\right). \tag{32}$$

The equation for the full-width at half-maximum (FWHM) of this pulse (w) expressed in terms of the cell size, thicknesses of layers and linear and nonlinear properties of components as well as an amplitude of stress pulse is presented below:

$$FWHM = \frac{1.76dK_{eq}^{1/2}}{\left(2\alpha_{eq}\,\zeta_m\right)^{1/2}}. \tag{33}$$

It is interesting that though the FWHM of the pulse in laminate w is scaled linearly with the cell size d the individual thicknesses of layers are also affecting the size of the solitary wave present in the values of K_{eq} and α_{eq}. It means that laminates with the same cell size d will have different values of w if the thicknesses of individual layers are different.

The speed of the solitary wave is given by

$$V = C_o + \frac{\nu}{3}\zeta_m, \tag{34}$$

$$\nu = \frac{\psi}{2C_o} = \frac{2dC_{Al}^2\rho_{Al}C_W^2\rho_W\left(C_{Al}^6\rho_{Al}^3K_WS_Wd_W+C_W^6\rho_W^3K_{Al}S_{Al}d_{Al}\right)}{K_{Al}K_W\left(C_{Al}^2\rho_{Al}d_W+C_W^2\rho_Wd_{Al}\right)\left(\rho_{Al}d_{Al}+d_W\rho_W\right)}. \tag{35}$$

Now we explore if this approximation satisfactorily de- scribes the shape of solitarylike stress pulses and their speeds observed in numerical calculations.

Figures 22(a)–22(d) present the shapes of stress pulse found in LS-DYNA numerical simulations and KdV solitary wave solution [Eq. (32)] for maximum stresses below 35 GPa where cold curve and isentropic compression are very well approximated by nonlinear equation (18). The pulse shapes generated in the numerical calculations performed with real material properties as well as the one with artificially small Y_{max} are shown in Fig. 22.

We can see that space scales and shapes of stress pulses observed in numerical calculations are satisfactory described by long wave KdV solitary wave solution despite the charac- teristic width of the pulse being close to the cell size and dissipation present in numerical calculations. It should be mentioned that the full width at half maximum (FWHM) for these pulses is only about two cells. The pulse in numerical calculation is narrower than KdV solution, and the FWHM of the KdV solitary wave solution is about 12% larger than the corresponding pulse width in numerical calculations in the case of a solitarylike wave in a 2 + 2 laminate [Fig. 22(c)].

It is interesting to check if a presented solitary wave solution is also a reasonable approximation for a broader range of wave amplitudes, specifically for

significantly larger stresses where nonlinear behavior deviates more significantly from the approximation described by Eq. (18). The corresponding shape of the stress pulse at these stresses is shown in Fig. 23.

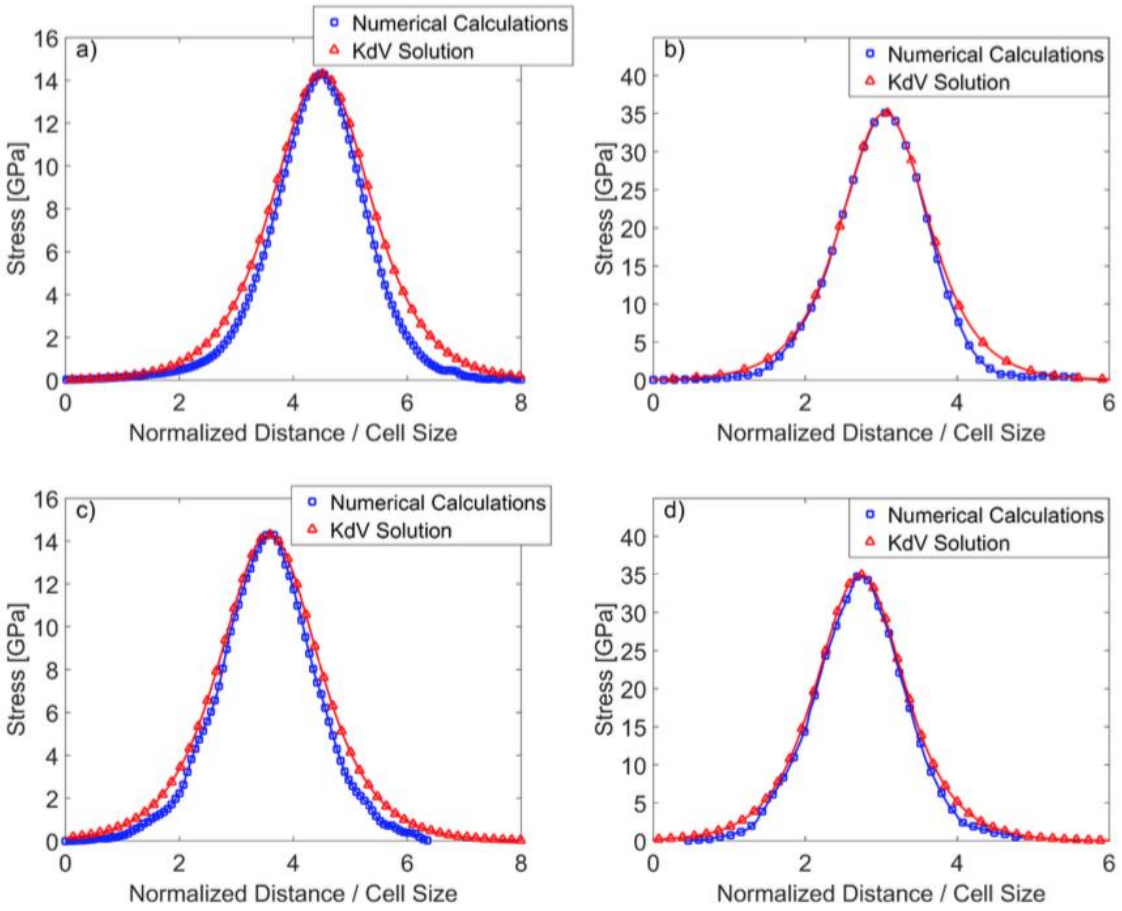

Figure 2-22: Comparison of KdV solitary solution with nonlinearity parameters taken from Hugoniot curve (Eq.18) to the shapes of solitary like waves found on numerical simulations: (a) The wave in numerical simulation corresponding to the depth 72 mm in the 2+2 laminate with artificially small Y_{max} laminate impacted by a 2-mm Al plate with a velocity of 2800 m/s. (b) The wave in numerical simulation corresponding to the depth of 32 mm in the 1+1 laminate with artificially small Y_{max} impacted by a 2-mm Al plate with a velocity of 2800 m/s. (c, d) comparison of waves in corresponding laminates (2+2 and 1+1) with real properties.

The value of FWHM in this case is about one cell size only. It is amazing that the KdV solitary wave, obtained as a solution of a wave equation being a

weakly nonlinear and long wave approximation of a discrete system, is still a satisfactory approximation for the shape of the very short localized pulse observed in numerical calculations. Thus Eq. (33) provides a correct scaling of the size of solitarylike pulses and a reasonable description of their shapes in a very broad range of stress amplitudes.

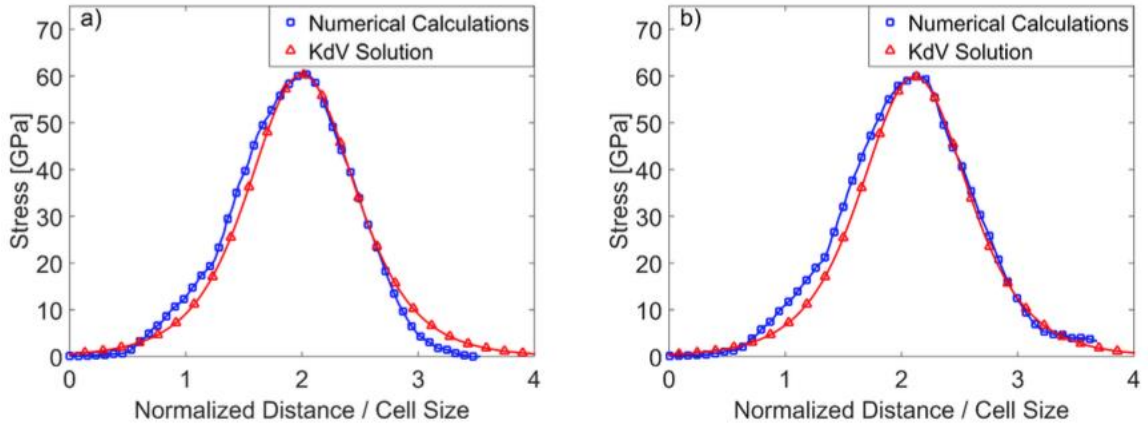

Figure 2-23: Comparison of KdV solitary solution with nonlinearity parameters taken from an approximated Hugoniot curve [Eq. (16)] to the wave found on numerical simulations. The wave in the numerical simulation corresponds to the depth of 132 mm in a 2 + 2 laminate impacted by an 8-mm Al plate with a velocity of 2800 m/s an artificially small Y_{max} (a) and in laminate with real material properties (b).

Another property of KdV solitary waves is a linear dependence of their speed on the stress amplitude [Eq. (34)]. Figure 24 presents a comparison of the dependence of the speed of pulses on the stress amplitude found in numerical calculations for laminates with different cell sizes with a similar dependence for KdV solitary waves [Eq. (34)].

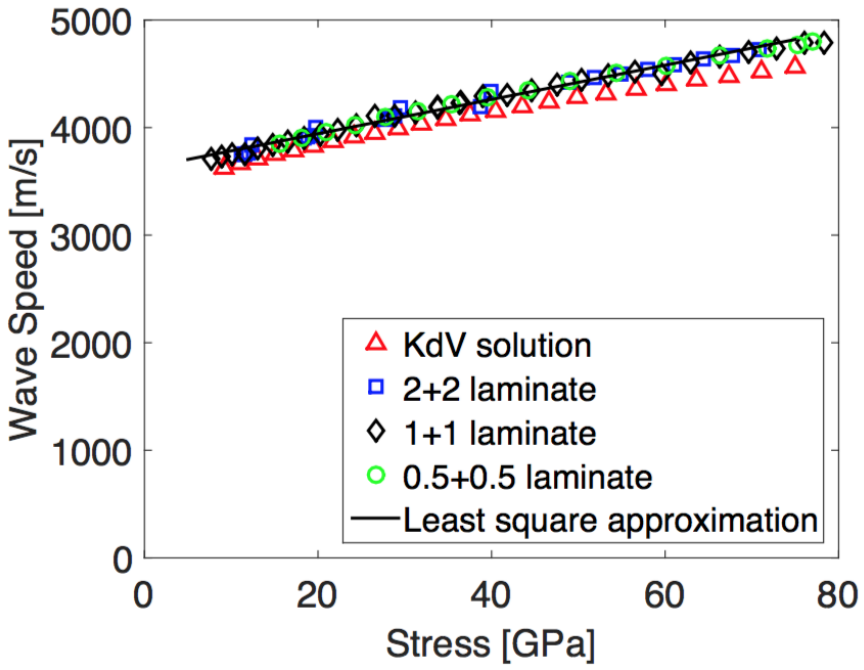

Figure 2-24: Dependence of the speed of the localized wave in Al-W 2+2, 1+1, and 0.5+0.5 laminates found in numerical calculations on maximum stress (on the interface between Al and W) and corresponding Eq. 33 for the speed of KdV solitary wave.

It is clear that the linear relationship between the speed of the pulse and maximum stress found for the KdV solitary wave is a satisfactory approximation in the whole investigated range of stress amplitudes for different laminates. It is important that the speed of the solitarylike wave in numerical calculations is not dependent on the cell size, as can be expected from the proposed analogy with the KdV soliton. It is interesting that at the same cell size, but at different individual thicknesses of layers (determining the relative volume of components) the speed of a solitarylike wave will be different. This dependence is represented by values of Keq and αeq depending on the volume fraction of the components. It means that laminates with the same cell size d will have different values of the slope of

the speed versus stress amplitude if the thicknesses of individual layers are different.

It should be mentioned that sound speed for the laminate, based on Eq. (13), is C_{eq} = 3381 m/s. From the graph presented in Fig. 24 we can see that the speed of the solitary wave in the KdV approximation and also in numerical calculations is larger than the sound speed in the laminate in a long wave approximation; thus this pulse is supersonic with respect to the long wave sound speed in the laminate. However, its speed in the investigated range of stresses is smaller than the sound speed in Al, and at maximum stresses below 30 GPa is also smaller than in W. As a result short wave length disturbances with the space scale compared to the thickness of the layers can escape into the area in front of the propagating pulse leaking the energy from the pulse and contributing to the amplitude attenuation. This mechanism is additional to the dissipation and presents another reason that these propagating pulses are not truly solitary waves despite being satisfactorily described by the KdV soliton solution. This mechanism also contributes to the nonelastic collision of these localized pulses.

2.5 Chapter conclusions

The existence of solitarylike localized waves in lami- nate material Al-W in a broad range of stress amplitude (10–80 GPa) was demonstrated using numerical calculations.

It was shown that the dissipation due to viscoplastic behavior causes significant decay of amplitude of these solitarylike stress pulses, but their space scale and shape are closely approximated by KdV solution.

These solitarylike waves exhibit behavior similar to classical KdV solitons, e.g., a dependence of speed and width on the stress amplitude. The different durations of incoming pulse, with respect to characteristic time scale of the laminate, result in either the formation of only one localized solitarylike wave, a train of such waves, or in an oscillatory shock–like wave. It has also been shown that interaction between these waves results in a phase shift, which is similar to behavior in classic solitons, although it also shows a nonelastic behavior.

A theoretical framework based on a weekly nonlinear KdV equation supporting a solitary wave was presented. To introduce a nonlinearity parameter, readily available shock Hugoniot data were used together with the exact dispersion relation for a linear elastic laminate. The shape and speed of the localized waves found in numerical calculations are in satisfactory agreement with the KdV solitary wave in a broad range of stress amplitudes.

This approach allowed us to arrive at the analytic equation for width and speed of the observed solitarylike stress pulses using nonlinear properties of components and geometry of laminate. It allows the design of layered materials for optimal protection, e.g., to prevent spall, and to understand the nature of pulses propagating under extremely short pulse loading, e.g., produced by powerful lasers.

2.6 Chapter References

[1] R. Kinslow, *High-Velocity Impact Phenomena* (Elsevier, New York, 2012).

[2] S. P. Marsh, *LASL Shock Hugoniot Data*, Vol. 5 (University of California Press, Berkeley, 1980).

[3] R. McQueen, S. Marsh, and J. Fritz, Hugoniot equation of state of twelve rocks, J. Geophys. Res. **72**, 4999 (1967).

[4] S. M. Rytov, Acoustical properties of a thinly laminated medium, Sov. Phys. Acoust. **2**, 68 (1956).

[5] C.-T. Sun, J. D. Achenbach, and G. Herrmann, Continuum theory for a laminated medium, J. Appl. Mech. **35**, 467 (1968).

[6] H. J. Sutherland and R. Lingle, Geometric dispersion of acoustic waves by a fibrous composite, J. Compos. Mater. **6**, 490 (1972).

[7] D. Drumheller and H. Sutherland, A lattice model for stress wave propagation in composite materials, J. Appl. Mech. **40**, 149 (1973).

[8] R. Hofmann, D. J. Andrews, and D. Maxwell, Computed shock response of porous aluminum, J. Appl. Phys. **39**, 4555 (1968).

[9] V. F. Nesterenko, *Dynamics of Heterogeneous Materials* (Springer Science & Business Media, New York, 2001).

[10] C. Wei, B. Maddox, A. Stover, T. Weihs, V. Nesterenko, and M. Meyers, Reaction in Ni-Al laminates by laser-shock com- pression and spalling, Acta Mater. **59**, 5276 (2011).

[11] C. Wei, V. Nesterenko, T. Weihs, B. Remington, H.-S. Park, and M. Meyers, Response of Ni/Al laminates to laser-driven compression, Acta Mater. **60**, 3929 (2012).

[12] V. Nesterenko, V. Fomin, and P. Cheskidov, Damping of strong shocks in laminar materials, J. Appl. Mech. Tech. Phys. **24**, 567 (1983).

[13] V. Nesterenko, V. Fomin, and P. Cheskidov, Attenuation of strong shock waves in laminar materials, *Nonlinear Deformation Waves* (Springer-Verlag, Berlin, 1983), p. 191.

[14] D. Benson and V. Nesterenko, Anomalous decay of shock impulses in laminated composites, J. Appl. Phys. **89**, 3622 (2001).

[15] N. K. Akhmadeev and R. K. Bolotnova, Propagation of stress waves in layered media under impact loading (acoustical approximation), J. Appl. Mech. Tech. Phys. **26**, 114 (1985).

[16] D. H. Yong and R. J. LeVeque, Solitary waves in layered nonlinear media, SIAM J Appl. Math. **63**, 1539 (2003).

[17] J. Engelbrecht, A. Berezovski, and A. Salupere, Nonlinear deformation waves in solids and dispersion, Wave Motion **44**, 493 (2007).

[18] R. D. Mindlin, Micro-structure in linear elasticity, Arch. Ration. Mech. Anal. **16**, 51 (1964).

[19] S. Zhuang, G. Ravichandran, and D. E. Grady, An experimental investigation of shock wave propagation in periodically layered composites, J. Mech. Phys. Solids **51**, 245 (2003).

[20] A. Salupere, K. Tamm, and J. Engelbrecht, Numerical simulation of interaction of solitary deformation waves in microstructured solids, Int. J. Non-Linear Mech. **43**, 201 (2008).

[21] J. Engelbrecht, A. Salupere, and K. Tamm, Waves in microstruc- tured solids and the boussinesq paradigm, Wave Motion **48**, 717 (2011).

[22] I. V. Andrianov, V. V. Danishevskyy, O. I. Ryzhkov, and D. Weichert, Numerical study of formation of solitary strain waves in a nonlinear elastic layered composite material, Wave Motion **51**, 405 (2014).

[23] J. O. Hallquist, ls-dyna *Theory Manual* (Livermore Software Technology Corporation, Livermore, CA, 2006); http://www.lstc.com/pdf/ls-dyna_theory_manual_2006.pdf.

[24] D. Steinberg, S. Cochran, and M. Guinan, A constitutive model for metals applicable at high-strain rate, J. Appl. Phys. **51**, 1498 (1980).

[25] D. Steinberg, *Equation of State and Strength Properties of Selected Materials* (Lawrence Livermore National Laboratory, Livermore, CA, 1996).

[26] L. C. Chhabildas and J. R. Asay, Rise-time measurements of shock transitions in aluminum, copper and steel, J. Appl. Phys. **50**, 2749 (1979).

[27] J. C. Crowhurst, M. R. Armstrong, K. B. Knight, J. M. Zaug, and E. M. Behymer, Invariance of the Dissipative Action at Ultrahigh Strain Rates Above the Strong Shock Threshold, Phys. Rev. Lett. **107**, 144302 (2011).

[28] J. Asay, L. Chhabildas, and D. Dandekar, Shear strength of shock-loaded polycrystalline tungsten, J. Appl. Phys. **51**, 4774 (1980).

[29] E. Lee and W. H. Yang, On waves in composite materials with periodic structure, SIAM J. Appl. Math. **25**, 492 (1973).

[30] G. Kerley, Theoretical equation of state for aluminum, Int. J. Impact Eng. **5**, 441 (1987).

[31] A. Rosas, A. H. Romero, V. F. Nesterenko, and K. Lindenberg, Observation of Two-Wave Structure in Strongly Nonlinear Dissipative Granular Chains, Phys. Rev. Lett. **98**, 164301 (2007).

[32] A. Rosas, A. H. Romero, V. F. Nesterenko, and K. Lindenberg, Short-pulse dynamics in strongly nonlinear dissipative granular chains, Phys. Rev. E **78**, 051303 (2008).

[33] E. B. Herbold and V. F. Nesterenko, Shock wave structure in a strongly nonlinear lattice with viscous dissipation, Phys. Rev. E **75**, 021304 (2007).

[34] L. Chhabildas, J. Asay, and L. Barker, Dynamic quasi- isentropic loading of tungsten, High Press. Sci. Technol. **5**, 842 (1990).

[35] C. Cattani and Rushchitskii, *Wavelet and Wave Analysis as Applied to Materials with Micro or Nanostructure*, Series on Advances in Mathematics for Applied Sciences (World Scientific, Hackensack, NJ, 2007).

Chapter 2, in full, is a reprint of the material as it appears in Physical Review E, Franco Navarro, P., Benson, D.J. and Nesterenko, V.F., American Physical Society 2015. The dissertation author was the primary investigator and author of this paper.

Chapter 3 : Multiple scales of shock waves in dissipative laminate materials

3.1 Introduction

The response of nonlinear materials with periodic microstructure depends on the parameters of the incoming disturbance. For example, short-duration pulses result in solitary waves, longer pulses can produce a train of solitary waves or shocklike stress pulses, and periodic excitations result in strongly nonlinear periodic waves in granular chains [1,2]. The balance of weak nonlinearity and dispersion caused by a periodic microstructure results in small-amplitude solitarylike waves (stegotons) in nondissipative laminates [3]. In Ref. [4] incoming, short, high-amplitude pulses (with respect to the characteristic inner time scale determined by the cell size and the sound speed of components) generated weakly decaying compression solitarylike waves in the dissipative nonlinear Al-W laminate.

In this paper we analyze the transient and quasisteady responses of dissipative Al-W laminates to long-duration, high-amplitude incoming pulses allowing the establishment of steady shock wave profiles and quasiequilibrium states behind the shock front. The response to high-amplitude shock loading of homogeneous materials is usually analyzed assuming that at high-amplitude loading, a steady state behind the shock exists. This approach ignores the transient stage necessary to establish a stationary shock front and does not

account for the possible maximum in stresses reached during the intermediate stages preceding a steady state behind the shock. The establishment of a steady shock wave is assumed to happen when it has propagated for at least a few shock front widths [2,5]. The assumption of a steady shock wave allows the use of conservation laws across the shock front, which results in the Rankine-Hugoniot equations connecting the states behind and in front of the stationary shock wave [5–7]. In laminate materials, the establishment of a steady state behind the wave and steady propagation regime might not occur, as can be seen in the case of short-duration incoming pulses. The examples include powerful laser loading, impact by small thickness plates, or contact explosion [8,9]. Some approaches to create Hugoniot curves for mixtures (with different degrees of success) are reviewed in [10], though they usually do not address the spatial scales of the shocked materials when they are applicable. The assumption that the shock wave has reached a steady state might be incorrect, at least in cases when characteristic duration of the shock wave is about the characteristic time of pulse propagation through the cell [4,11]. The shock wave propagation in finite nonlinear laminates can result in peculiar and counterintuitive effects such as the increase of amplitude of the wave with the decrease of layer thickness; this contradicts the behavior based on the difference of acoustic impedances of linear elastic materials [2,12,13].

The dissipation processes during shock loading and nonlinearity of material behavior determine the width of the shock wave in homogeneous materials [14–17]. In homogeneous materials for strong shock waves, the fourth power law was

established to relate the maximum strain rate and stress behind the shock in the form $\dot{\epsilon} = \alpha\sigma^4$, where $\dot{\epsilon}$ represents the strain rate at the leading front and σ the maximum stress on the leading front. This result was introduced by Grady and a thorough explanation can be found in [18,19]. This fourth power law has been widely adopted in the shock physics community. Nevertheless, experimental results presented in the paper by Zhuang *et al.* [20] demonstrated that this law does not apply to laminate materials. Instead, a second power law, i.e., $\dot{\epsilon} = \alpha\sigma^2$, was proposed to connect the maximum stress and strain rate.

It was shown in [4,11] that the nature of high-amplitude stress waves in dissipative Al-W laminate was determined by the ratio of the duration of incoming pulses to the characteristic time of pulse propagation through the cell ($t_r = {2d_{imp}}/{C_{imp}}/{d_{lam}}/{C_{lam}}$), where C_{lam} is the equivalent sound speed in the laminate; in this paper C_{lam} has a value of 3381 m/s, being the limit of the long-wave approximation expressed by Eq. (4). At small time ratios (t_r < 2.5), numerical calculations demonstrated that the incoming pulse was localized after a propagation distance of about four to five cells. Its properties (speed and shape) were similar to a weakly nonlinear Korteweg–de Vries (KdV) solitary wave. Longer incoming pulses (t_r > 5) were transformed into a train of separated solitarylike waves or into a triangular oscillatory shock profile depending on the level of dissipation. Preliminary results related to the scaling of the shock wave loading can be found in [11].

In this paper we investigate numerically the multiple scales of high-amplitude shock waves generated by the plate impact in Al-W laminates with different mesostructures. We identify three different characteristic time scales presented in Fig. 25 related to the formation of the stationary shock: the time from the impacted end required to establish a stationary shock profile, the width of the leading front determining the maximum strain rate of loading, and the width of the shock wave identified as the time span from the initial state to the final equilibrium (quasiequilibrium) state (slowly attenuating elastic vibrations can still be present as well as differences in the temperatures of Al and W).

The establishment of this stationary wave profile takes some propagation distance depending on the cell size and properties of components. In the first few cells, the leading pulse is still a shock waves in individual components [4,11–13] and not part of a stationary shock wave in the laminate. The transition from the initial to the final equilibrium state in the Al laminate with gaps (modeling porous materials) due to multiple reverberations of shock waves was numerically demonstrated in [14].

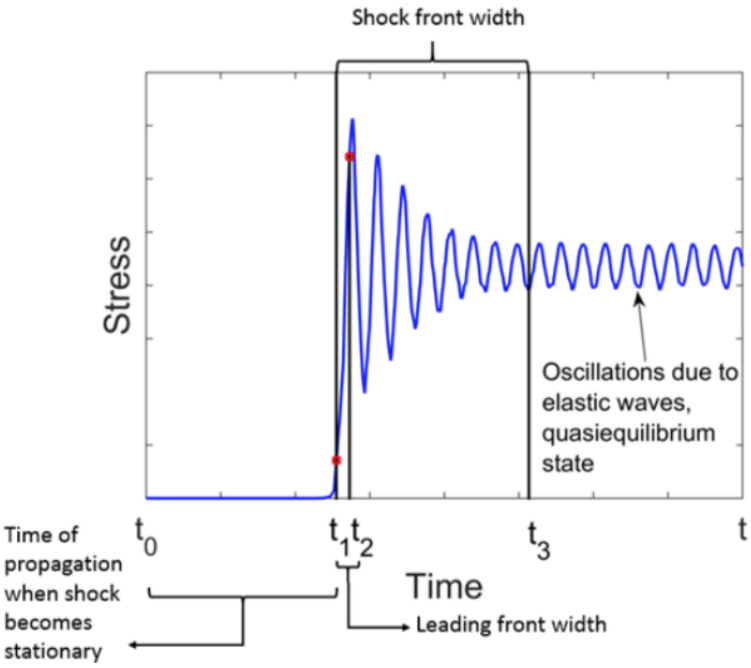

Figure 3-1: Three characteristic time scales related to the established stationary shock profile detected at some point inside the laminate far enough from the impacted end. The three time scales identified in the graph are described as follows: time of propagation $t_1 - t_0$ when shock excited by external disturbance at time t_0 becomes stationary - it has achieved steady amplitude and width of leading front as well as oscillating profile of shock and final state; shock front width $t_3 - t_1$ determined by the time difference corresponding to 0.1 of maximum stress amplitude and time when plastic deformation is replaced by slowly decaying elastic reverberations (quasi-equilibrium state); and leading front width $t_2 - t_1$ determined by time difference between point with 0.1 of maximum stress amplitude and point with 0.9 of maximum stress amplitude. The latter time difference should be used to determine the maximum strain rate in the stationary shock.

The establishment of this stationary wave profile takes some propagation distance depending on the cell size and properties of components. In the first few cells, the leading pulse is still a shock waves in individual components [4,11–13] and not part of a stationary shock wave in the laminate. The transition from the initial to the final equilibrium state in the Al laminate with gaps (modeling porous materials) due to multiple reverberations of shock waves was numerically demonstrated in [14].

The schematic of the shock wave structure presented in Fig. 1, strictly speaking, does not represent a final state due to presence of oscillating elastic waves that have not decayed; this state also has different temperatures in the components. We can characterize this final state as a frozen state with a time scale to reach equilibrium much longer than the characteristic times of wave propagation in practical devices. Nevertheless, the decay of the elastic reverberations and the equilibration of the temperature between the components will probably have only a slight effect on the final stress and particle velocity. The characteristic times related to the attenuation of the elastic oscillations and the even longer time required for thermal equilibrium are not shown in Fig. 1. These characteristic scales might be relevant for the nanolaminates.

The state in the leading front is a transient state and should not be used as the final state of the laminate Hugoniot. It should be mentioned that the Hugoniot curve has no information on the type of dissipative processes leading to the establishment of the final equilibrium state. The parameters that the leading front depends on are the specific dissipative properties of individual components of the laminate and, depending on them, it can be different with the same final equilibrium state.

It was demonstrated that in the investigated Al-W laminate that the width of the leading front (and subsequently time interval $t_2 - t_1$) is mostly determined by the laminate's mesostruc- ture, nonlinear parameters of components, and amplitude of the shock. This time scale can be related to the characteristic scale

of the solitarylike wave observed in [4] that is satisfactorily de- scribed by the Korteweg–de Vries approximation [4,11]. The critical level of dissipation corresponding to the transition of an oscillatory to a monotonic shock (as in Fig. 1) is determined by the amplitude of the wave and the dispersive properties of laminates similar to the stress wave profiles in discrete dissipative granular chains [1,2]. The dissipation affects the width of the shock front, during which multiple loading cycles bring the laminate into a final quasiequilibrium state. This time scale is of the same order as the propagation time to form a stationary shock wave in the investigated Al-W laminate.

It is appropriate to mention that the shock wave solution of the KdV equation with viscous dissipation has two space scales. For weak dissipation, the shock front width is determined by the nonlinear effects and depends on the shock amplitude and the dispersion coefficient, unlike the characteristic size of the shock front width that is determined by viscous dissipation and dispersion. The characteristic size of the oscillations behind the shock front is of the same order as the width of the leading front width.

3.2 Simulations

One-dimensional numerical calculations were performed using LS-DYNA, a general-purpose finite-element program [21] used in [4]. The material response was modeled with the Steinberg-Guinan plasticity model coupled with Grüneisen’s equation of state [22,23]. The experimental results of the homogeneous materials

(Al and W) were compared to the results of the numerical calculations to verify the agreement of temperature and stresses at the final state of the material behind the shocks with published Hugoniot data.

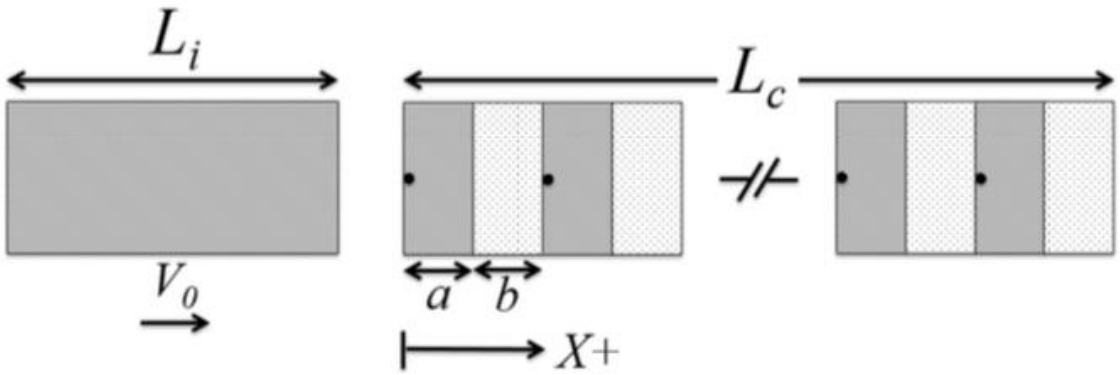

Figure 3-2: Geometry of laminate Al/W material. Black dots indicate points in Al layers adjacent to the interfaces where the stress is calculated.

The components in the laminates (see Fig. 2) had equal thicknesses (a = b) with values of a and b equal to 2, 1, and 0.5 mm. All the layers were modeled as perfectly bonded, which is an appropriate assumption for compression wave loading. In this paper striker plates with relatively large thicknesses (L_i = 80 and 800 mm) were used to create long-duration incoming pulses with a time ratio tr ranging from 25 to about 1000.

The mesh size in all cases was equal 1×10^{-5} m = 0.01mm and the selected artificial viscosity resulted in a shock width in Al and W at least ten times smaller than the smallest layer size (0.5 mm). This ensures that a steady state is reached behind the shock waves when they propagate inside each layer during the initial stage of the pulse formation following the impact. Of course, it is desirable that the

numerical shock width is similar to the one found in experiments [24,25], but the width of the shock front is not important for the parameters of the final state as long as the shock width is sufficiently smaller than the layer thickness. This ensures that the material reaches Hugoniot states at each shock loading. The Hugoniot states are characteristic of stationary shocks and are independent of the specific mechanisms of dissipation defining the width of the transient zone and the resulting final equilibrium state. In our calculations the plastic shock width (Δx) and the rise time (Δt) are: Aluminum Δt = 3.72x10^{-9} s and Δx =3.38x10^{-5} m (at a shock stress of 70 GPa), and for Tungsten, at the same shock stress, the shock rise time is Δt = 9.69x10^{-9} s and Δx =4.79x10^{-5} m. Both of the shock widths are about 10 times smaller than the smallest cell size (0.5 mm) used in the laminate and are much smaller than the characteristic scale of oscillations observed in the shock wave.

3.3 Results of numerical calculations

The results of one-dimensional numerical calculations related to the formation and propagation of stress pulses generated by a long duration of incoming disturbances, with time ratios t_r between 25 and 1015, are investigated in this paper. At these higher time ratios, unlike in previous study [4], a stationary shock wave with an oscillating tail, where the frequency of the oscillations changes with the size of the cell, can be observed. We present results related to the formation and propagation of shock waves in 2+2 (2 mm Al plus 2 mm W layers), 1+1 (1 mm Al plus 1 mm W layers), and 0.5+0.5 (0.5 mm Al plus 0.5 mm W layers)

laminates impacted by 80- and 800-mm Al flyer plates. The numerical data presented here correspond to a point in the Al layers right at the interface with the W layers and (Fig. 2) all the distances are measured from the impacted end.

3.3.1 A 2+2 laminate impacted by an 80-mm Al flyer plate (t_r=25)

The stress evolution in a shock wave propagating in a 2+2 laminate impacted by an 80-mm Al plate is presented in Figs. 3(a) and 3(b). From these figures we can observe that at a depth of 12 mm, the duration of the leading front was already close to its stationary value (evident at a larger depths). We will later show how this corresponds to half of the duration of the stationary solitarylike wave presented in [4] and thus can be approximated by analytical equations presented in [4,11]; from these equations, the width of the leading part of the shock can be determined.

It is clear that the relatively fast decaying stress oscillations, due to plastic deformation, exist immediately behind the leading front (four first pulses). The amplitude of these oscillations initially increases with the propagation distance until they become quasistationary at some depth, as shown by the leading oscillations in the stress profiles in Fig. 3(b). This is typical for the dispersive behavior of materials with periodic mesostructures and weak dissipation, e.g., granular chains [26].

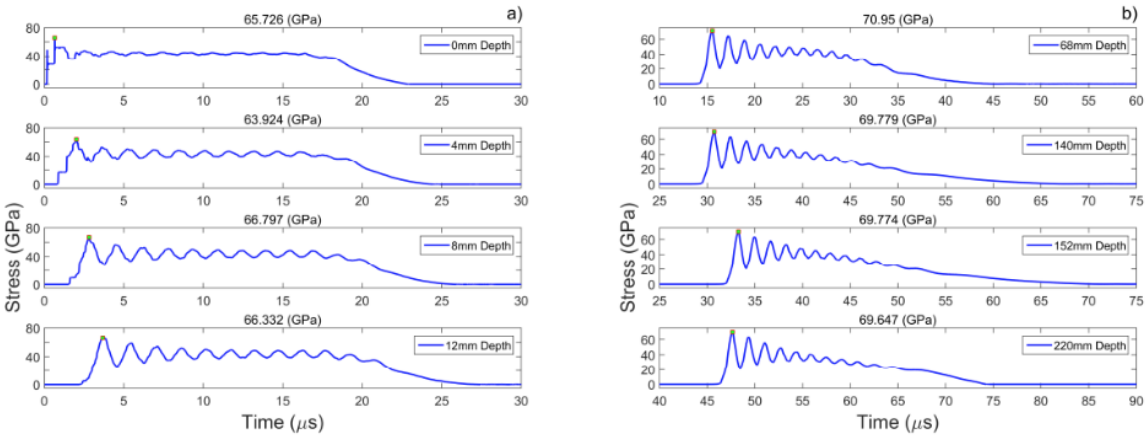

Figure 3-3: Stress pulse evolution in 2+2 laminate impacted by 80 mm Al flyer plate at 2800 m/s at different distances from impacted end (a) 0, 4, 8 and 12 mm (b) 68, 140, 152, 220 mm.

The mostly elastic oscillations behind the shock front attenuate very slowly. For this impact condition, they did not oscillate around an established mean value before the arrival of the release wave from the free surface of the impactor. It is interesting that the amplitude of elastic oscillations decreased with the arrival of the rarefaction wave due to their compressive nature. Thus the quasiequilibrium state, under this impact condition, was not reached and the use of the Hugoniot curve is not appropriate to describe the final states behind shock in the laminate.

It is interesting that the amplitude of the leading pulse has reached practically steady values (which we define as a deviation from the mean value that is below 0.5%) at a distance of about 120 mm [Fig. 4(a)]. The stationary leading front width and the amplitude of the leading pulse were reached despite the fact that the quasiequilibrium state behind shock (Fig. 1) was not established due to the arrival of the rarefaction wave. The leading front [0.1–0.9 wide (Fig. 1)] of the

oscillatory shock wave approaches a stationary value at a distance of 25 mm [Fig. 4(b)]. It seems that reaching the steady values of the leading amplitude is a slower process than establishing a leading front width. This is probably due to the different mechanisms determining their establishment, where the latter is mainly caused by the balance of the nonlinear and the dispersive terms and the former is due to a slower dissipation processes. We will illustrate that by using the KdV weakly dissipative approach it is possible to approximate the leading front width.

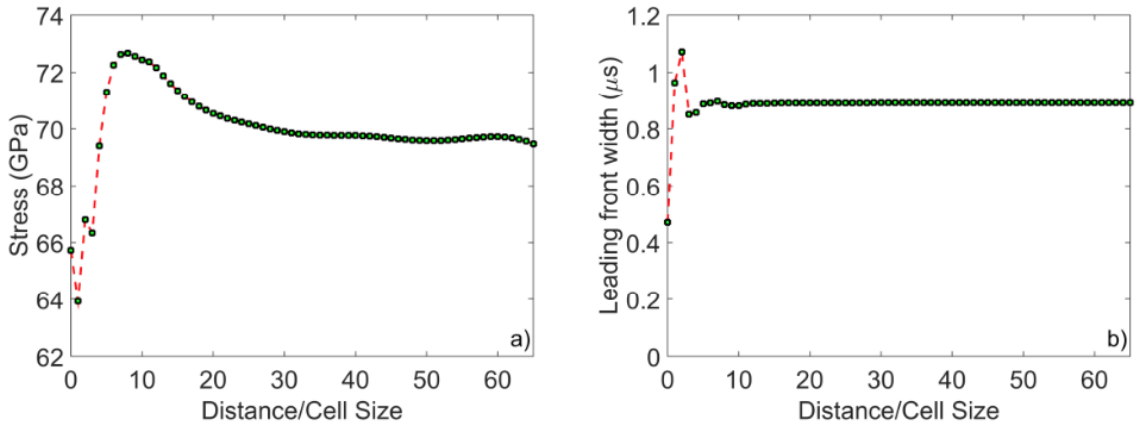

Figure 3-4: 2+2 laminate impacted by 80 mm Al flyer plate at 2800 m/s (a) Maximum stress on the leading front of the shock versus distance from impacted end; (b) Leading front width versus distance from impacted end.

The speed of the shock when the leading pulse reached its steady amplitude is equal to 4729 m/s. The nature of the shock wave and that of the solitary wave are qualitatively different. It is reflected in their different speeds of propagation; a solitarylike wave at the same stress level (~70 GPa) in the same Al-W laminate has a speed of 4474.5 m/s [4].

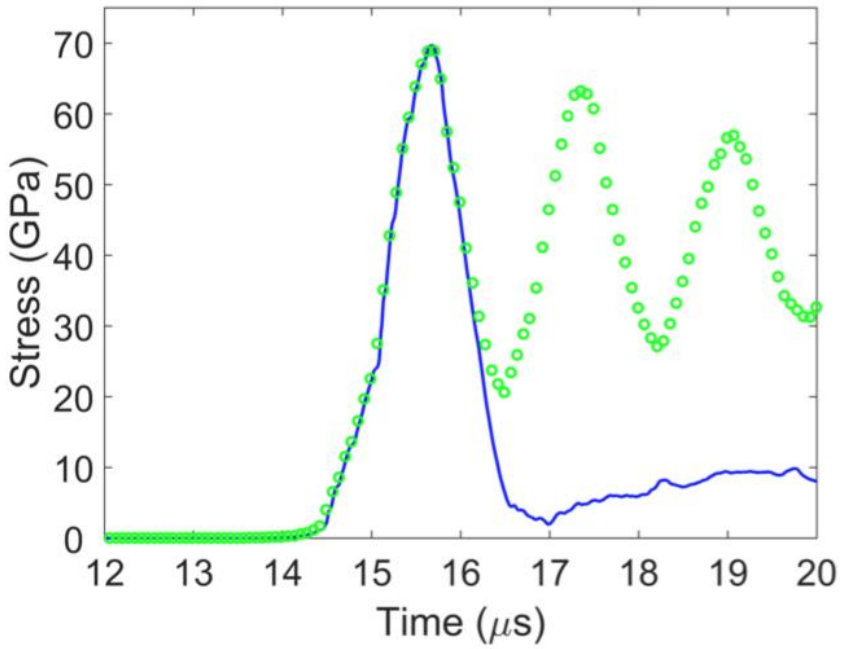

Figure 3-5: Comparison of a solitary-like wave (solid line) and leading part of a shock wave (empty dots) in the same 2+2 Al-W laminate. The solitary-like wave was created by the impact of an 8 mm Al flyer plate [7,8] while the shock wave was created by the impact of an 80-mm Al flyer plate.

Figure 5 presents a comparison of the solitary wave profile in a 2+2 laminate with the real dissipative properties [4] hit by the 8-mm Al plate with a velocity of 2800 m/s and the profile of the shock wave with a similar stress amplitude generated in the same laminate by the impact of the Al plate with a thickness of 80 mm. The comparison of the two stress profiles clearly shows that the shape and width of the leading stationary front of the shock are closely approximated by the solitarylike wave. Thus the strain rates in the leading part of the shock wave can be estimated based on the properties of the solitarylike waves presented in [4,11].

3.3.2 A 2+2 laminate impacted by an 800-mm Al flyer plate (t_r=254)

In the previous section we observed that the impact on a 2+2 laminate by an 80-mm Al plate did not form a stationary shock wave due to the relatively short duration of the incoming pulse in comparison with the characteristic time scale of the laminate. To increase the duration of the incoming pulse and explore its influence on the wave structure, an impact by an 800- mm Al plate with a velocity of 2800 m/s on a laminate with an identical mesostructure (2+2, as in the previous case) was in- vestigated. These impact conditions correspond to a time ratio of t_r = 254. The impact conditions were selected to remove the influence of the rarefaction wave in an attempt to reach a quasiequilibrium state behind the stationary shock front.

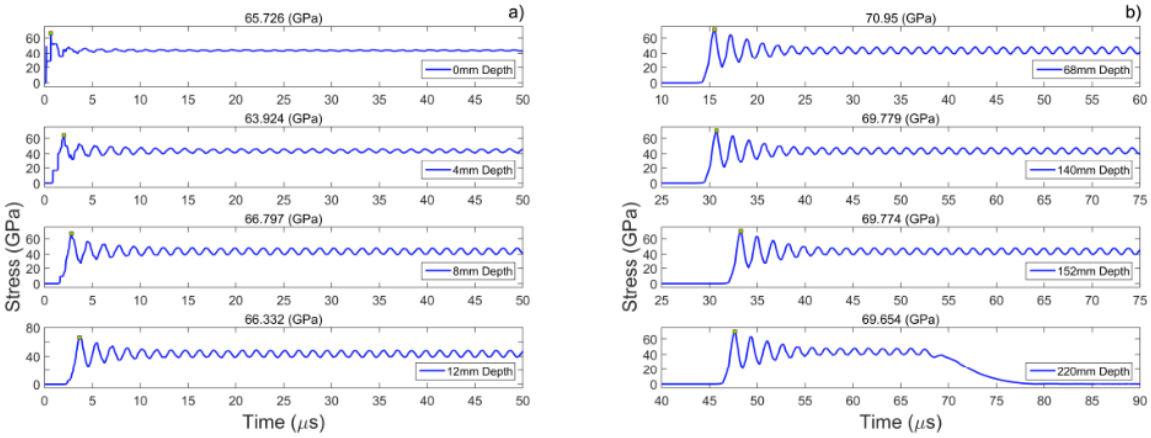

Figure 3-6: Stress pulse evolution in 2+2 laminate impacted by 800 mm Al flyer plate at 2800 m/s at different distances from impacted end (a) 0, 4, 8 and 12 mm (b) 68, 140, 152, 220 mm.

The evolution of the stress pulses is presented in Fig. 6. As in the case of the 2+2 laminate impacted by the 80-mm Al flyer plate, at a depth of 12 mm, the

leading front with similar amplitude was already close to its stationary value. Relatively fast decaying oscillations of the stress due to the plastic deformation exist right behind the leading front (the four first pulses), reflecting the dispersive behavior of the materials with periodic mesostructures and weak dissipation, e.g., granular chains [1,26].

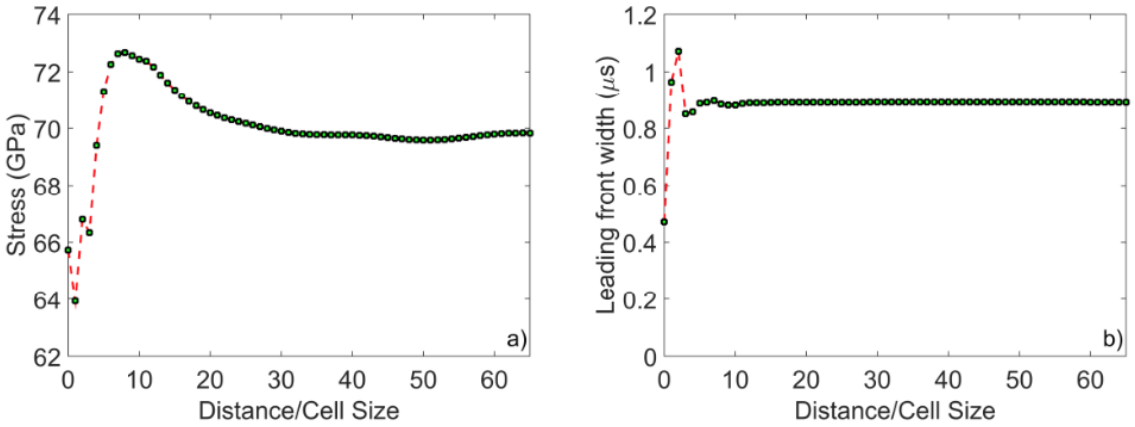

Figure 3-7: 2+2 laminate impacted by 800 mm Al flyer plate at 2800 m/s (a) Maximum stress in the leading peak vs. propagation distance (b) leading front width versus propagation distance.

Despite a different duration of the incoming pulse between this case and the previous one (impact by an 80-mm Al plate), the establishment of the leading front width of the shock wave and a steady amplitude of the leading peak happened at similar distances (compare Figs. 4 and 7). This demonstrates that at the investigated ranges of time ratios t_r = 25−254, a quasisteady shock front with an oscillatory tail can be expected, although reaching this quasisteady state takes a distance of about 120 mm (30 cells) or 25 mm (about 6 cells) for the leading amplitude and leading front width correspondingly. It should be emphasized that

at much shorter time ratios (t_r = 0.25) qualitatively different disturbances (solitarylike pulses) were observed [4].

In contrast to the previous case with an impact by an 80- mm Al plate, the quasiequilibrium state was indeed reached behind the leading part of the shock front with mostly elastic, very slowly attenuating oscillations about an established mean value. The elastic nature of these oscillations is demonstrated in Fig. 8, which shows the evolution of the shock front width with the traveling distance [Fig. 8(a)] and the stress history with its corresponding effective plastic strain at a depth of 100 mm from the impacted end [Fig. 8(b)]. The shock front width is determined by the distance from the leading edge of shock wave to the point where plastic strain is saturated.

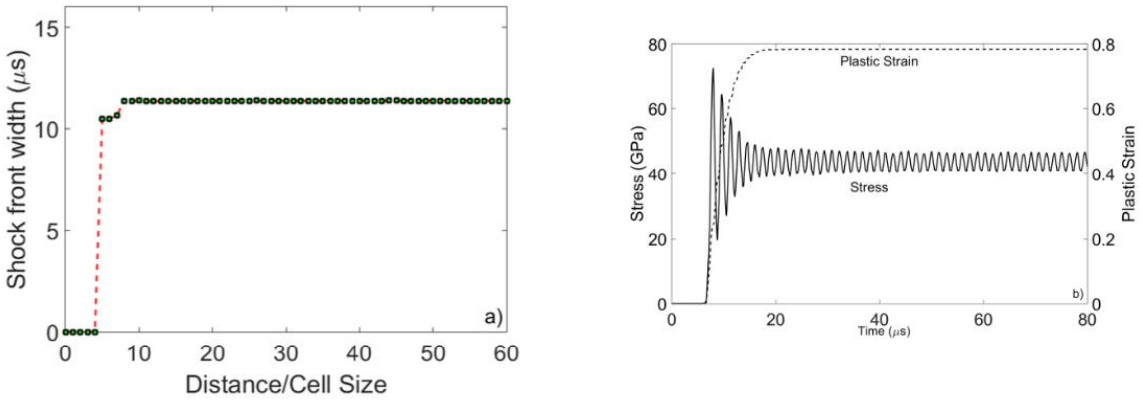

Figure 3-8: 2+2 Al laminate impacted by 800 mm Al flyer plate at 2800 m/s. (a) Shock front width vs. traveled distance (b) Superposition of stress profile and effective plastic strain, the inflection point on the plastic strain curve (right Y-axis) indicates the point where the oscillations become purely elastic.

This quasi-equilibrium state behind the shock (there are still elastic oscillations and different temperatures in the components) and the established

mean value of the stress can be approximated using the equation for the normal stress ($\sigma = \rho_0 D u$) based on the stationary conditions of the shock front and the assumption of a quasi-equilibrium state behind the shock front. Indeed, using the initial density of the laminate (ρ_0 =11043 kg/m^3), the particle velocity (u=827 m/s) and the shock speed (D=4279 m/s), a normal stress behind the shock is calculated to be 43.2 GPa, compared to 43.42 GPa from the numerical simulations.

The quasiequilibrium state was reached by a sequence of attenuating oscillations. These oscillations have a characteristic decay time that is determined by the dissipation mechanism. In our case, this is mostly plastic deformation. The structure of the stress pulse is qualitatively similar to the one expected for dispersive and weakly dissipative media described by the KdV equation with viscous dissipation. The characteristic scale in this approach is determined by the viscosity and dispersive coefficients [27,28].

The oscillating behavior continues into the quasiequilibrium state characterized only by elastic deformation. When the 2+2 laminate has reached a quasiequilibrium state, the compressed cell thickness is 3.3 mm: 1.5 mm Al plus 1.8 mm W. Sound speeds in the compressed components are 7942 m/s for Al and 4700 m/s for W [5] compared to their original 5328 and 4030 m/s, respectively. By using the corresponding sound speed of each layer under compression, we calculate the new long-wave sound speed in the compressed laminate to be 4910 m/s. The characteristic time of the sound propagation through the compressed cell is 6.7 × 10^{-7}s, about two times smaller than period of the elastic oscillations in the

quasiequilibrium state. These oscillations are probably the remnants of the oscillations inside the shock front where the plastic deformation provides the mechanism of their attenuation. The period of the elastic oscillations is scaled with the thickness of the laminate cell; for example, in the 2+2 laminate, the period is 15×10^{-7}s and in the 1+1 laminate presented later (Fig. 9), the period is 7.4×10^{-7}, about two times smaller at similar amplitudes of the leading wave and similar mean value of the stress in the quasiequilibrium state behind shock.

3.3.3 A 1+1 laminate impacted by an 80-mm Al flyer plate (t_r=51)

In Sec. 3.3.1 it was demonstrated that the impact by an 80-mm Al plate on the 2+2 laminate did not generate a stationary shocklike stress pulse. The dispersive properties of the laminates depend on the cell size and it is expected that this parameter can influence the rate of the establishment of the stationary shock wave. To explore the effects that cell refinement might have on the length scales required for the establishment of a stationary front, a refined 1+1 laminate, impacted by an 80-mm Al flyer plate (as in Sec. 3.3.1) was investigated.

Figures 9(a) and 9(b) show the results of the stress wave evolution inside this laminate. A few features should be emphasized. As in the previous cases, the stress waves have oscillatory profiles. However, in this case, the quasistationary stress wave (with elastic oscillations in the quasiequilibrium state) was formed, unlike the transient waves in the 2+2 laminate excited by the impact of the same 80-mm Al plate.

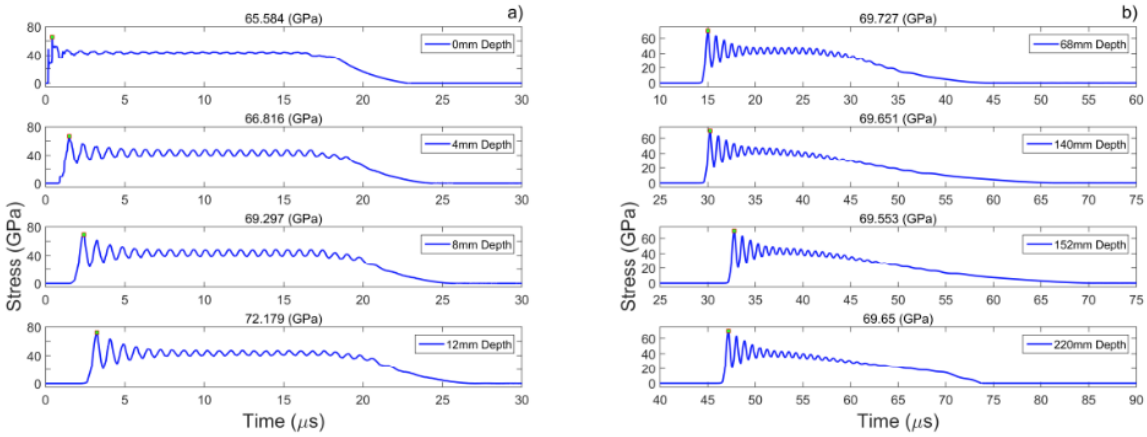

Figure 3-9: Stress pulse evolution in 1+1 laminate impacted by 80 mm Al flyer plate at 2800 m/s at different distances from impacted end (a) 0, 4, 8 and 12 mm (b) 68, 140, 152, 220 mm. Compare these profiles with the waves structure in 2+2 laminate excited by the same Al plate.

A difference in the frequency of oscillations behind the leading front of the wave can be observed by comparing the wave profiles presented in Figs. 3(a) and 3(b) and Figs. 9(a) and 9(b). It indicates that cell size is directly related to the period of these oscillations.

Another important feature of the stress waves in this refined 1+1 laminate is the faster establishment of the stationary leading front in comparison with the coarser 2+2 laminate [compare Figs. 3(a) and 9(a)]. In the former case, the stationary leading front and quasiequilibrium state behind, with oscillations fluctuating around a mean value of 43.6 GPa, were formed at relatively short distances from the impacted end (12 mm). At the same distance from the impacted end, in the 2+2 laminate, the stress wave did not have a stationary leading front

and the establishment of the quasiequilibrium state behind it was already influenced by the rarefaction wave.

The following details of the establishment of the stationary state of the leading front should be mentioned. By inspection of Figs. 9(a) and 9(b), one can qualitatively observe that a maximum steady stress level of approximately 69 GPa has been reached. Figure 10(a) presents a detailed picture of this process, demonstrating that this steady stress level is reached relatively close to the impacted end (at about 60 mm), compared to the corresponding distance of 120 mm in the case of the 2+2 laminate impacted by the 80- or 800-mm Al plates, where the same level of maximum stress in the leading front was observed.

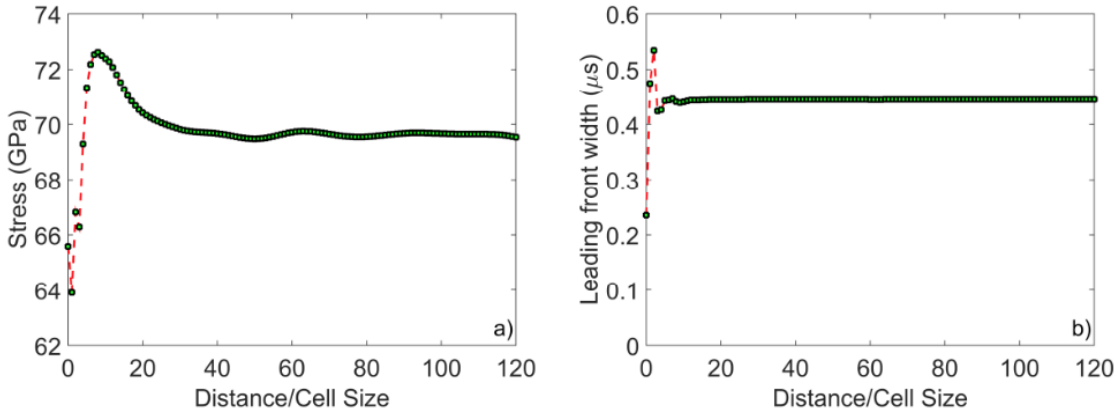

Figure 3-10: Establishment of the stationary amplitude in the leading front in the 1+1 laminate impacted by an 80-mm Al flyer plate at 2800 m/s: (a) maximum stress in the leading peak vs propagation distance and (b) leading front width versus propagation distance.

The leading front width is scaled with the cell size and it is equal to 0.445 μs (the 1+1 laminate [Fig. 10(b)]) compared to 0.89 μs in the 2+2 laminate. It is

important to analyze whether or not this 1+1 laminate has reached a quasiequilibrium state behind the shock front for these impact conditions (Fig. 11).

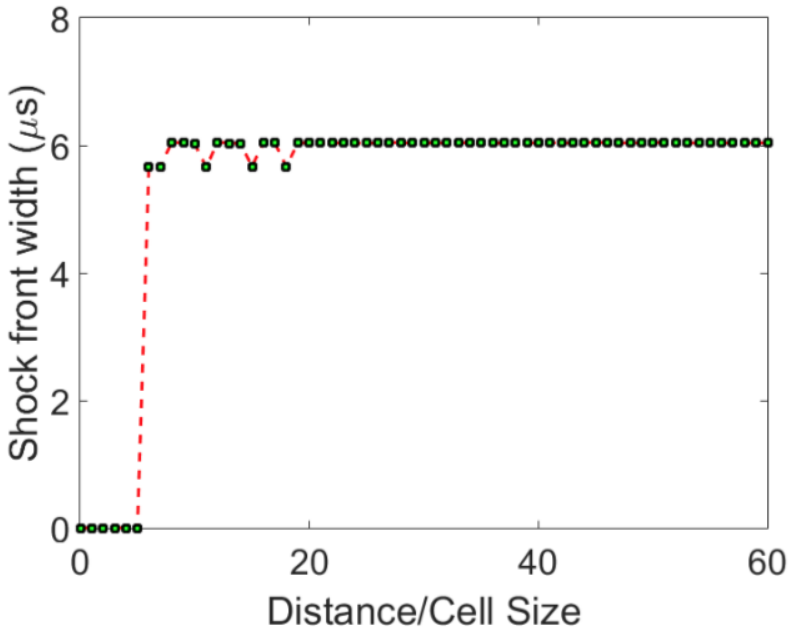

Figure 3-11: Establishment of the stationary shock front width with traveled distance in a 1+1 Al laminate impacted by an 80-mm Al flyer plate at 2800 m/s.

The formation of the quasiequilibrium state behind the shock front was not observed in the case of the 2+2 laminate, impacted by the 80-mm Al flyer plate (Fig. 3). Refinement of the cell size helped us reach a steady shock wave with a steady amplitude in the leading front; widths of the leading and shock wave fronts were established before the arrival of the rarefaction wave (Figs. 10 and 11).

3.3.4 A 1+1 laminate impacted by an 800-mm Al flyer plate (t_r=508)

We now explore if a longer duration incoming pulse than in the previous section results in the same parameters (amplitude of the leading shock front, leading front width, and shock front width) of the shock wave in the 1+1 laminate. To generate a longer incoming pulse in the 1+1 laminate, the numerical calculations were conducted with an 800-mm Al flyer plate having a velocity of 2800 m/s. Figures 12(a) and 12(b) present the results of these numerical simulations.

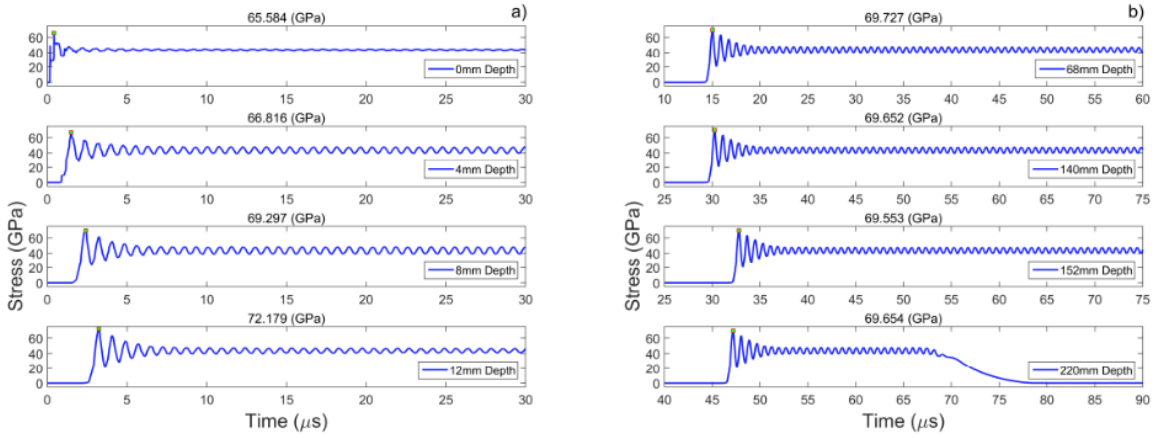

Figure 3-12: Stress pulse evolution in a 1+1 laminate impacted by an 800-mm Al flyer plate with a velocity of 2800 m/s at different distances from the impacted end: (a) 0, 4, 8, and 12 mm and (b) 68, 140, 152, and 220 mm.

Figures 12(a) and 12(b) show that the final quasiequilibrium state (where elastic oscillations are present) was reached before the arrival of the release wave. It is interesting that these oscillations very quickly decay after the arrival of the release wave. The oscillations are around the same mean value of the normal stress (43.6 GPa) as in the previous cases (the 1+1 laminate impacted by the Al

plate with an 80-mm thick plate [Fig. 9(a)] and 2+2 laminate impacted by an 800-mm Al plate [Fig. 6(b)]), where the quasiequilibrium state was reached behind the shock wave. The comparison of the final states behind the shock waves propagating in different laminates clearly demonstrates that the final quasiequilibrium state is not sensitive to the laminate's mesostructure.

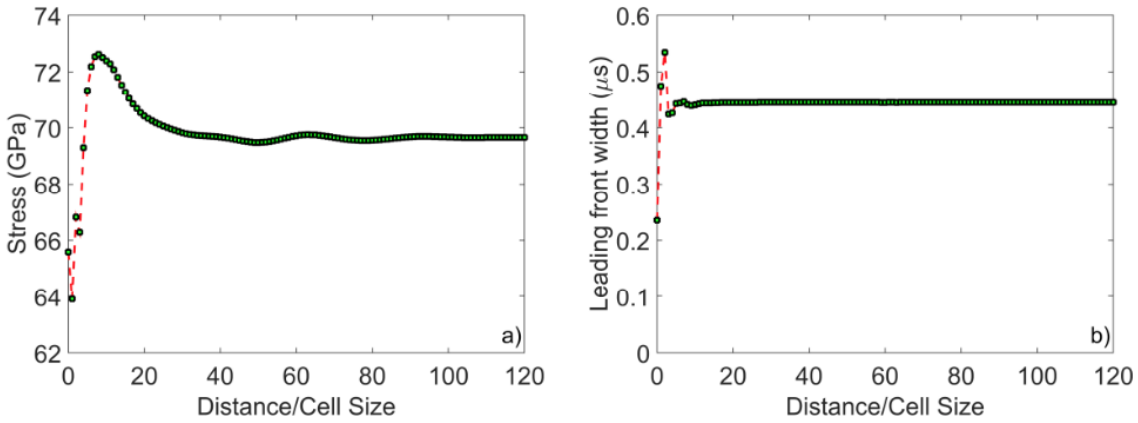

Figure 3-13: (a) Maximum stress in the leading peak and (b) leading front width versus propagation distance in a 1+1 laminate impacted by an 800-mm Al flyer plate at 2800 m/s.

It is interesting to find the distance where a steady shock front was established in this fine laminate. Figures 13(a) and 13(b) show the dependence on propagation distance of the stress at the leading peak and the leading front width of the shock. It is clear that they reached steady state values at differ- ent distances, which are the same as in the case of the 1+1 lam- inate impacted by the 80-mm Al plate [Figs. 10(a) and 10(b)].

A comparison of Figs. 10 and 13 demonstrates that a longer impactor (bigger time ratio t_r) did not affect the distance from the impacted end necessary for the establishment of the leading front width and the maximum stress level at

the leading peak. This observation suggests that there is a critical time ratio at which a stress wave in a laminate will be able to reach a steady-state regime. The normalized propagation distance to establish the steady peak stress was similar in the 2+2 and 1+1 laminates [about 30 cells in both cases; compare Figs. 7(a) and 13(a)]. The leading front width also scaled with the size of the cell, resulting in times equal to 0.45 μs in the 1+1 laminate vs 0.9 μs in the 2+2 laminate.

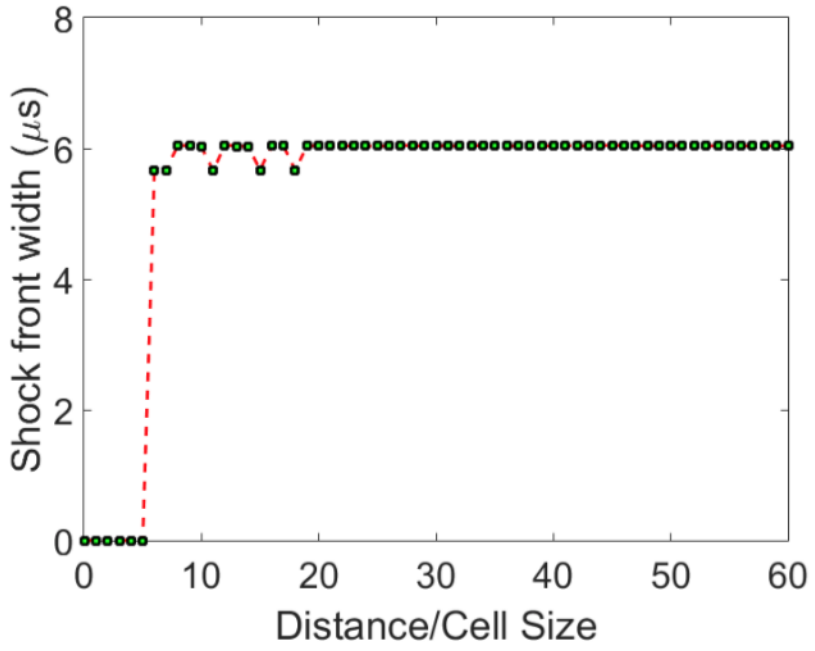

Figure 3-14: Shock front width vs traveled distance in the 1+1 Al laminate impacted by an 800-mm Al flyer plate at 2800 m/s.

Figure 14 illustrates the establishment of a steady shock front width in the 1+1 Al laminate impacted by an 800-mm Al flyer plate. The shock front width also scaled with the laminate cell size, decreasing from 11.4 μs in the 2+2 laminate to 6 μs in the 1+1 laminate [compare Fig. 14 to Fig. 8(a)]. The oscillations in the

quasiequilibrium state behind the steady shock front in the 1+1 laminate have a period half as large as the ones found in the 2+2 laminate (compare Figs. 6 and 12).

3.3.5 A 0.5+0.5 laminate impacted by an 80-mm Al flyer plate (t_r=102)

It was shown that the impact by the 80-mm Al flyer plate on a 1+1 laminate [Figs. 9(a) and 9(b)] resulted in a steady shock at a distance of about 30 cell sizes (Figs. 10 and 11), while at the same impact conditions, a steady shock wave was not formed in a 2+2 laminate at the same normalized distance from the impacted end [Figs. 3(a) and 3(b)]. We now explore if a steady shock is formed in a finer (0.5+0.5) laminate and how the main space-time scales change with the cell size. Figures 15(a) and 15(b) present the stress evolution in this 0.5+0.5 laminate impacted by an 80-mm Al flyer plate.

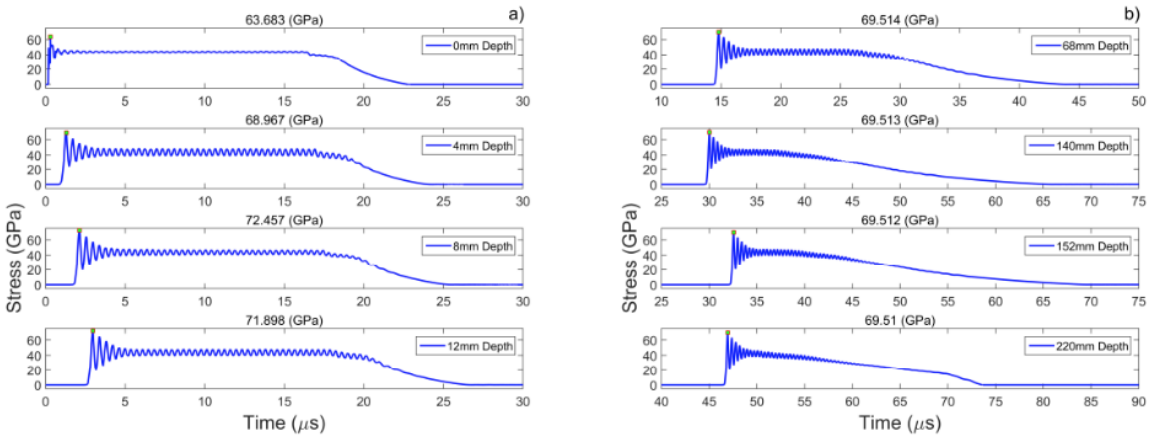

Figure 3-15: Stress pulse evolution in a 0.5+0.5 laminate impacted by an 80-mm Al flyer plate at 2800 m/s at different distances from the impacted end: (a) 0, 4, 8, and 12 mm and (b) 68, 140, 152, and 220 mm.

From the evolution of the stress wave profile, it is clear that a steady shockwave is established. It is important to compare the distance to establish the steady shock with results for the 1+1 laminates impacted by the same flyer plate. Figure 16(a) shows that the stress at the leading front reached a stationary value at around 30 cells, which is consistent with the previously analyzed 1+1 laminate [Fig. 10(a)]. The leading front width has also scaled with the refinement of the cell size as can be observed in Fig. 16(b).

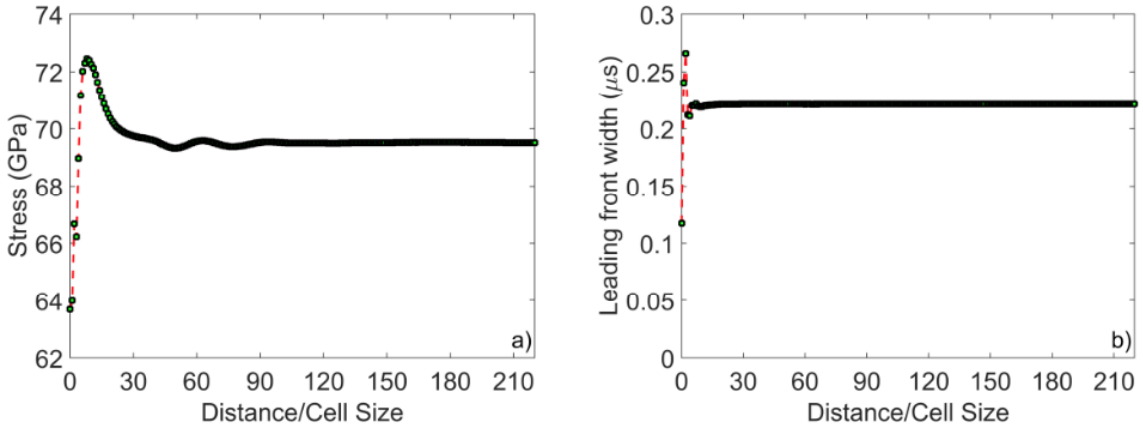

Figure 3-16: A 0.5+0.5 laminate impacted by an 80-mm Al flyer plate at 2800 m/s: (a) maximum stress in the leading peak vs propagation distance and (b) leading front width versus propagation distance.

The establishment of the shock front width is shown in Fig. 17. Contrary to other laminates, we observe bigger fluctuations before reaching a steady value close to 4 μs.

It is interesting that the normalized distance for the establishment of steady shock front width in the 0.5+0.5 laminate is similar to the case of the 1+1 laminate, but variations of this parameter inside the transient range are much larger in the former laminate (compare Figs. 11 and 17). Thus, we can conclude that impact by

the 80-mm flyer plate resulted in the establishment of a steady shock wave at the same amplitudes and similar normalized space scales in the 1+1 and 0.5+0.5 laminates. Similar impact conditions did not result in a steady shock wave in the 2+2 laminate.

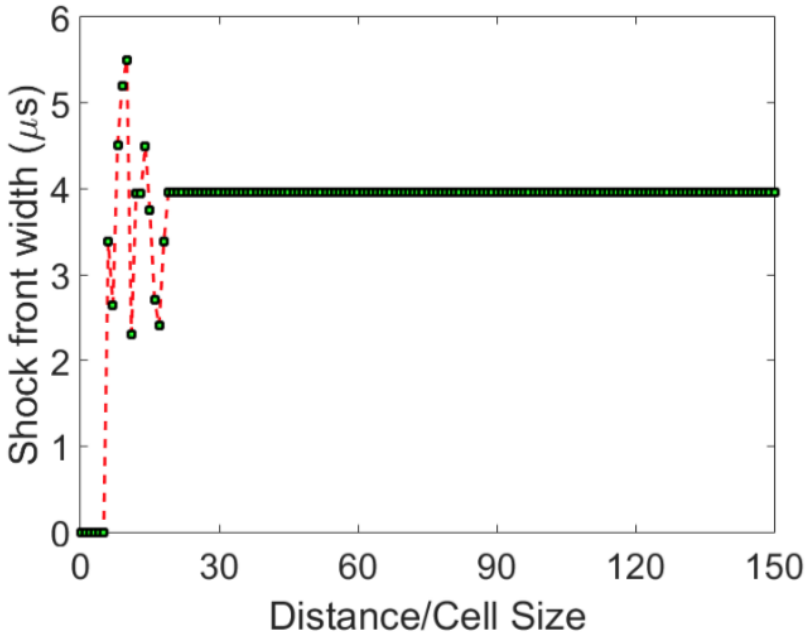

Figure 3-17: Shock front width vs traveled distance in a 0.5+0.5 Al laminate impacted by an 80-mm Al flyer plate at 2800 m/s.

3.3.6 A 0.5+0.5 laminate impacted by an 800-mm Al flyer plate (t_r=1016)

It is natural to expect that an increase in the duration of the incoming pulse in the 0.5+0.5 laminate, generated by impact of the 800-mm flyer plate, will also result in the establishment of a steady shock wave. Nevertheless, we want to check if the amplitude of this wave will be similar to the case of the impact by the 80-mm flyer plate at the same velocity and if characteristic length scales for the

shock wave will be the same. In other words, we would like to explore if a steady shock wave in the 0.5+0.5 laminate does not depend on the relatively long duration of incoming pulse. Figures 18(a) and 18(b) present the profiles of the stress waves in the 0.5+0.5 laminate impacted by an 800-mm Al flyer plate.

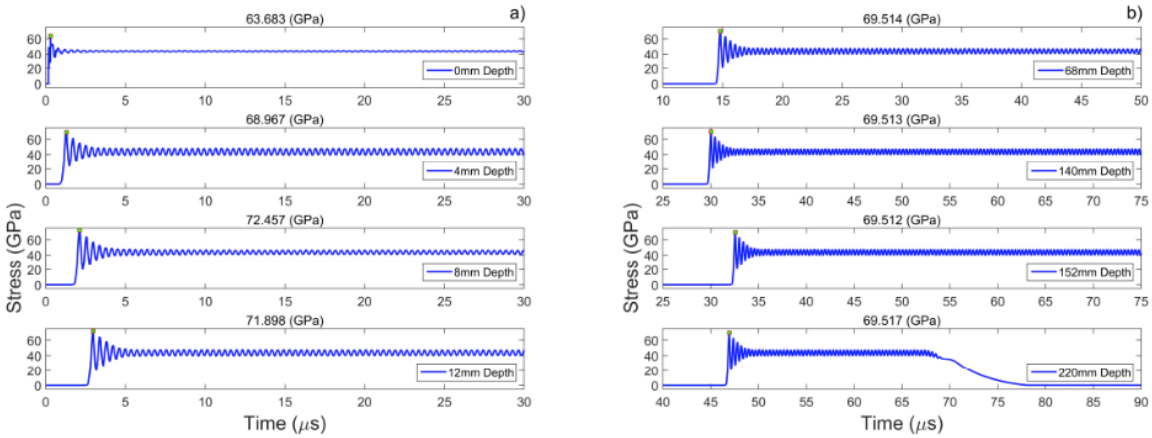

Figure 3-18: Evolution of stress wave profiles in a 0.5+0.5 laminate impacted by an 800-mm Al flyer plate at 2800 m/s at different distances from the impacted end: (a) 0, 4, 8, and 12 mm and (b) 68, 140, 152, and 220 mm.

It is clear from Fig. 18 that these impact conditions resulted in a steady shock wave. Figure 19 demonstrates that the establishment of the maximum stress and the leading front width of the shock wave happen at the same normalized distances from the impacted end as in the 0.5+0.5 laminate impacted by an 80 mm Al flyer plate. This demonstrates that the establishment of a steady shock front is mainly the result of the laminate mesostructure and the properties of the components and the duration of the relatively long incoming stress pulse has almost no effect.

Comparing Figs. 6(a) and 6(b), Figs. 12(a) and 12(b), and Figs. 18(a) and 18(b), we observe that the period of the elastic oscillations behind the shock front is equal to 0.37 μs for the 0.5+0.5 laminate, 0.75 μs for the 1+1 laminate, and 1.56 μs for the 2+2 laminate. It is clear that the period of these oscillations is directly related to the laminate cell size.

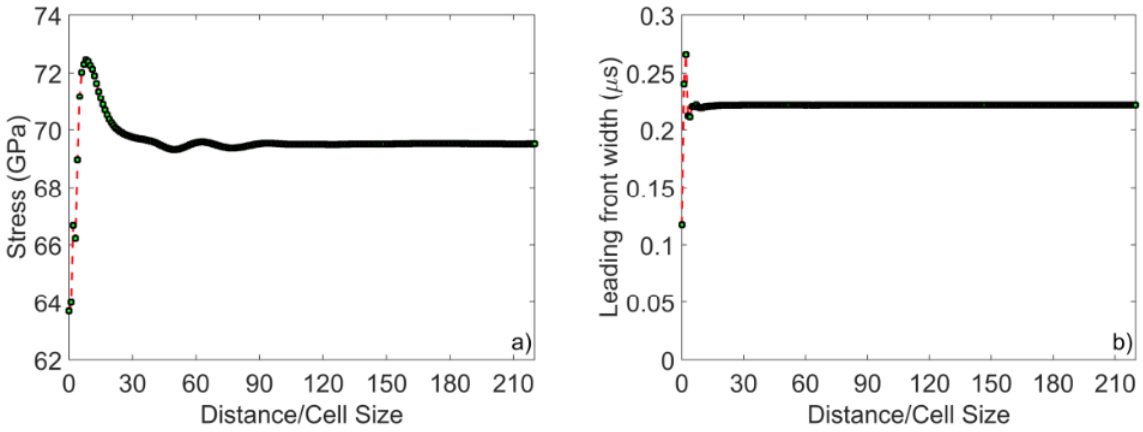

Figure 3-19: (a) Maximum stress in the leading peak vs propagation distance and (b) leading front width versus propagation distance in a 0.5+0.5 laminate impacted by an 800-mm Al flyer plate at 2800 m/s.

Finally, Fig. 20 shows that the steady shock front width was reached at the same normalized distance (about 30 cells) from the impacted end as the case for the same laminate impacted by the 80-mm Al flyer plate (Fig. 17). It is evident that the cell refinement in the laminate has a direct influence on the establishment of steady shock waves and their characteristic space scales.

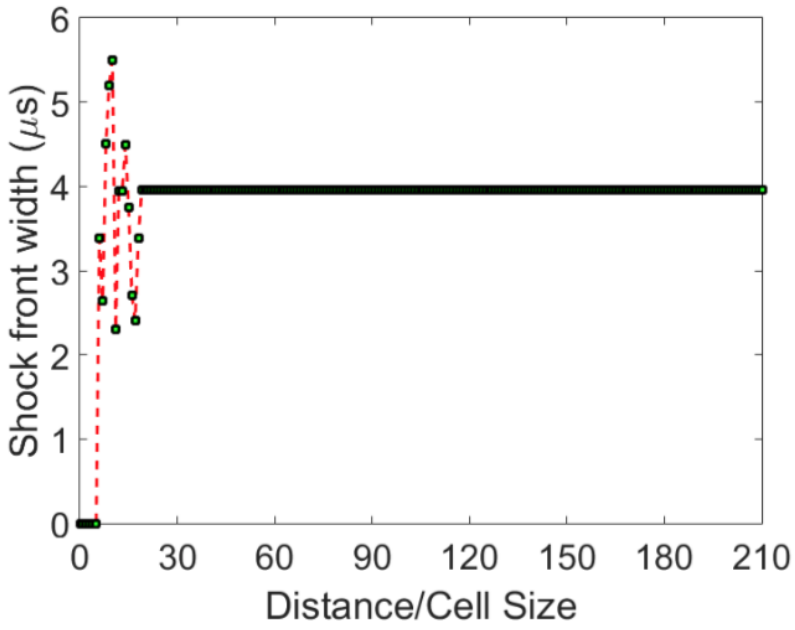

Figure 3-20: Shock front width vs traveled distance in a 0.5+0.5 laminate impacted by an 800-mm Al flyer plate at 2800 m/s.

The results of the presented numerical simulations demonstrated that quasistationary shock waves are formed when the duration of incoming compression pulse is long enough. These shock waves had a stationary oscillatory profiles connecting the initial and final quasiequilibrium states (it has elastic slow attenuating strain oscillations). We have found that the characteristic cell size of the laminate affects the leading front width and shock front width (both linearly proportional to the cell size of the laminate), while the quasistationary state behind the shock front appears to be independent of the cell size.

It is clear from Figs. 3, 6, 9, and 12 that two mechanisms are responsible for the formation of the stationary leading front: reflection of the leading wave at

interfaces, which widens the front (geometrical dispersion), and nonlinearity, which steepens it. The shock front width is influenced by the dissipation (in the case investigated mostly by the viscoplastic behavior of components) and it is an order of magnitude larger than the leading front width determined by the balance of the geometrical dispersion and nonlinear behavior of components.

The observed properties of the quasistationary shock waves are qualitatively similar to the shock waves in the weakly dissipative dispersive system described by the KdV equation [27,28]. In the following section we will attempt to identify a scaling of the main shock parameters using the dissipative KdV approach.

3.4 Scaling of shockwave parameters using the dissipative KdV equation

Nondissipative elastic periodic laminates support weakly nonlinear small-amplitude solitarylike waves (stegotons) [3]. It was also shown that short-duration high-amplitude stress pulses in the Al-W laminate have properties similar to KdV solitons despite the dissipation due to the plastic deformation. They attenuate while keeping their solitarylike identity deter- mined by the nondissipative KdV equation [4,11].

The stationary solution of the nondissipative KdV equation (1) presented below provides a reasonable approximation for the properties of these solitarylike waves:

$$\xi_t + C_o\xi_x + S\xi_{xxx} + \nu\xi\xi_x = 0, \tag{1}$$

$$S = \frac{d^2 C_0}{24}, \tag{2}$$

$$\nu = \frac{\alpha_{eq} C_0}{K_{eq}}, \tag{3}$$

$$C_o^2 = \frac{d^2}{\frac{d_a^2}{c_a^2} + \frac{d_b^2}{c_b^2} + \left(\frac{Z_a}{Z_b} + \frac{Z_b}{Z_a}\right)\left(\frac{d_a d_b}{c_a c_b}\right)}, \tag{4}$$

The cell size d and the long wave sound speed C_0 in the laminate determine the dispersive coefficient S, and the coefficients α_{eq} and K_eq are responsible for the nonlinear behavior of the laminate under compression. The parameters α_{eq} and K_{eq} for the high amplitude stress pulses were found using the Hugoniot curve of the components ($D_i = C_{0i} + s_i u_i$) allowing an approximation of the stress-strain relation of the laminate at high stresses (subscript i identifies Al or W component). This approach results in the following expression for the parameters α_{eq} and K_{eq}, details how to find them can be found in [4].

$$K_{eq} = \frac{\mathrm{K}_{Al}\mathrm{K}_W}{(1-\tau)\mathrm{K}_{Al} + \tau \mathrm{K}_W}, \tag{5}$$

$$\alpha_{eq} = \frac{\left(\tau \mathrm{K}_W^3 \alpha_{Al} + (1-\tau)\mathrm{K}_{Al}^3 \alpha_W\right)}{((1-\tau)\mathrm{K}_{Al} + \tau \mathrm{K}_W)^3}. \tag{6}$$

where τ is the volume fraction of Al. The coefficients K_i and α_i (i stands for Al or W) for each component are:

$$K_i = \frac{\mathrm{C}_{0\mathrm{i}}^2}{V_{0i}}, \tag{7}$$

$$\alpha_i = \frac{2 s_i \mathrm{C}_{0\mathrm{i}}^2}{V_{0i}}, \tag{8}$$

V_{0i} represents the specific volume of Al or W. As mentioned before, K and α capture the linear and nonlinear stress-strain behavior under compression, these

coefficients have been determined using material's shock Hugoniot, detailed explanation can be found in [4].

Eq. (1) has the following solitary solution propagating with speed v:

$$\xi = \xi_m \operatorname{sech}^2\left(\left(\frac{2\alpha_{eq}\xi_m}{d^2 K_{eq}}\right)^{\frac{1}{2}}(x - vt)\right). \quad (9)$$

Attenuating short-duration high-amplitude stress pulses at given strain amplitude ξ_m can be approximated by this equation [4,11].

The results of the numerical calculations presented above demonstrate that the incoming, long-duration, high-amplitude stress pulses generate stationary oscillatory shock waves (e.g., Figs. 6, 12, and 18). It is natural to explore if the parameters of these shock waves can be described by adding dissipation properties to the KdV equation (1).

The KdV equation with a viscous dissipative term (where μ is the viscosity coefficient) is

$$\xi_t + C_o\xi_x + S\xi_{xxx} + \nu\xi\xi_x - \mu\xi_{xx} = 0. \quad (10)$$

Equation 10 predicts not only the attenuating quasi stationary solitary-like waves, but it also supports a new type of disturbance - a stationary shock-like wave [27-28].

The shock-like strain wave supported by Eq. 10 has some specific properties that we will compare with the results of numerical calculations presented above.

First, the speed of propagation of this shock-like wave depends on its amplitude

$$V_{sh} = C_0 + \frac{\alpha_{eq} C_0}{2K_{eq}} \xi_f, \tag{11}$$

where ξ_f is the strain in the final state behind shock wave.

It is important to note that the speed of the shock-like stress wave is independent on the nature of dissipation, for example, in the Al-W laminate, it is mostly due to the plastic deformation, and not due to the viscosity. Depending on the dissipation level, the shock structure in nonlinear materials with a periodic mesostructure can be oscillatory (weakly dissipative) or monotonic (strongly dissipative) [27,28], but in both cases, the speed of the wave can be found using Eq. (11).

Second, the profile of shock-like solution for the weakly dissipative Eq. 10 has three characteristic space scales. The shock-like strain wave profile can be described by the following equation in the reference system moving with speed of the shock wave V_{SH} [27-28],

$$\xi = \xi_f + const\ exp\left(\frac{\mu}{2S} x\right) \cos\left(\sqrt{\frac{\nu \xi_f}{2S}} x\right), \tag{12}$$

the leading shock front is at x=0, ξ_f is the final strain behind shock and the shock wave propagates to the right, x<0).

This equation clearly demonstrates the existence of three spatial scales: one is related to the leading front width ($\pi\sqrt{S/2\nu\xi_f}$). This scale is of similar order of magnitude to the scale of the solitary-like wave supported by the non-dissipative

KdV (Eq. (1)). It was demonstrated that this scale is related to the shape of the high amplitude localized waves in Al-W laminates having properties similar to the KdV solitary waves [4].

The larger scale ($2\pi\sqrt{2S/v\xi_f}$) is related to the period of decaying oscillations behind the leading front, where the plastic work is still present.

The third characteristic scale ($2S/\mu$) is related to the spatial rate of decay of the oscillation amplitude, determined by the viscosity and the dispersion coefficient. It is important to note that first two scales depend linearly on the characteristic space scale of the mesostructure *d*. But the third characteristic scale, related to the oscillations amplitude decay, is proportional to d^2.

The change from oscillatory to monotonic shock-like profile, supported by weakly nonlinear KdV equation (Eq. 10), is determined by the critical value of viscosity μ_{cr} given by:

$$\mu_{cr} = \sqrt{2Sv\xi}. \tag{13}$$

The critical value of viscosity can be also identified for strongly nonlinear periodic system of particles interacting by Hertz law [1]. It is expected that a monotonous profile will be observed in the case of the strongly dissipative wave propagating in periodic structures with other mechanisms of dissipation, e.g., laminates with layers of foam [2] or metal plates separated by rubber O-rings [29].

Another important property of the stationary oscillating shock wave solution of weakly nonlinear dissipative KdV Eq. (10), is that the maximum amplitude of

strain in the leading pulse is equal to 1.5 of the final strain in the case when dissipation is very weak (and leading pulse is very close to solitary-like wave) [27].

It is interesting to compare the presented properties of the shock-like solution of Eq. (10) with the results of numerical calculations demonstrating oscillatory shock profiles (Figs. 6, 12, and 18).

Table 3-1: The speed of shock waves with different amplitude, strains in their leading maximum, a final mean strain in quasi-equilibrium states, their ratio obtained in numerical calculations, theoretical values of speed for shock-like stress wave and the difference between theoretical and numerical values of shock wave speeds. The data correspond to 2+2 laminate impacted by Al flyer plate of 800 mm thickness at different velocities

2+2 Laminate

Impactor Velocity (m/s)	Shock speed (m/s)	Max strain on leading front	Mean final strain in quasi-eq. state	Max/Final strains	Theoretical speed (m/s)	Diff. between theoretical & numerical shock speed
2800	4729	0.2762	0.2003	1.4	4605.4	2.7%
2400	4542	0.2354	0.174	1.4	4445	2.2%
2000	4363	0.1962	0.1473	1.3	4281.6	1.9%
1600	4180	0.1541	0.1199	1.3	4114.2	1.6%

The speed of the steady shock waves with different amplitude, strains in their leading maximum, the final mean strain in the quasiequilibrium state, and their ratio obtained in numerical calculations are presented in Table I. These data correspond to the 2+2 laminate impacted by an Al flyer plate of 800 mm thickness at different velocities. Table I also presents theoretical values of speed for the shocklike stress wave (corresponding to the final mean strains from a numerical

calculations) and the difference between theoretical [using Eq. (11)] and numerical values of shock wave speeds.

We can see that the theoretical values for the speed of the shocklike stress waves obtained using Eq. (11) are close to their values in numerical calculations (the maximum difference is 2.7%). The ratio of the strain amplitude in the leading maximum and the mean strain at the final state for different amplitudes of shock waves is in the interval 1.3–1.4, being only slightly lower than the predicted value for weakly dissipative and weakly nonlinear KdV equations. This demonstrates that plastic deformation in Al-W laminates results in a weakly dissipative behavior of stress pulses.

It is interesting to compare the shape of the localized stress pulses (excited by impact of an 8-mm Al flyer plate at 2800 m/s), leading fronts of the shocklike waves (excited by impact of 80 mm Al flyer plate and 800 mm Al flyer plate at 2800 m/s) in numerical calculations, and the solitary wave solution of Eq. (1) with similar amplitude. This comparison is presented in Fig. 21, which clearly shows that the solitary solution of Eq. (1) provides a correct estimation of the spatial characteristics of the localized stress pulse and the leading part of the shocks at their similar stress amplitudes.

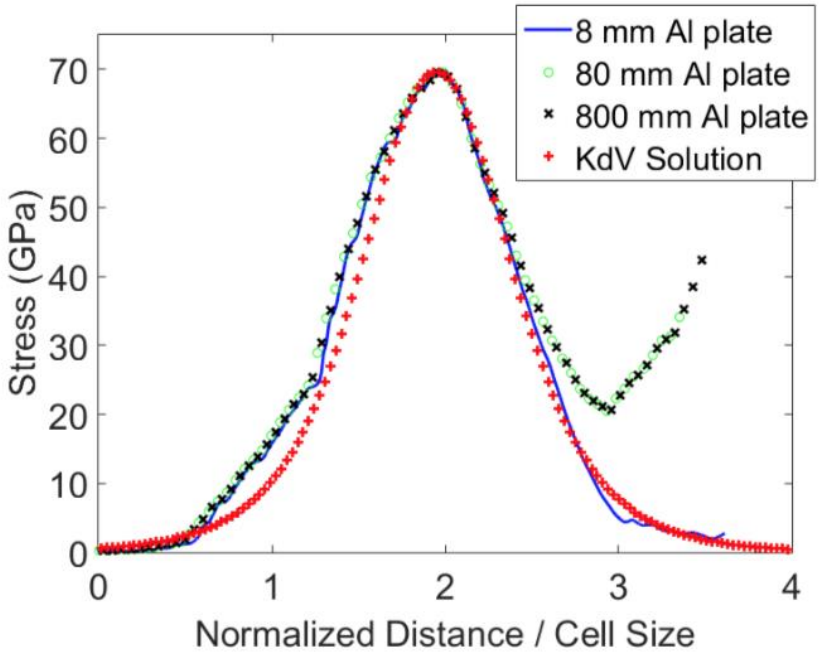

Figure 3-21: Comparison of KdV solitary solution to the shape of localized stress pulse (excited by impact of 8 mm Al flyer plate) and leading part of the shock wave with similar amplitude excited by impact of 80 mm Al flyer plate and 800 mm Al flyer plate. All cases correspond to 2+2 Al-W laminate and velocity of impactor 2800 m/s.

The period of decaying oscillations on the back of the leading front of shock wave in the KdV approach is related to the amplitude and dispersive properties of laminate scaling linearly with the cell size (Eqn. 12). These periods ($2\pi\sqrt{2S/\nu\xi_f}$) for similar values of ξ_f are equal to 0.0084 m, 0.0042 m and 0.0021 m for 2+2, 1+1 and 0.5+0.5 laminates respectively scaling with the sizes of unit cells.

From numerical simulations we obtain the following values for these periods of decaying oscillations: 0.0079 m, 0.0039 m and 0.0019 m corresponding to the 2+2, 1+1 and 0.5+0.5 laminates. It is clear that the periods of the oscillations in the numerical calculations (Fig. 6, Fig. 12 and Fig. 18) are close to the data from

theoretical approach based on the KdV equation being close to be proportional to the cell size. This again demonstrates that the high amplitude oscillatory shock waves in the Al-W laminates are weakly dissipative and scaled with the cell size as in the theoretical approach despite the qualitatively different mechanisms of dissipation.

The rate of the amplitude decay of the oscillations in the leading part of the shock wave in the weakly dissipative KdV approach is related to the viscosity and the dispersive coefficient (Eq. (12)) and it has a characteristic space scale ($2S/\mu$) that is proportional to the square of the cell size. The results of the amplitude decay of the oscillations for the different laminates are shown in Fig. 22. Fig. 22 compares the decay of the first four oscillations in different laminates (2+2, 1+1 and 0.5+0.5) under the same impact by 800 mm Al flyer plate with a velocity of 2800 m/s. It is clear that the space scale corresponding to their decay from the leading maximum to a point where only the elastic oscillations exist scales almost linearly with the cell seize (Fig. 22(a))).

This scaling is different than expected from the dissipative KdV approach with a constant viscosity. It indicates that the mechanism of plastic deformation in laminates can't be described by an effective viscosity coefficient that does not depend on the spatial scale d. This is expected because attenuation in the laminate is also due to wave reverberations and at given distance the number of these reverberations depends on the cell size d. Based on the numerical results,

we can conclude that if the dissipative mechanism is to be described by the effective viscosity this parameter should be proportional to d.

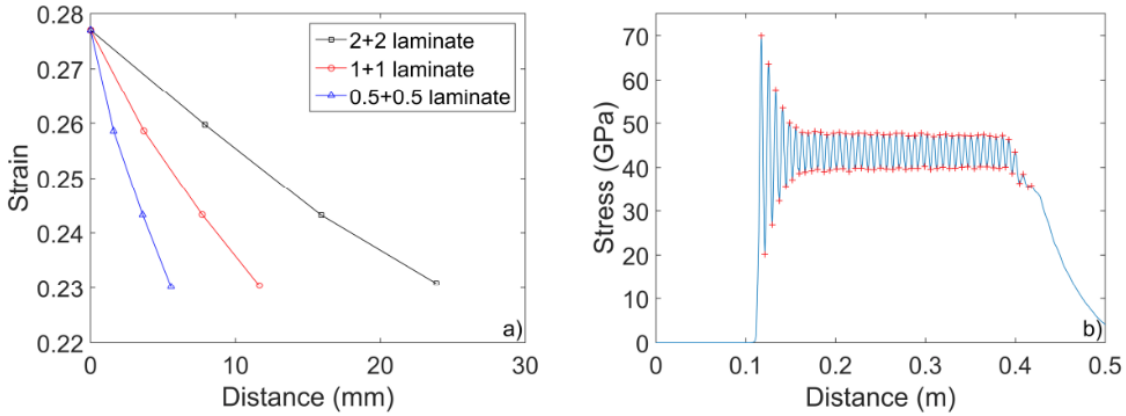

Figure 3-22: (a) Decay rate of the first part four oscillations on the leading shock on 2+2, 1+1 and 0.5+05 laminate. (b) Oscillating shock on 2+2 laminate that shows the decay of the oscillations until a quasi-equilibrium state has been reached.

The elastic oscillations in the region behind the shock front width demonstrate a very low rate of decay [Figs. 6, 12, and 18). Their periods are equal to 0.0074, 0.0035, and 0.0017 m for the 2+2, 1+1, and 0.5+0.5 laminates scaled by their cell sizes. It is clear that these very slowly decaying oscillations are

not described by the proposed KdV approach with a constant viscosity. It might be described with an effective viscosity vanishing or dramatically reduced at a certain level of stress below the yield stress.

The nonlinearity taken into account in the proposed KdV approach for the Al-W laminates is based only on the nonlinear relation between stresses and strains for each component determined by the interatomic forces. The nonlinear parameters of the components and the subsequent nonlinear parameter of the

laminate under compression were found from their shock Hugoniots as most representative for the material behavior under the investigated stress amplitudes. The detailed explanation of the procedure used can be found in [4]. Numerical calculations include all mechanisms of nonlinearity (the nonlinear relation between stresses and strains and convective and geometric nonlinearities), but our simplified KdV approach still is able to provide a reasonable description of the numerical results and scaling of the leading front thickness responsible for the maximum strain rates in shocked laminates.

3.5 Chapter conclusions

Long-duration impulse loading (compared to the characteristic time scale of the laminate) of the Al-W laminate resulted in the formation of oscillatory steady shock waves in Al-W laminates with different mesostructure. The width of the leading front and the maximum strain rates due to shock loading are determined by the dispersive and nonlinear parameters of the laminate and not by dissipation, as is the case in uniform solids. The characteristic spatial scale of the leading shock front can be satisfactory described by the Korteweg–de Vries approximation as well as its speed and the ratio of the maximum to final strain. The dissipation determines a shock front width where multiple loading-unloading cycles bring the laminate into a final quasiequilibrium state. The period of the fast decaying oscillations is well described by the KdV approach and scales linearly with the cell size of the laminate. The rate of decay of these oscillations in the numerical

calculations does not scale with the square of the cell size, as expected from the dissipative KdV approach with a constant viscosity due to the different mechanism of dissipation in high-amplitude compression pulses.

3.6 Chapter References

[1] E. B. Herbold and V. F. Nesterenko, Propagation of Rarefaction Pulses in Discrete Materials with Strain-Softening Behavior, Phys. Rev. Lett. **110**, 144101 (2013).

[2] V. F. Nesterenko, *Dynamics of Heterogeneous Materials* (Springer Science & Business Media, New York, 2001).

[3] D. H. Yong and R. J. LeVeque, Solitary waves in layered nonlinear media, SIAM J Appl. Math. **63**, 1539 (2003).

[4] P. Franco Navarro, D. J. Benson, and V. F. Nesterenko, Nature of short, high-amplitude compressive stress pulses in a periodic dissipative laminate, Phys. Rev. E **92**, 062917 (2015).

[5] R. Kinslow, *High-Velocity Impact Phenomena* (Elsevier, New York, 2012).

[6] S. P. Marsh, *LASL Shock Hugoniot Data* (University of California Press, Berkeley, 1980), Vol. 5.

[7] R. McQueen, S. Marsh, and J. Fritz, Hugoniot equa- tion of state of twelve rocks, J. Geophys. Res. **72**, 4999 (1967).

[8] C. Wei, B. Maddox, A. Stover, T. Weihs, V. Nesterenko, and M. Meyers, Reaction in Ni-Al laminates by laser- shock compression and spalling, Acta Mater. **59**, 5276 (2011).

[9] C. Wei, V. Nesterenko, T. Weihs, B. Remington, H.-S. Park, and M. Meyers, Response of Ni/Al laminates to laser-driven compression, Acta Mater. **60**, 3929 (2012)

[10] O. E. Petel and F. X. Jette, Comparison of methods for calculating the shock hugoniot of mixtures, Shock Waves **20**, 73 (2010).

[11] P. Franco Navarro, D. J. Benson, and V. F. Nesterenko, Proceedings of the 19th Biennial Conference on Shock Compression of Condensed Matter.

[12] V. Nesterenko, V. Fomin, and P. Cheskidov, Damping of strong shocks in laminar materials, J. Appl. Mech. Tech. Phys. **24**, 567 (1983).

[13] D. Benson and V. Nesterenko, Anomalous decay of shock impulses in laminated composites, J. Appl. Phys. **89**, 3622 (2001).

[14] R. Hofmann, D. J. Andrews, and D. Maxwell, Computed shock response of porous aluminum, J. Appl. Phys. **39**, 4555 (1968).

[15] J. W. Swegle and D. E. Grady. Shock viscosity and the prediction of shock wave rise times, J. Appl. Phys. **58**, 692 (1985).

[16] A. Molinari and G. Ravichandran, Fundamental structure of steady plastic shock waves in metals, J. Appl. Phys. **95**, 1718 (2004).

[17] A. Molinari and G. Ravichandran, Modeling plastic shocks in periodic laminates with gradient plasticity theories, J. Mech. Phys. Solids **54**, 2495 (2006).

[18] D. E. Grady, Structured shock waves and the fourth-power law, J. Appl. Phys. **107**, 013506 (2010).

[19] D. E. Grady, Unifying role of dissipative action in the dynamic failure of solids, J. Appl. Phys. **117**, 165905 (2015).

[20] S. Zhuang, G. Ravichandran, and D. E. Grady, An exper- imental investigation of shock wave propagation in periodically layered composites, J. Mech. Phys. Solids **51**, 245 (2003).

[21] J. O. Hallquist, *LS-DYNA Theory Manual* (Livermore Soft- ware Technology Corporation, Livermore, 2006); http:// www.lstc.com/pdf/ls-dyna_theory_manual_2006.pdf

[22] D. Steinberg, S. Cochran, and M. Guinan, A constitutive model for metals applicable at high-strain rate, J. Appl. Phys. **51**, 1498 (1980).

[23] D. Steinberg, *Equation of State and Strength Properties of Selected Materials* (Lawrence Livermore National Laboratory, Livermore, 1996).

[24] L. C. Chhabildas and J. R. Asay, Rise-time measurements of shock transitions in aluminum, copper and steel, J. Appl. Phys. **50**, 2749 (1979).

[25] J. C. Crowhurst, M. R. Armstrong, K. B. Knight, J. M. Zaug, and E. M. Behymer, Invariance of the Dissipative Action at Ultrahigh Strain Rates Above the Strong Shock Threshold, Phys. Rev. Lett. **107**, 144302 (2011).

[26] S. Y. Wang and V. F. Nesterenko, Attenuation of short strongly nonlinear stress pulses in dissipative granular chains, Phys. Rev. E **91**, 062211 (2015).

[27] V. Karpman, *Nonlinear Waves in Dispersive Media* (Pergamon, New York, 1975).

[28] R. Z. Sagdeev, Fine structure of a shock-wave front propagated across a magnetic field in a rarefied plasma, Sov. Phys. Tech. Phys. **6**, 867 (1962).

[29] X. Yichao and V. F. Nesterenko, Proceedings of the 19th Biennial Conference on Shock Compression of Condensed Matter (Ref. [11]).

Chapter 3, in full, is a reprint of the material as it appears in Physical Review E, Franco Navarro, P., Benson, D.J. and Nesterenko, V.F., American Physical Society 2016. The dissertation author was the primary investigator and author of this paper.

Chapter 4 : Instability of cavity collapse in highly heterogeneous mixture granular Al-W

4.1 Introduction

The purpose of this chapter is to explore the possible self organization phenomena (e.g., shear localization and patterning observed in many materials in similar conditions of deformation) and stability of cavity collapse in highly heterogeneous samples made of Al-W powders using Thick-Walled Cylinder (TWC) experiments. Cavity collapse is important in many physical processes, e.g. generation of hot spots in energetic materials [1], cavitation, microstructure of meteorites who are in fact densified matter [2]. Cavity collapse is also used for strain controlled, high strain, high strain rate deformation in the TWC method [3-10]. The former has allowed the investigation of materials instability in high strain rate plastic flow.

In the case when materials are under shock or dynamic compression, it is observed that microcavities or pores are collapsed under relatively high pressures. A model proposed in [11, 12], included the dependence of the collapse on the temperature. During the process of shock consolidation of powders [3, 13-18], the creation of localized hotspots can occur due to the creation of microjets caused by cavities collapse, which is directly influenced by the initial shape of the grains [18]. A relative amplitude of the shock and the particle strength determines specific

regimes of deformation of granular materials: (a) a quasistatic regime of pore collapse where no jetting is observed and grains are deformed as in a quasistatic process despite shock loading and (b) a dynamic regime where microjetting is generated during the process of pore collapse. The difference between these two regimes is important. The dynamic regime facilitates a bonding process between particles and chemical reactions during the shock loading of granular materials. In [19], it was reported that jetting formed during shock-induced loading of nanometer-scale voids, was the reason for detonation initiation. It was recognized that void filling in granular materials by a liquid may serve as an effective mechanism of energy dissipation [20].

The dynamic pore collapse for all materials is unstable at some strains due to strain softening mechanisms. These mechanisms are very different depending on the materials micro/meso structure. In small grain size copper, Ti, 4340 steel and SS304L (Fig. 1(a)), [7,21-23], the main mechanism is shear instability resulting in shear bands with their subsequent self organization creating a regular pattern of localized shear bands. In monocrystals (Fig. 1(b)) [24, 25] and large grain size materials [5], this pattern of localized shear bands is suppressed by instability caused by mechanisms of deformation related to crystal plasticity anisotropy.

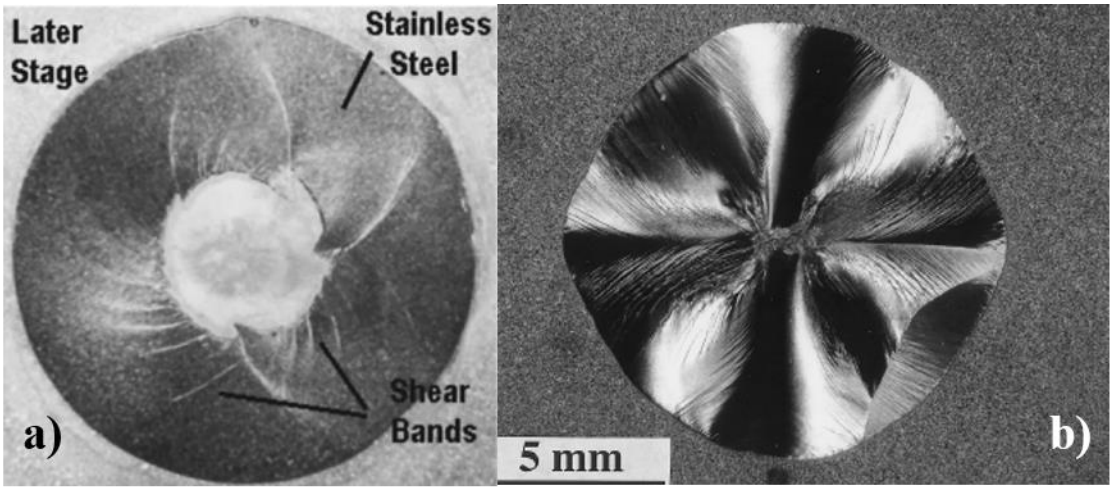

Figure 4-1: (a) Failure of SS304L through shear band formation and interaction as presented in [22] and (b) Optical micrograph of collapsed Cu showing suppression of shear band formation through deformation along crystal orientation as presented in [24].

In granular materials, such as SiC and Al_2O_3 (Fig. 2(a)) [26] the regular pattern of localized shear bands is due to a microcracking softening mechanism. In the case of laminates, the shear localization due to thermal softening is not a dominating mechanism. Instead, the cooperative buckling is the preferential mechanism of instability flow in the collapse of laminate cavities [27] (Fig. 2(b)).

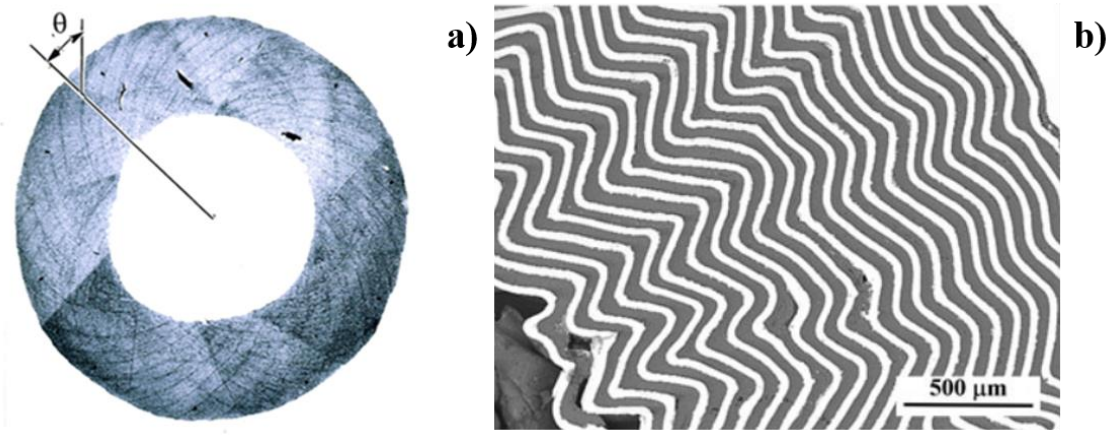

Figure 4-2: (a) Failure through microcracking in TWC collapsed SiC specimen (b) Mechanism of cooperative buckling in Al-W laminate cylinder. Pedro, replace (a) with pattern of shear bands.

The goal of this chapter to explore and help identify, using numerical modeling and experiments, mechanisms of instability that dominate in the process of pore collapse in highly heterogeneous mixture of ductile, low density (2.7 g/cc) and strength (7-11 MPa) Al and high strength (750 MPa), high density (19.3 g/cc) W particles with different porosity. It is shown that the grain size of W has a significant influence on the mechanisms of instabilities during cavity collapse. The weak deformation “paths” along clusters of Al grains, which are oriented approximately under 45 degrees to radius, appear to be nucleation sights for localized shear deformation.

4.2 Experiments

Al-W granular/porous composite tubes were prepared from elemental Al powder (Alfa Aesar, -325 mesh), coarse W powder (Alfa Aesar, -325 mesh) and

fine W powder (Alfa Aesar, <1 μm) . The volume ratio of Al to W, in Al-W samples was approximately 70% to 30%, corresponding to a theoretical density of (7.665 g/cm3) for a solid sample close to density of steel as required for specific applications. Mixtures of the Al W components were first ball-milled to prevent the agglomeration of particles using a SPEX 800 for 10 minutes with a 1:5 mass ratio of 4 ceramic balls to powder. The mixture was then placed in a cylindrical stainless-steel assembly encapsulated in a rubber jacket (Figure 3).

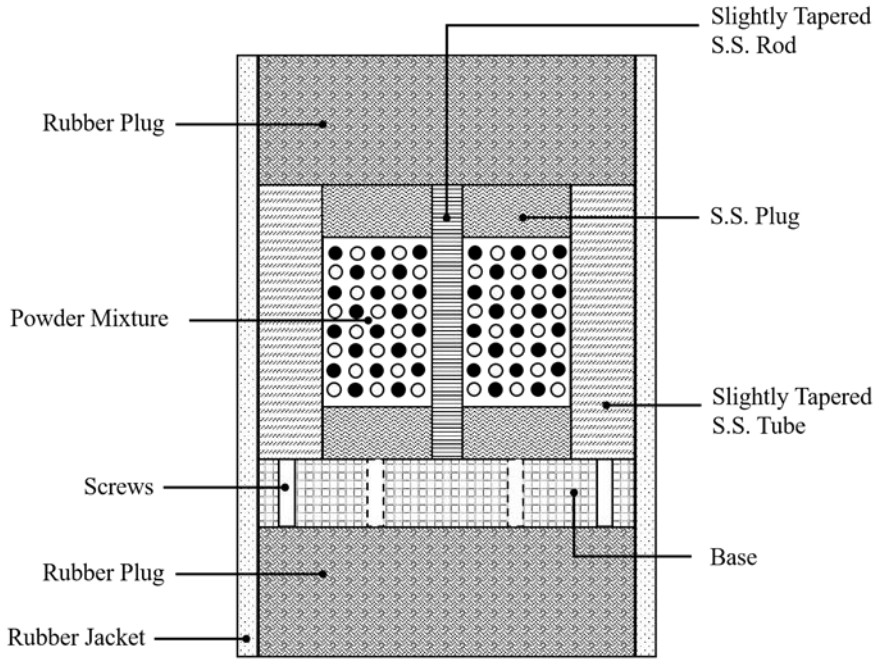

Figure 4-3: Schematic configuration used to create high accuracy Al-W powder samples using Cold Isostatic Pressing with oil as pressurizing media. The base was attached to the SS tube by six screws. Top and bottom rubber plugs were secured by clamps to prevent oil penetration inside assembly during CIPing.

Densification of the sample was accomplished by the axial movement of the top SS plug axially pushed by deformed rubber plug inside during pressurization

in the CIPing cycle. After CIPing and disassembling of the base plate from SS tube the sample was pushed away from the assembly.

All samples were CIPed at 345 MPa under room temperature for 10 min. The high accuracy ring shaped sample of densified powders is shown in Fig. 4.

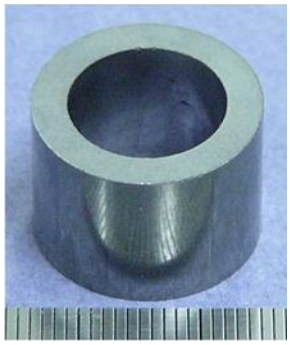

Figure 4-4: Sample after CIPing. The scale on the bottom is in millimeters.

The initial properties of rings after CIPing are presented in Table 1.

Table 4-1: Experimental results of sample properties after processing.

Sample	Length (mm)	O.D. (mm)	I.D. (mm)	Weight (g)	Density (g/cm^3)	Porosity (%)
Al-cW	11.62	19.18	12.95	12.06	6.60	13.9
Al-fW	11.84	19.29	13.02	12.00	6.36	17.03

The samples were enclosed in a copper assembly for the explosively loaded TWC test as show in Fig. 5.

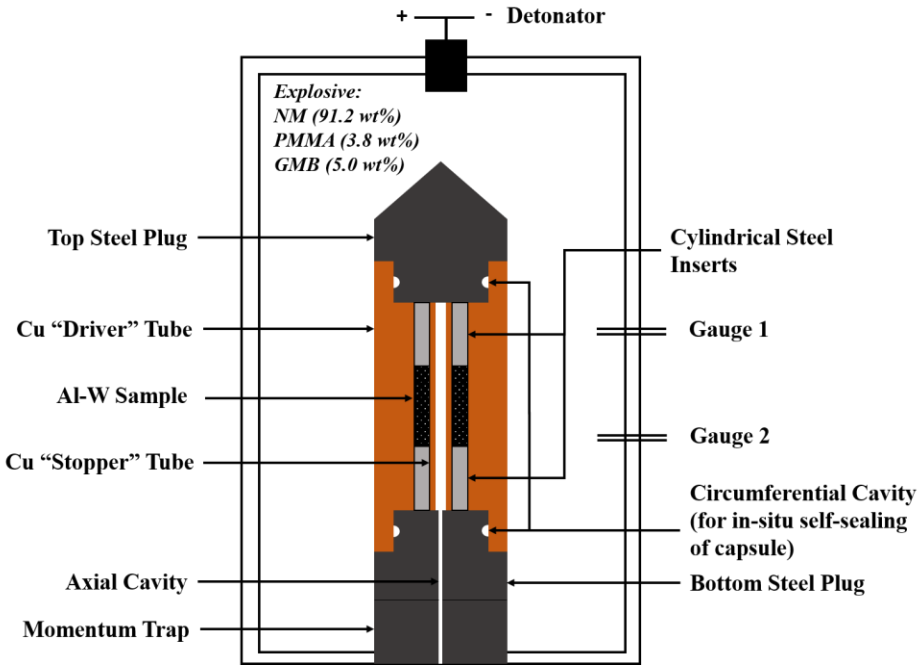

Figure 4-5: Thick Walled Cylinder test assembly

The copper stopper tube had an inner diameter of 11 mm and an outer diameter of 12 mm. The thick walled copper driver tube had an inner diameter of about 19.2-3 mm and an outer diameter of 30 mm. In both cases the copper was selected due to its resistance to shear localization. The toroidal cavities on the bottom and top plugs served for self-sealing of the samples during the test [28] and axial cavity was necessary to avoid trapping of the central jetting.

The explosive driver for the TWC test was a gelled nitromethane (96% nitromethane, 4% PMMA) diluted 5% by mass with glass micro balloons that allowed for the fine tuning of the dynamic loading (explosive density=0.82 g/cc, detonation velocity = 4.8 mm/μs). The diameter of the explosive charge was equal

to 58 mm and thickness of PVC container was 7.4 mm. Further details about the experimental set-up can be found in [9].

After the test, samples were cut using electrical discharge machining to prevent intermetallic reaction between Al and W and the sections are shown in Fig. 6. No shear localization was observed in the tested samples and they are mostly uniformly collapsed unlike in the samples of solid steel and sic granular material (Figs. 1 and 2).

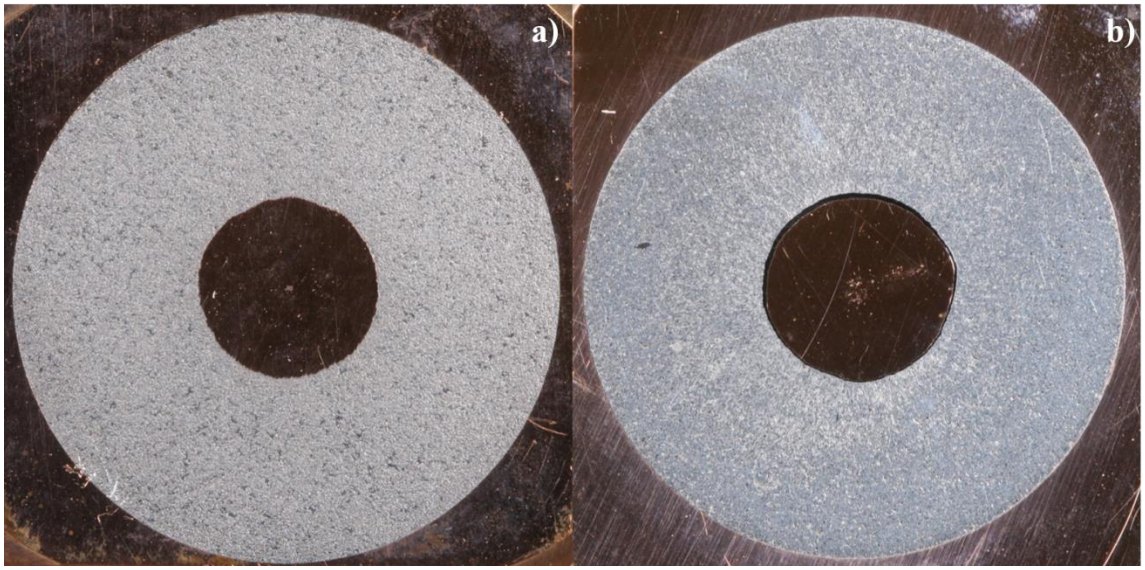

Figure 4-6: (a) Al-coarse W sample and (b) Al-fine W sample. The central copper rod was created by the collapsed copper stopper tube. The collapse in both samples is quite stable and the cylindrical symmetry of the sample has been preserved in both inner and outer surface (compare with Figs. 1 and 2.

Scanning Electron Microscope (SEM) was used to investigate the microstructure before and after tests in the samples with coarse (40 micron) and fine (1 micron) W particles.

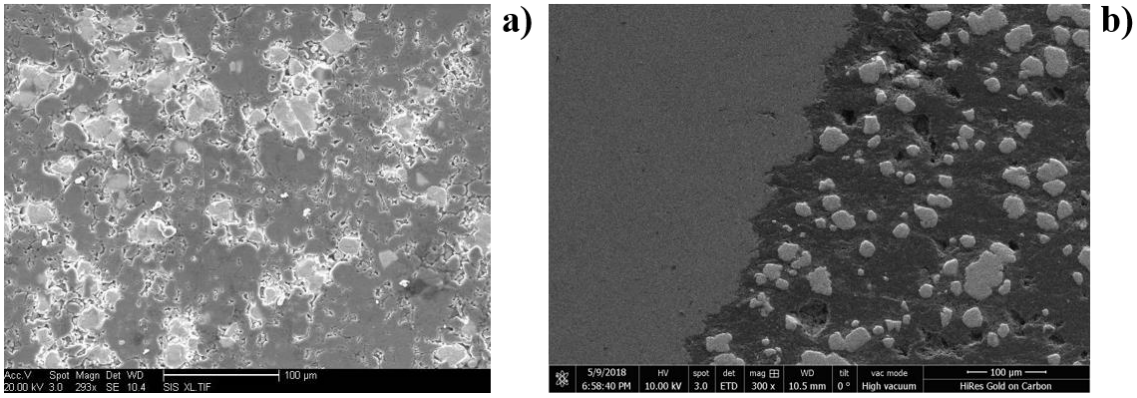

Figure 4-7: Al-coarse W sample before (a) and after (b) TWC tests, on right is the interface between the sample and copper driver tube.

From Fig. 4.8 we can see that initially equiaxed Al particles become elongated flowing between mostly underformed W particles and accumulating most of the plastic strain.

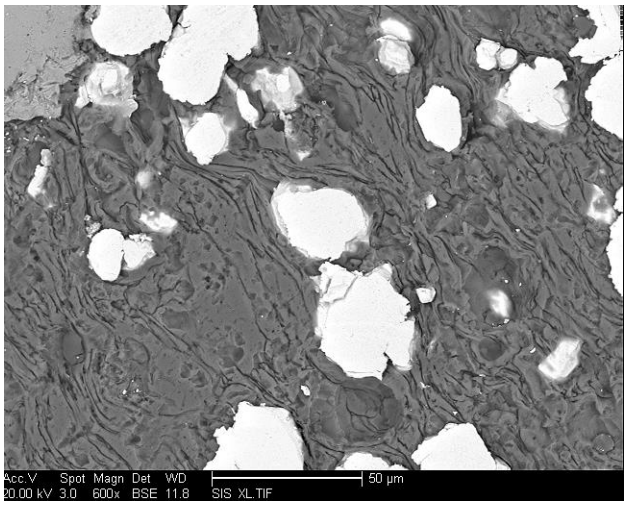

Figure 4-8: Plastic flow of Al particles between Al grains

The fine W particles (Fig. 9(a) and 9(b)) become more agglomerated during the deformation, in comparison with the coarser W particles (Fig. 8) and their clusters (white in the picture) seem to be radially oriented.

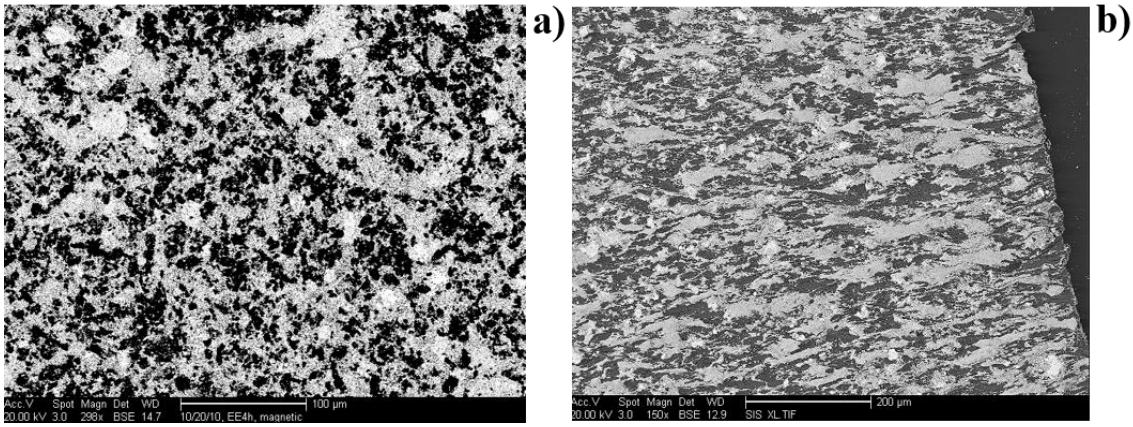

Figure 4-9: Al-fine W sample before (a) and after (b) TWC test.

The coarse, high strength W particles were not plastically deformed in comparison with low strength Al particles during the collapse process. Thus the overall plastic deformation of the sample was accommodated by plastic flow of Al particles between W particles (Fig. 8). This phenomenon is comparable to the one observed in experiments of granular Al-W expanding rings, where Al flows in-between W fibers [28].

In case of fine W particles the flow only of Al particles was not sufficient to accommodate a global plastic deformation of the sample. Radial alignment of fine W particles (Fig.9), requiring their displacements and reordering during deformation, was probably necessary to accommodate the global plastic deformation of the sample.

A closer look at the interface between the sample with fine W particles and Cu stopper tube demonstrates relatively smooth boundary (Fig. 10,a,b). Fine W particles probably flow with Al particles during cavity collapse (despite the very large difference in their strength) resulting in relatively smooth interface of the sample with copper stopper tube.

Fig. 10(c,d) corresponding to the experiments with coarse W particles reveals a small scale irregularities/instabilities at the sample interface with copper stopper tube, though they did not resulted in a regular pattern. The size of these instabilities is comparable to the size of W particles. It seems that flow of Al particles between coarse W particles has caused a jetting phenomenon resulting in kinks at the interface with a Cu stopper tube. This phenomenon was also observed in the numerical simulations.

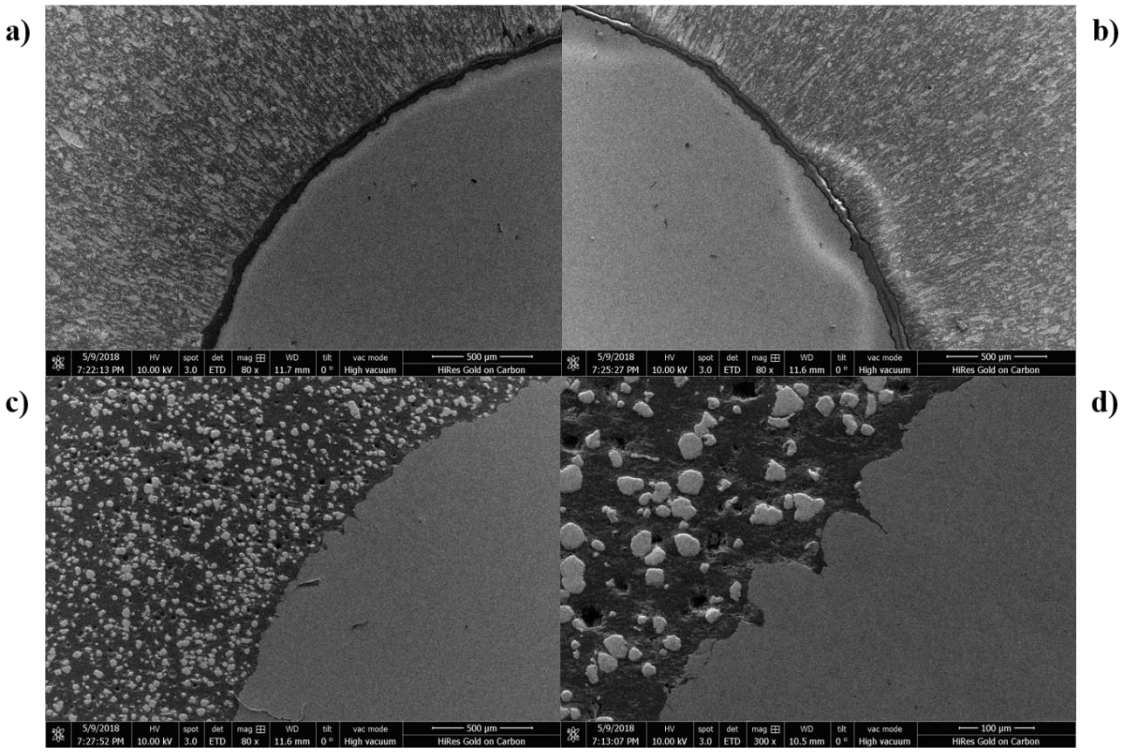

Figure 4-10: Closer look of the Al-W composite microstructure after TWC tests: (a)-(b) Al-fine W, (b) Al-coarse W. During the collapse, soft Al particles flow around the coarse,hard W particles and they are heavily deformed between W particles. This is like what it is observed in expanding geometry. On the other hand, fine W particles flow with Al particles during collapse.

4.3 Numerical Simulations

Numerical simulations were executed LS-DYNA, a general-purpose finite element code. To represent the grains used in experiments, an appropriate mesh was created utilizing Voronoi partitions as presented in [30]. The tessellations of the circular area are then adapted for analysis in LS-DYNA and an example is shown in Fig. 11.

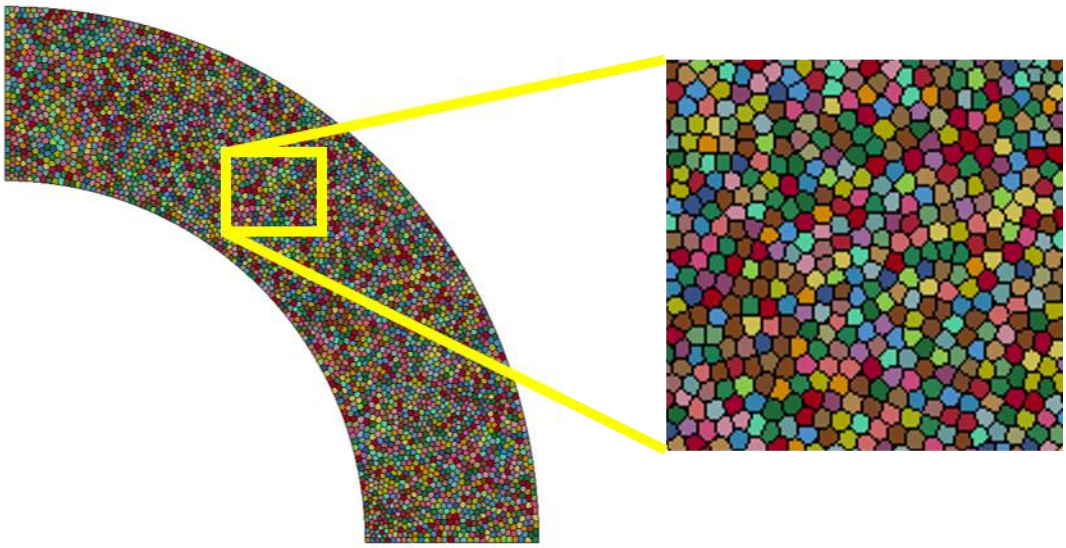

Figure 4-11: Sample mesh on quarter circle with particle size 100 μm. In this case the sample is fully densified (no porosity).

Particles of size 400, 100 and 40 μm were explored to investigate their probable influence on mechanisms of cavity collapse in this highly heterogeneous mixture. The effects of porosity were also explored by creating meshes that were fully dense and with initial porosity 13.9% as in the experiments.

TWC experiments are specifically designed to provide conditions of collapse that are almost radially symmetrical giving us the advantage to run calculations using a quarter of a circle. The dynamic behavior of all the elements: Al, W and Cu were modeled using Johnson-Cook [30] constitutive model with failure, the flow stress is described as:

$$\sigma_y = (A + B\bar{\epsilon}^{p\,n})(1 + c\ln\dot{\epsilon}^*)(1 - \left(\frac{T-T_0}{T_m-T_0}\right)^m). \qquad (1)$$

In this model, A, B, c, n, and m are model constants, $\bar{\epsilon}^p$ is the effective plastic strain, and $\dot{\epsilon}^*$ is the normalized effective total strain-rate, T_m is the melting temperature, and T_0 refers to the room temperature.

$$\epsilon^f = [D_1 + D_2 \exp(D_3\sigma^*)][1 + D_4 ln\dot{\epsilon}^*]\left[1 + D_5\left(\frac{T-T_0}{T_m-T_0}\right)^m\right], \quad (2)$$

$$\mathcal{D} = \Sigma \frac{\Delta\epsilon_p}{\epsilon^f}., \quad (3)$$

σ^* is the pressure divided by the deviatoric stress, and $\mathcal{D}$ is the damage parameter, the material is considered fully damaged and unable to support shear when the parameter is equal 1. The Grüneisen equation of state was used in conjunction with the Johnson-Cook constitutive model,

$$P = \frac{\rho_0 C^2 \mu\left[1+\left(1-\frac{\gamma_0}{2}\right)\mu-\frac{a}{2}\mu^2\right]}{\left[1-(S_1-1)\mu-S_2\frac{\mu^2}{\mu+1}-S_3\frac{\mu_3}{(\mu+1)^2}\right]} + (\gamma_0 + a\mu)E, \quad (4)$$

where C is the sound speed in the material, S_1, S_2, and S_3 are coefficients in the shock velocity-particle velocity equation. All the required values for the calculations are presented in Table 2 and were obtained from [32-35].

Table 4-2: Material parameters used in numerical simulations [32-35].

	A [Mbar]	B [Mbar]	*n*	*C*	*m*	C_0 [cm /μs]
Al	3.24x10^{-3}	1.114x10^{-3}	0.42	2x10^{-3}	1.34	0.52
W	1.506x10^{-2}	1.765x10^{-3}	1.00	1.6x10^{-2}	1.00	0.40
Copper	0.9x10^{-3}	2.92x10^{-3}	0.31	2.5x10^{-2}	1.09	0.394
	Density [g/cm^3]	G [Mbar]	Specific Heat [J/gK]	Melting Temp [K]	S_1	γ_0
Al	2.7	0.26	0.89	930	1.4	1.97
W	18.3	1.24	0.13	3640	1.24	1.67
Copper	8.92	0.44	0.385	1356	1.489	2.02
	D1	D2	D3	D4	D5	
Al	-0.77	1.45	-0.47	0.000	1.60	
W	0.00	0.33	1.50	0.000	0.00	
Copper	0.54	4.89	3.03	0.014	1.12	

The explosive is simulated using the John-Wilkins Lee (JWL) equation of state.

$$P = A\left(1 - \frac{\omega}{R_1 V}\right)e^{-R_1 V} + B\left(1 - \frac{\omega}{R_2 V}\right)e^{-R_2 V} + \frac{\omega E}{V} \quad (5)$$

where A = 78.69 GPa, B = 1.92 GPa, ω = 0.36, R1 = 4.61, and R2 = 1.06. These constants were obtained using CHEETAH 2.0 [36]. It is assumed that the explosive in the plane of interest detonates instantaneously, since the velocity of collapse, due to the relatively large thickness of copper, is significantly smaller than the detonation speed.

Fig. 12 show the results of simulations with Al-W sample where size of particles was 400 μm. The collapse of the cavity has lost its cylindrical symmetry, mostly in the inner surface of the sample being in contact with coper stopped tube. This behavior is contrary to results of experimental tests (Figs. 6), which were conducted using particles ten times smaller. In numerical calculations Al particles (depicted in red) have been squeezed between W particles (depicted in blue) indenting into copper stopper tube distorting its interface with sample and breaking axial symmetry of cavity collapse. Fig. 13 shows the plastic strain field corresponding to the calculations with particle size 400 μm. Figs. 12 and 13 allow to observe that the Al particles have accommodated most of the plastic strain with elongation in radial direction without significant deformation of W particles. Mostly radial plastic flow of Al particles caused W particles to rearrange themselves reducing distance between them in circumferential direction.

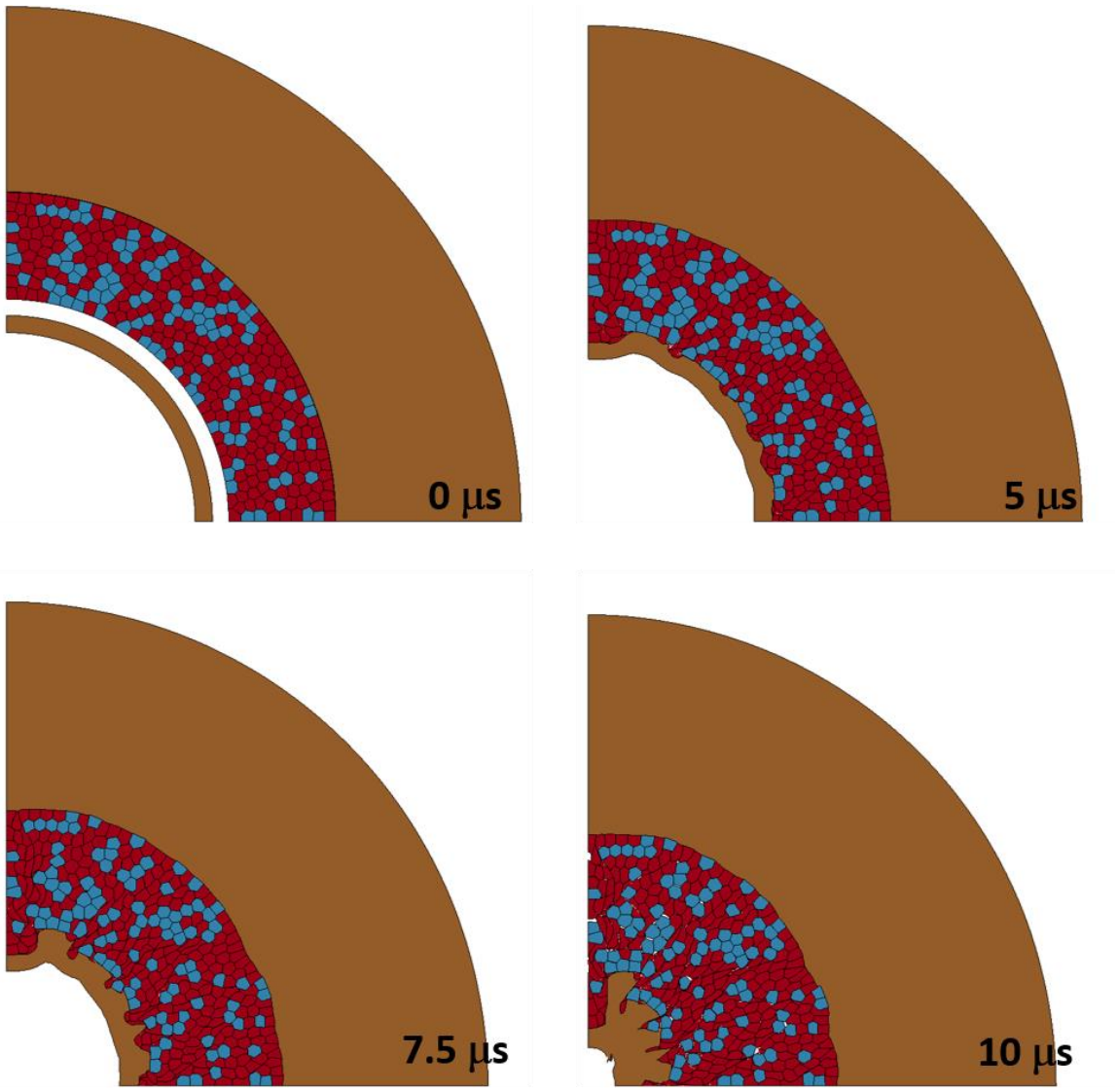

Figure 4-12: Simulation of quarter circle Al-W powder of 400 μm in size, 70% Al 30% W by volume, sample was initially fully dense. Multiple instances of collapse are shown.

Fig. 13 helps to emphasize the plastic strain distribution in this fully dense sample demonstrating that global strain is mainly accommodated by the deformation and flow of softer Al particles. It is clear that on later stages of

deformation network of highly localized regions of plastic flow appear along paths created by Al particles.

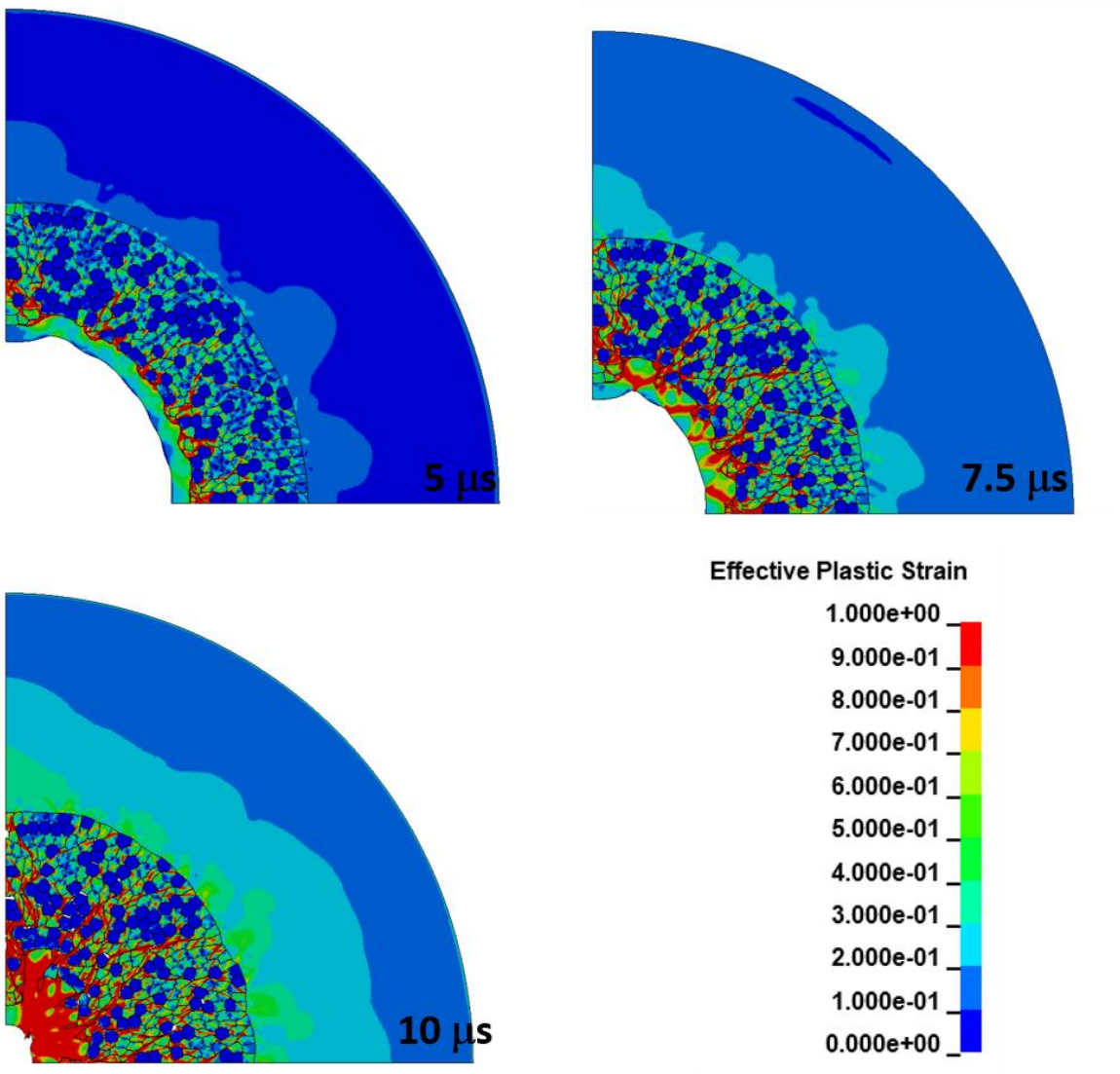

Figure 4-13: Plastic strain field of quarter circle Al-W powder of 400 μm in size, 70% Al 30% W by volume, initially fully dense. Multiple instances of collapse are shown.

Influence of the grain size on the mechanism of cavity collapse can be observed by comparing figures 12 and 14. The bigger particles have caused

bigger kinks in the inner surface that resulted in a significant distortion of axial symmetry, compared to the results with finer (100 μm size) grains.

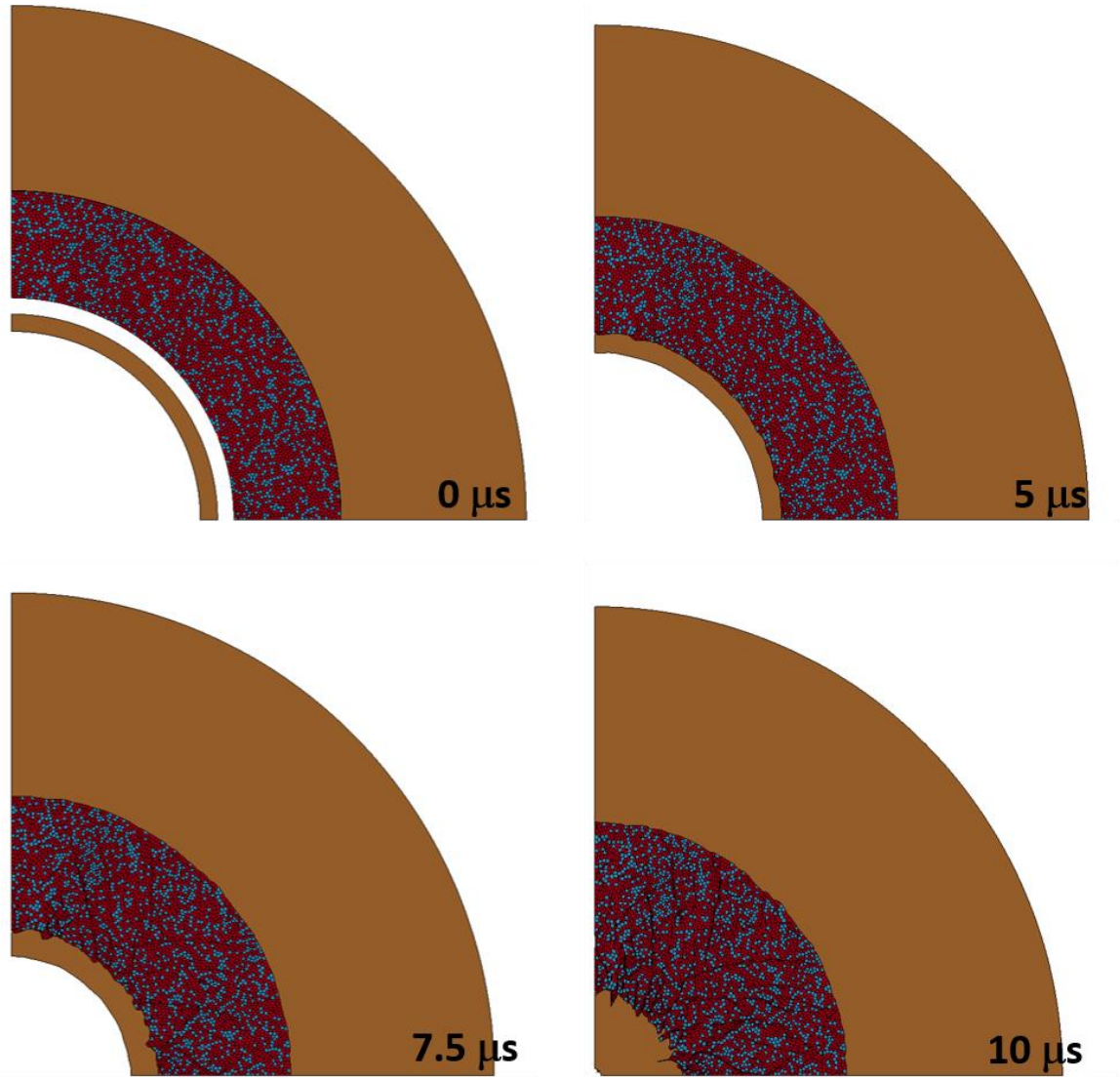

Figure 4-14: Simulation of quarter circle Al-W powder of 100 μm in size, 70% Al 30% W by volume, sample was initially fully dense. Multiple instances of collapse are shown.

The plastic strain filed reveals a similar phenomenon to observed in Fig. 13 with particle size (400 μm), where most plastic strain has been accommodated by

the softer Al particles while W particles have moved without experiencing high levels of plastic strain. In both cases (400 and 100 microns). Irregular pattern of localized shear bands following weak paths created by Al particles can be observed in the plastic strain field (Fig. 15), although they have not evolved into cracks.

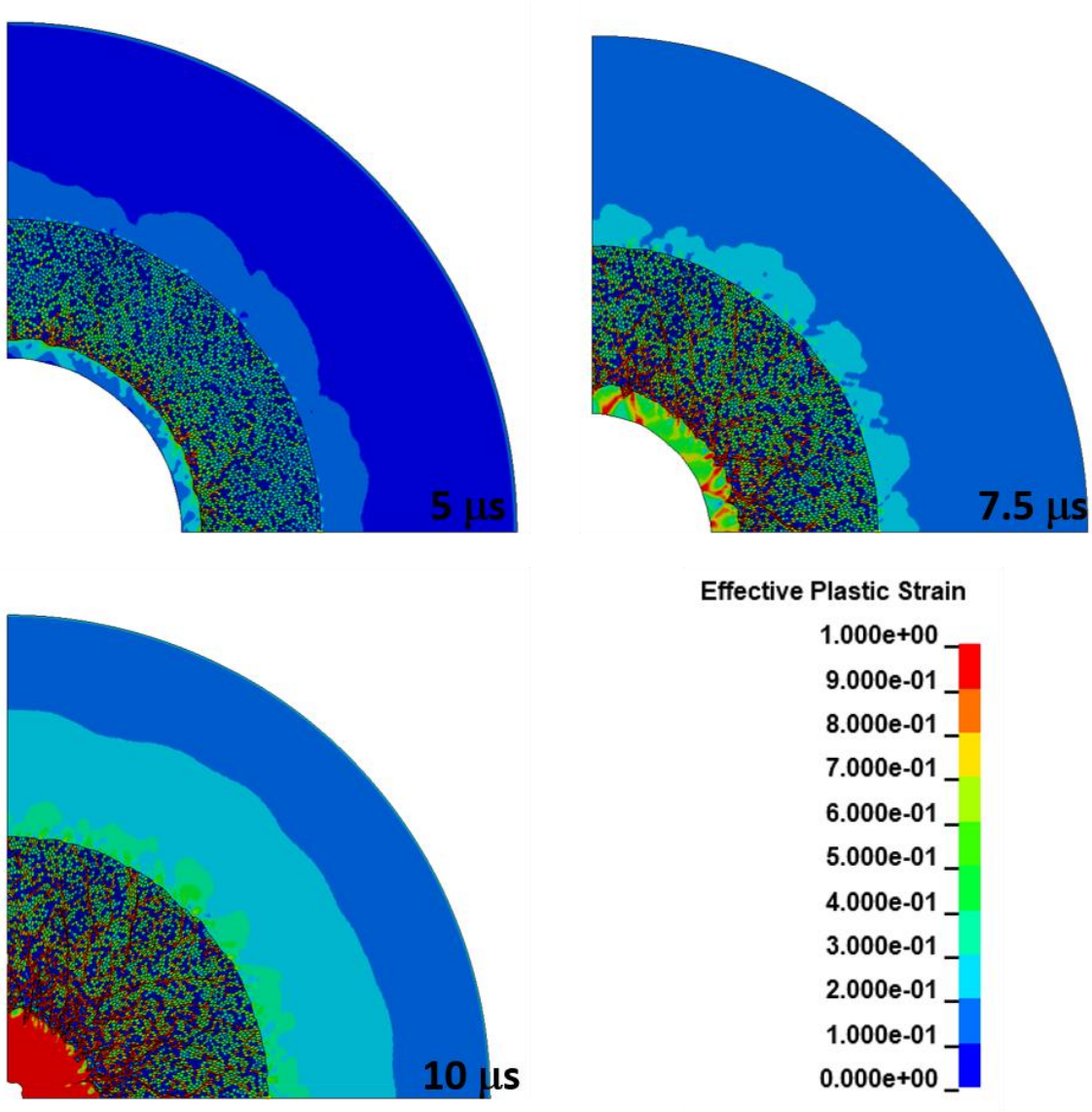

Figure 4-15: Plastic strain field of quarter circle Al-W powder of 100 μm in size, 70% Al 30% W by volume, initially fully dense. Multiple instances of collapse are shown.

To clarify this observation numerical simulations of a cavity collapse in the sample with size 40 μm were carried on. These calculations are computationally expensive, and in this dissertation, only partial results of an initially fully dense sample are showed (Fig. 19 and 20).

Fig. 16, shows the cavity collapse in a sample with grain size 40 micron in numerical simulations, similar to grain size in experiments. It is possible to observe how the kinks created in the Cu stopper interface with the sample are smaller in size, reinforcing the idea of a direct relationship between size of instabilities and grain size.

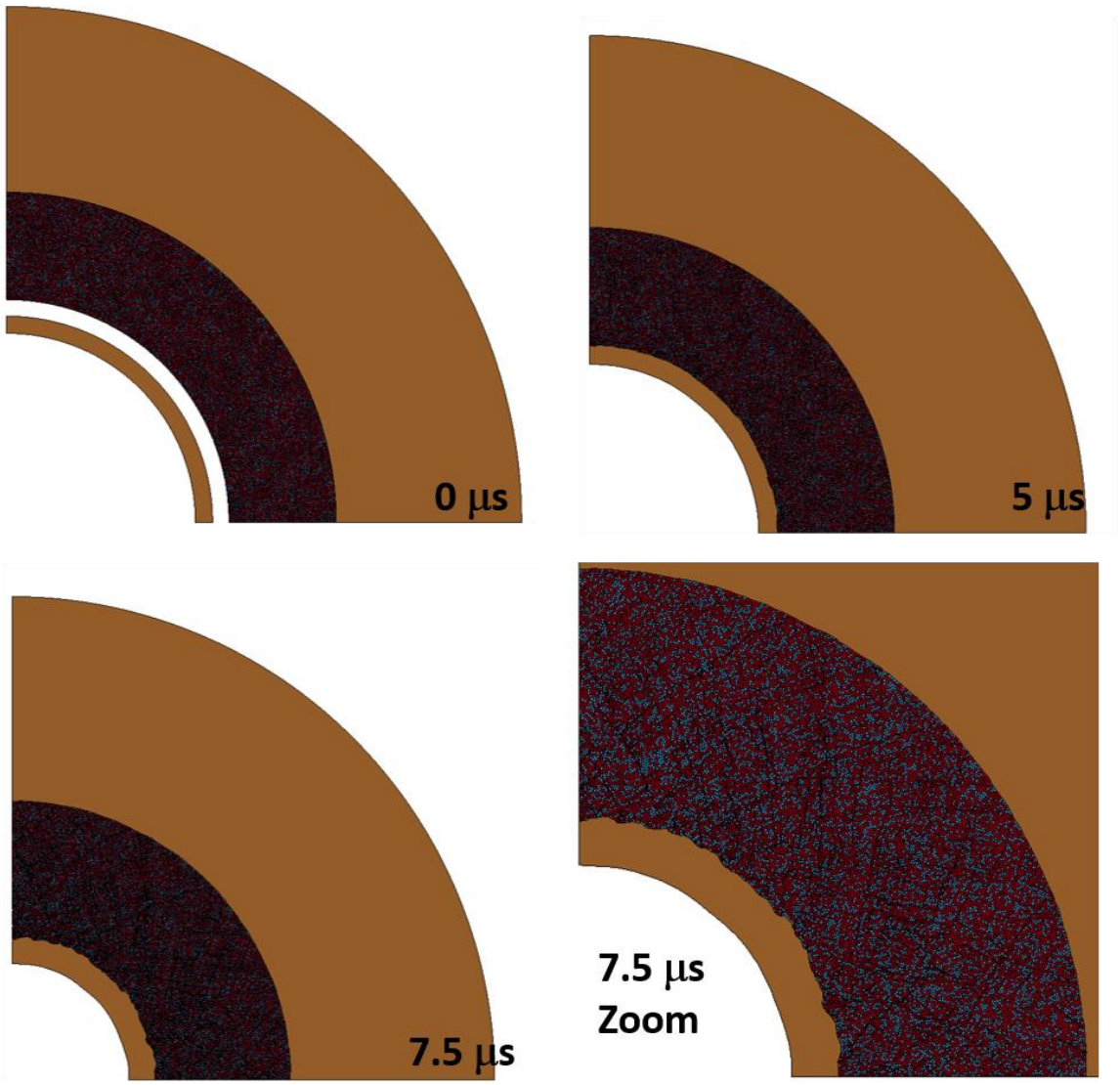

Figure 4-16: Simulation of quarter circle Al-W powder of 40 μm in size, 70% Al 30% W by volume, sample was initially fully dense. Multiple instances of collapse are shown.

Figure 17 corresponds to the plastic strain field of the sample with real grain size (40 μm). It is important to remark, that even at finer grain sizes, the same shear band phenomena can be observed, these shear bands are finer and seem to scale with particle size. Even at this particle size, no fracture can be observed.

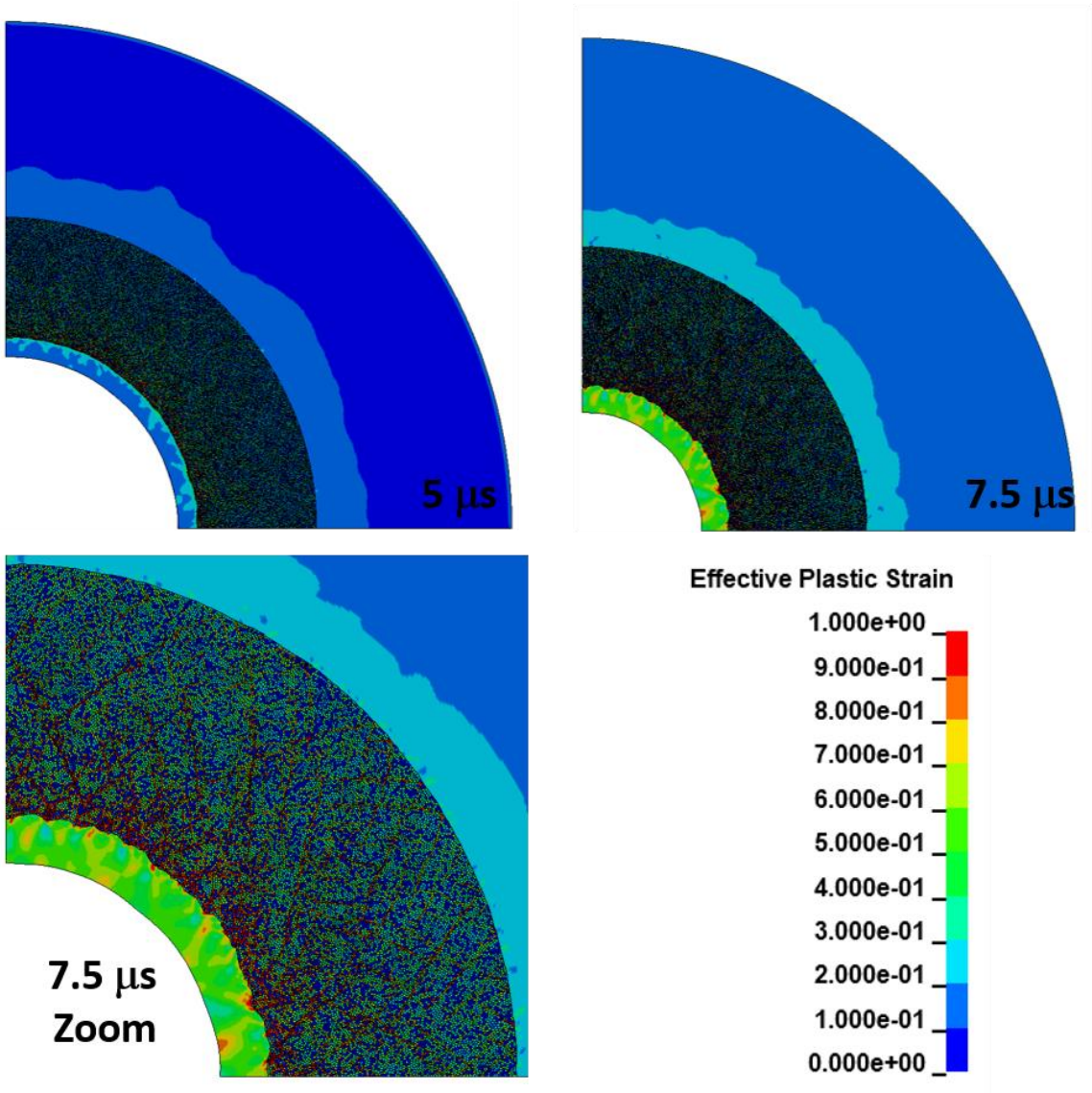

Figure 4-17: Plastic strain field of quarter circle Al-W powder of 40 μm in size, 70% Al 30% W by volume, initially fully dense. Multiple instances of collapse are shown.

To study the effects that porosity on mechanisms of cavity collapse, a sample with 100 μm particles and initial porosity 13.9%, similar to the experiments, was created by numerical modeling. An initial larger sample with larger porosity was designed which was quasistatically compressed to the right size of the sample

with required porosity. Fig. 18 represents the process of quasistatic collapse of the sample resembling the real cold isostatic compression of the samples.

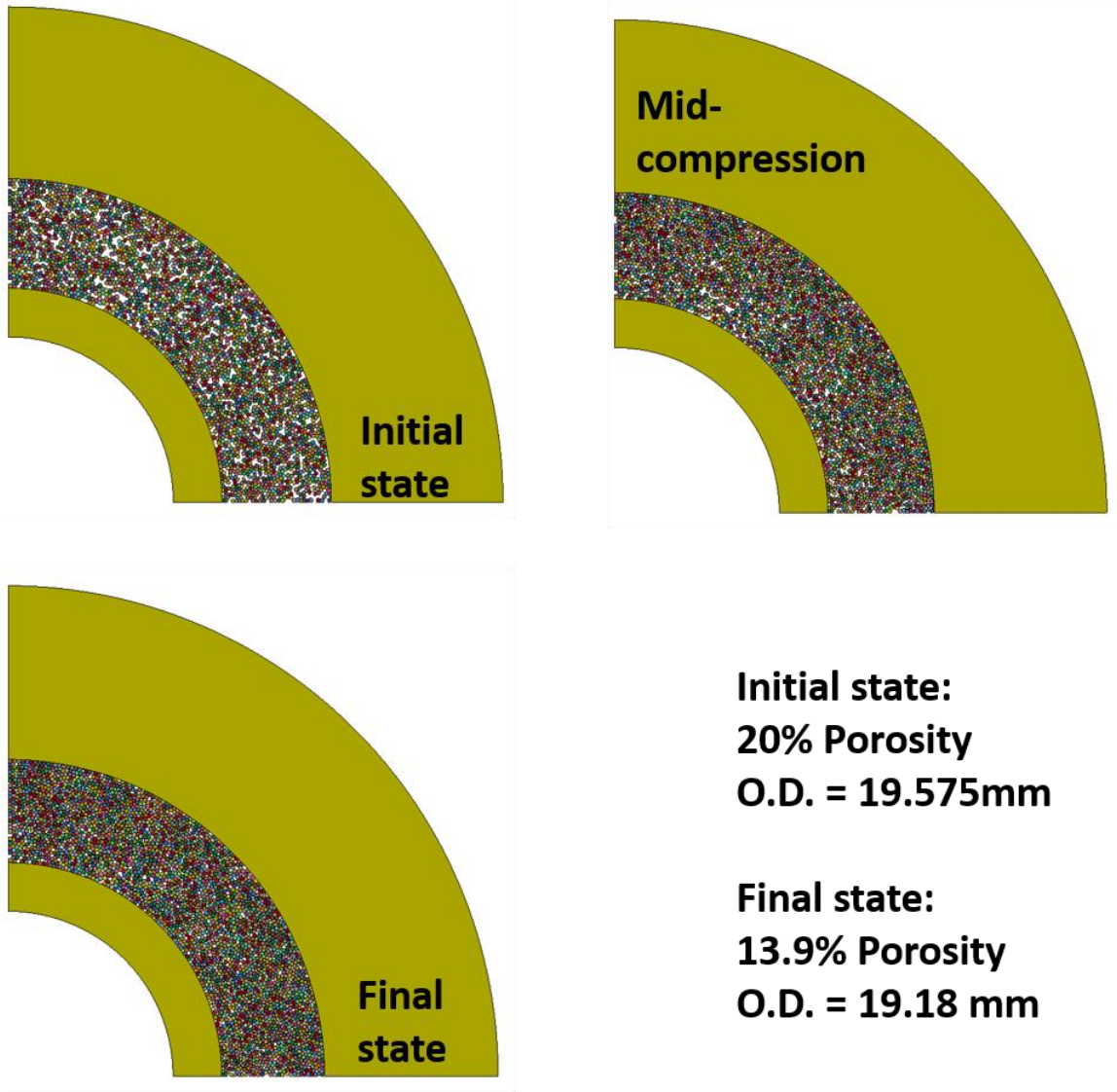

Figure 4-18: Illustration of process utilized to create a sample with initial porosity 13.9% that resembles samples utilized in experiment.

After the sample has been fictitiously “CIPed” or quasistatically driven to the desired sample size, a TWC numerical simulation is conducted. Figures 19 and

20 represent the results of the numerical calculations of samples with initial porosity.

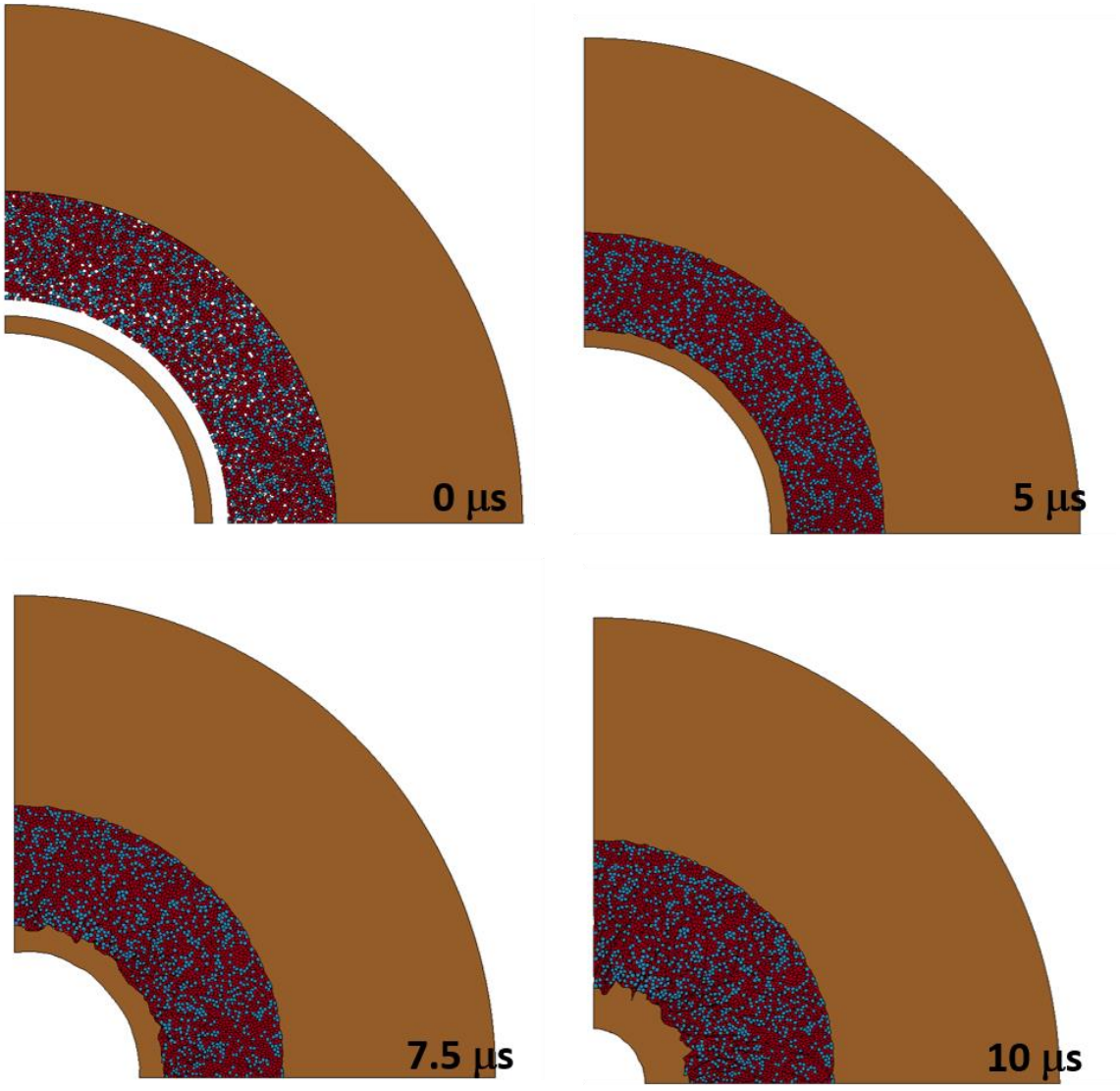

Figure 4-19: Simulation of quarter circle Al-W powder of 100 μm in size, with initial porosity 13.9%. Multiple instances of collapse are shown.

Comparison of Figs. 14 & 19 demonstrates a small differences in the collapse process. First, the shock loading wave fills out the pores which results in

a different state at comparable times. For example, at same instant in time, the porous sample has not fully collapsed unlike the fully dense sample. More interesting differences can be observed comparing the plastic strain fields demonstrating a different accommodation of strain.

Fig. 15 and 20 both depict that most of the plastic deformation is accommodated by Al particles, but also demonstrate a significant difference in the global strain accommodation. We can observe some effects of initial sample porosity. For example, the localization of plastic strain in a shear bands like pattern is retarded or alleviated. This can be explained due to some of the energy being spent to fill the pores in the porous sample compared to a shock pulse that is less dissipative traveling in a fully dense sample. Nevertheless, the instabilities observed in the inner surface are comparable. This might indicate that grain size is a more important variable in the initiation of instabilities.

Comparison Fig. 20 and Figs. 12, 14 and 16 demonstrate that reducing particles sizes by order of magnitude from 400 micron to 40 micron reduced sizes of “kinks” on the sample/copper stopper tube interface at similar final diameters of the latter. Strain localization is present with shear bands selecting paths of less resistance made of Al particles close to 45 degrees in both samples.

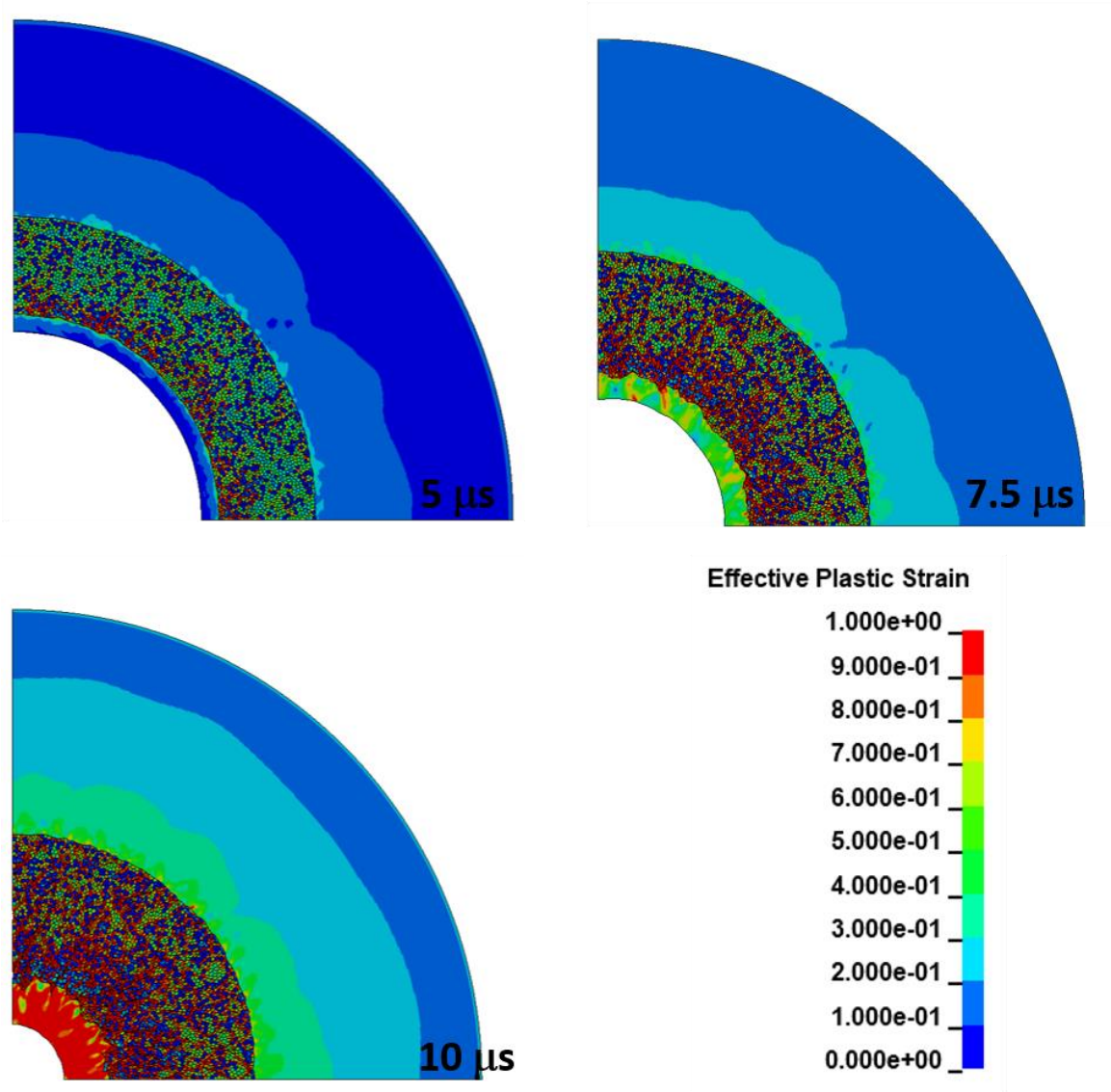

Figure 4-20: Plastic strain field of quarter circle Al-W powder of 100 μm in size, with initial porosity 13.9%. Multiple instances of collapse are shown.

4.4 Chapter Conclusions

Stability of cavity collapse in a highly heterogenous Al-W granular solid and porous samples was studied in numerical simulations and in experiments.

Numerical calculations demonstrated that cavity collapse with initial diameter 11mm in highly heterogeneous solid mixture of Al and W is destabilized by instability of plastic flow due to significant difference in strength of randomly distributed components – Al and W particles despite that the diameters of particles (400 microns) being significantly smaller than cavity diameter.

The mechanism of instability during cavity collapse in investigated highly heterogeneous mixtures of particles is different with shear instability caused by thermoplastic softening typical for solid metals (e.g., Ti and Ti64, Cu, SS304); instability due to microfracture softening observed in brittle granular materials (SiC, Al_2O_3) and in some steels (4340) with randomly distributed “defects”; or caused by cooperative buckling in laminates or crystal plasticity in monocrystals.

Reduction of particle size to 40 micron in solid and porous mixtures dramatically reduced a role of strain localization and enhanced the stability of cavity collapse. The initial porosity was eliminated on the stage of wave propagation in the sample and large strain plastic flow continued as in the initially solid sample. Nevertheless, initial porosity reduced effects of strain localization in the mixture with 40 micron particles.

Final geometry of explosively collapsed samples with initial particle sizes of Al and W particles being 40 microns and in mixture with sizes of W particles 1 micron and Al particles 40 microns was similar to observed in numerical modeling. Thus, collapse of macroscopic cavities in highly heterogeneous samples can be stabilized by relatively small particle sizes.

4.5 Chapter References

[1] A. Kapahi and H. S. Udaykumar, Dynamics of void collapse in shocked energetic materials: Physics of void-void interactions, Shock Waves **23**, 537 (2013).

[2] P.A. Bland, G.S. Collins, T.M. Davison, N.M. Abreu, F.J. Ciesla, A.R. Muxworthy and J. Moore, Pressure–temperature evolution of primordial solar system solids during impact-induced compaction, Nature communications,**5**, 5451 (2014).

[3] V.F. Nesterenko, *Dynamics of Heterogenous Materials* (Springer, New York, 2001).

[4] V.F. Nesterenko V.F., Lazaridi, A.N., and Pershin S.A., Localization of deformation in copper by explosive compression of hollow cylinders. Fiz. Goreniya Vzryva; **25**, 154 (1989).

[5] V.F. Nesterenko, M.P. Bondar, Localization of deformation in collapse of a thick walled cylinder. Combust Explosion Shock Waves, **30,** 500 (1994).

[6] V.F. Nesterenko, and M.P. Bondar, Investigation of deformation localization by the “thick- walled cylinder” method. DYMAT J, **1,** 245 (1994).

[7] Q. Xue, V.F. Nesterenko, and M.A. Meyers, Evaluation of the collapsing thick-walled cylinder technique for shear band spacing. Int J Impact Eng, **28,** 257 (2003).

[8] V.F. Nesterenko, M.A. Meyers, H.C. Chen, and J.C. LaSalvia, Controlled high rate localized shear in porous reactive media, Applied physics letters, **65**, 3069 (1994).

[9] P.H. Chiu, K.L. Olney, A. Higgins, M. Serge, D.J. Benson, and V.F. Nesterenko, The mechanism of instability and localized reaction in the explosively driven collapse of thick walled Ni-Al laminate cylinders. Appl Phys Lett, **102,** 241912 (2013).

[10] K.L. Olney, P.H. Chiu, M.S. Ribero Vairo, A. Higgins, M. Serge, D.J. Benson, and V.F. Nesterenko, Influence of mesoscale properties on the mechanisms of plastic strain accommodation in plane strain dynamic deformation of concentric Ni-Al laminates. J. Appl. Phys., **117**, 044302 (2015).

[11] M.M. Carroll, and A.C. Holt, Static and dynamic pore-collapse relations for ductile porous materials, J. Appl. Phys. **43**, 1626 (1972).

[12] M.M. Carroll, K.T. Kim, and V.F. Nesterenko, The effect of temperature on viscoplastic pore collapse, J. Appl. Phys. **59**, 1962 (1986).

[13] A. Kapahi and H. S. Udaykumar, Dynamics of void collapse in shocked energetic materials: Physics of void-void interactions, Shock Waves **23**, 537 (2013).

[14] D. J. Benson, V. F. Nesterenko, F. Jonsdottir, and M. A. Meyers, Quasistatic and dynamic regimes of granular material deformation under impulse loading, J. Mech. Phys. Solids **45**,1955 (1997).

[15] W. Tong and G. Ravichandran, Dynamic pore collapse in viscoplastic materials, J. Appl. Phys. **74**, 2425 (1993).

[16] Z. P. Tang,W. Liu, and Y. Horie, Numerical investigation of pore collapse under dynamic compression, AIP Conf. Proc. **505**, 309 (2000).

[17] M. A. Meyers, D. J. Benson, and E. A. Olevsky, Shock consolidation: Microstructurally-based analysis and computational modeling, Acta. Mater. **47**, 2089 (1999).

[18] S. R. Cooper, D. J. Benson, and V. F. Nesterenko, A numerical exploration of the role of void geometry on void collapse and hot spot formation in ductile materials, Int. J. Plasticity **16**, 525 (2000).

[19] Y. Shi and D. W. Brenner, Jetting and detonation initiation in shock induced collapse of nanometer-scale voids, J. Phys.Chem.C **112**, 6263 (2008).

[20] Baoxing Xu, Xi Chen, Weiyi Lu, Cang Zhao, and Yu Qiao, Non-dissipative energy capture of confined liquid in nanopores, Appl. Phys. Lett. **104**, 203107 (2014).

[21] P. Franco Navarro, P.H. Chiu, A. Higgins, M. Serge, D.J. Benson, and V.F. Nesterenko, V.F., Shear band patterning and post-critical behavior in AISI 4340 steel with different microstructure, International Journal of Impact Engineering, **112**, 144 (2018).

[22] Q. Xue, M.A. Meyers, and V.F. Nesterenko, Self organization of shear bands in stainless steel. Materials Science and Engineering: A, **384**, 35 (2004).

[23] Q. Xue, M.A. Meyers, V.F. and Nesterenko, Self-organization of shear bands in titanium and Ti–6Al–4V alloy. Acta Materialia, **50**, 575 (2002).

[24] S. Nemat-Nasser, T. Okinaka, V. Nesterenko, and M. Liu, Dynamic void collapse in crystals: computational modelling and experiments. Philosophical Magazine A, **78**, 1151 (1998).

[25] S. Nemat-Nasser, T. Okinaka, and V. Nesterenko, Experimental observation and computational simulation of dynamic void collapse in single crystal cooper, Materials Science and Engineering: A, **249**, 22 (1998).

[26] M.A. Meyers, V.F. Nesterenko, J.C. LaSalvia, and Q. Xue, Shear localization in dynamic deformation of materials: microstructural evolution and self-organization. Materials Science and Engineering: A, **317**, 204 (2001).

[27] K.L. Olney, P.H. Chiu, A. Higgins, M. Serge, T.P. Weihs, G.M. Fritz, A.K. Stover, D.J. Benson, and V.F. Nesterenko, The mechanisms of plastic strain accommodation during the high strain rate collapse of corrugated Ni–Al laminate cylinders. Philosophical Magazine, **94**, 3017 (2014).

[28] K. L. Olney, P.-H. Chiu, D. J. Benson, A. Higgins, M. Serge, and V. F. Nesterenko, Localized microjetting in the collapse of surface macrocavities, Physical Review E, **91**, 022405 (2015).

[29] P.H. Chiu, K.L. Olney, D.J. Benson, C. Braithwaite, A. Collins, and V.F. Nesterenko, Dynamic fragmentation of Al-W granular rings with different mesostructures. Journal of Applied Physics, **121**, 045901 (2017).

[30] C. Talischi, G.H. Paulino, A. Pereira, and I.F. Menezes, PolyMesher: a general-purpose mesh generator for polygonal elements written in Matlab. Structural and Multidisciplinary Optimization, **45**, 309 (2012).

[31] G. R. Johnson, and W. H. Cook, Fracture characteristics of three metals subjected to various strains, strain rates, temperatures and pressures, Eng. Fract. Mech. **21**, 31 (1985).

[32] T.J. Holmquist, D.W. Templeton, and K.D. Bishnoi, Constitutive modeling of aluminum nitride for large strain, high-strain rate, and high-pressure applications, International Journal of Impact Engineering, **25**, 211 (2001).

[33] K.L. Olney, P.H. Chiu, C.W. Lee, V.F. Nesterenko, and D.J. Benson, Role of material properties and mesostructure on dynamic deformation and shear instability in Al-W granular composites, Journal of Applied Physics, **110**, 114908 (2011).

[34] E. Vitali, and D.J. Benson, Modeling localized failure with arbitrary Lagrangian Eulerian methods, Computational Mechanics, **49**, 197 (2012).

[35] D. Steinberg, *Equation of state and strength properties of selected materials* (Lawrence Livermore Natioral Laboratory, Livermore, 1996).

[36] L. F. Fried, P. C. Souers, *CHEETAH 2.0 User's Manual* (Lawrence Livermore National Laboratory, Livermore, 1998).

Chapter 4, in part is currently being prepared for submission for publication of the material. Franco Navarro, P., Benson, D.J., Nesterenko, V.F., The dissertation author was the primary investigator and author of this material.

Chapter 5 : Shear band patterning and post-critical behavior in AISI 4340 steel with different microstructure

5.1 Introduction

Shear localization is an important deformation and failure mechanism for materials that have been subjected to high strain rate de- formation, e.g., high-velocity impact and penetration, in high-speed metal cutting, and during collapse of cylindrical cavities [1–5]. Shear bands have been extensively studied starting with the paper by Zener and Hollomon [6], which introduced adiabatic shear bands (ASBs). It was recently brought to light [7] that Tarnavskii in 1928 [8] and Davidenkov and Mirolubov in 1935 [9] gathered the first evidence of ASBs in steels.

In this paper, we focus on the pattern of multiple shear bands in AISI 4340 steel (as-received vs. hardened) using the Thick-Walled Cylinder (TWC) method. This post-critical behavior is important in many applications, it being responsible for the material's ability to dissipate the mechanical energy due to viscoplastic deformation. The explosively driven method was proposed by Nesterenko et al. [4,10–16] to investigate spontaneous shear instability, patterns of shear bands in solid and granular materials, and buckling of laminates (inert and reactive). It also was used by other researchers [17,18] and later modifications of this method employed electromagnetic drive [19–23], Hopkinson bar [24], and gas gun [25].

Analytical approaches to describe the thickness and spacing of adiabatic shear bands have been developed starting with the paper by Grady and Kipp [26] and detailed explanations can be found in [2,27–29]. Nevertheless, these models describe only qualitative results and fail to capture both length and spacing observed in experiments. Although results are in the same order of magnitude, they are off by a factor of 3–4 [21].

Numerical calculations were used to study formation and evolution of ASBs and their emerging self-organized patterns in the geometry corresponding to the TWC test in different materials such as Cu, Ti, and AISI 304 L in [19–21,30–33]. The difference in these approaches lies in the failure criteria that give a positive feedback mechanism for the strain localization. These authors invoked energy or strain criteria [21–23] weakening the material and resulting in nucleation of a shear band. In [22] the authors connected rapid development of localization in Ti6Al4V to dynamic recrystallization and delay in shear localization in CP-Titanium and in MgAM50 to a significant twinning absent in Ti6Al4V. The highest number of shear bands in SS304L is attributed to both twinning and martensitic transformation being active.

In [31], the authors emphasized a need of defects to nucleate shear bands in their numerical approach. The interplay between the number of shear bands and its propagation is directly related to the initial defect distribution. In [32,33], the authors reproduced the nucleation of strain localization and generated a pattern of shear bands without the introduction of any defects in the materials or the meshes.

The authors employed a temperature perturbation that helped break the homogeneity and cause localization.

AISI 4340 steel has unique properties and applications related to high strain rate deformation of penetrators and armor plates. Extensive research has been conducted to understand its response to shear band nucleation and propagation [34–36].

The failure mechanism of AD95 ceramic/4340 steel composite armor during the impact of a tungsten projectile at a velocity of about 820 m/s was studied in [34]. Different failure modes corresponding to various target configurations were observed.

In [35], the authors study penetration of ogive-nose steel projectiles made from 4340 (R_c 45) on concrete targets. The projectiles had a speed of either 400 m/s or 1200 m/s. In experiments, it was shown that penetration depth increased with speed, but once the data were normalized by a length scale determined by the model of the authors, the data collapsed on a single curve.

The authors of [36] conducted a study of penetration in semi-in- finite 4340 targets by tungsten-alloy projectiles at 1500 m/s. In this study, experimental results are compared to numerical simulations that use the Johnson–Cook material model; this is analogous to what is done in this work. The authors found that when the ratio of target diameter to projectile diameter is below 20 the target resistance rapidly de- creases. With the use of simulations, the authors found that penetration

increases when the region of plastic flow is close to the radial boundary of the target.

Numerous studies have focused on understanding the formation of multiple shear bands in the machining process of this steel at various cutting speeds, ranging from 100 m/min to 3000 m/min [37–39]. The main interest of understanding shear band formation in the cutting process is related to the surface finish, which could greatly affect the performance of the finished part. It was found that, in general, cutting speeds as well as characteristics of the steel, like hardness, dictate chip formation. Specifically, in [37], the authors conducted a computational study using the Johnson-Cook material model with damage to simulate chip morphology. This approach is similar to what we present in the present paper.

The single shear band formation in AISI 4340 steel due to high velocity impact was investigated in papers [40–44]. Different techniques, like Hopkinson bar tests or expanding cylinder tests, are used to produce strain rates in the range 1^{02}–10^{5} s^{-1}, without the control of the total global strains. It was concluded that initiation sites for the formation of shear bands occurred at the interface of the carbide inclusions and the matrix. In [42], the authors used numerical calculations to reproduce adiabatic shear observed in experiments using a Hopkinson bar. Their simple criteria to predict the onset of instabilities is based on a maximum shear stress under a minimum critical shear strain rate. It proved to be capable of predicting the start of the in- stability, but not its evolution on the post-critical stage.

The previous research has been focused on understanding the development of single shear bands through experiments and numerical simulations and understanding the mechanism of their formation and propagation in AISI 4340 steel. At the same time, in many applications a pattern of shear bands is generated, which determined the performance of the devices or quality of the machining. In this paper, we generated a pattern of shear bands in a plane strain controlled environment using the Thick-Walled Cylinder (TWC) method to understand the interplay and propagation of multiple shear bands in AISI 4340 steel under a controlled global strain. Two types of AISI 4340 steel with different initial microstructure were explosively driven with identical conditions of the dynamic deformation. These specimens had different mechanical properties (e.g., strength and ductility) due to a heat treatment described below. They had similar thermophysical properties (e.g., density, heat capacity, and thermal conductivity), which favorably restricts the number of variable properties of the samples. Numerical simulations were conducted to understand the influence of the material mechanical properties on the generated pattern of self-organized shear bands. A different distribution of defects was introduced in the material to better replicate the experimental results.

5.2 Experimental procedures and results

Cylindrical samples were machined from the cold-drawn AISI 4340 steel rod processed by air melt (McMaster-Carr) and had an initial outer diameter (O.D.) of

17.02 mm, inner diameter (I.D.) of 12.07 mm, and height of 20 mm. They were used as inserts in the TWC method and were dynamically collapsed under plane strain conditions. The details of the method can be found in [14]. The explosive driver was a gelled nitromethane (96% nitromethane, 4% PMMA) diluted 5% by mass with glass microballoons. The same driver was used in [15] and [16] and allowed for the fine tuning of the explosive loading.

As-received AISI 4340 steel has proeutectoid ferrite and pearlite (alternating layers of ferrite and cementite). Some specimens were austenized at 845°C, oil quenched, and tempered at 205°C for two hours to increase its hardness. During the first austenizing stage of hardening, the steel was completely transformed to austenite. In the next stage, during fast oil-quenching, the steel was transformed to a martensite microstructure resulting in a very hard and brittle material. To enhance its ductility and toughness, tempering was carried out at 205 C to produce a tempered martensite structure, which consisted of thin precipitated platelet and spherical carbides immersed in the tem- peredmartensite lath matrix [45,46]. The microstructure of as-received and hardened AISI 4340 steel are presented in Fig. 1.

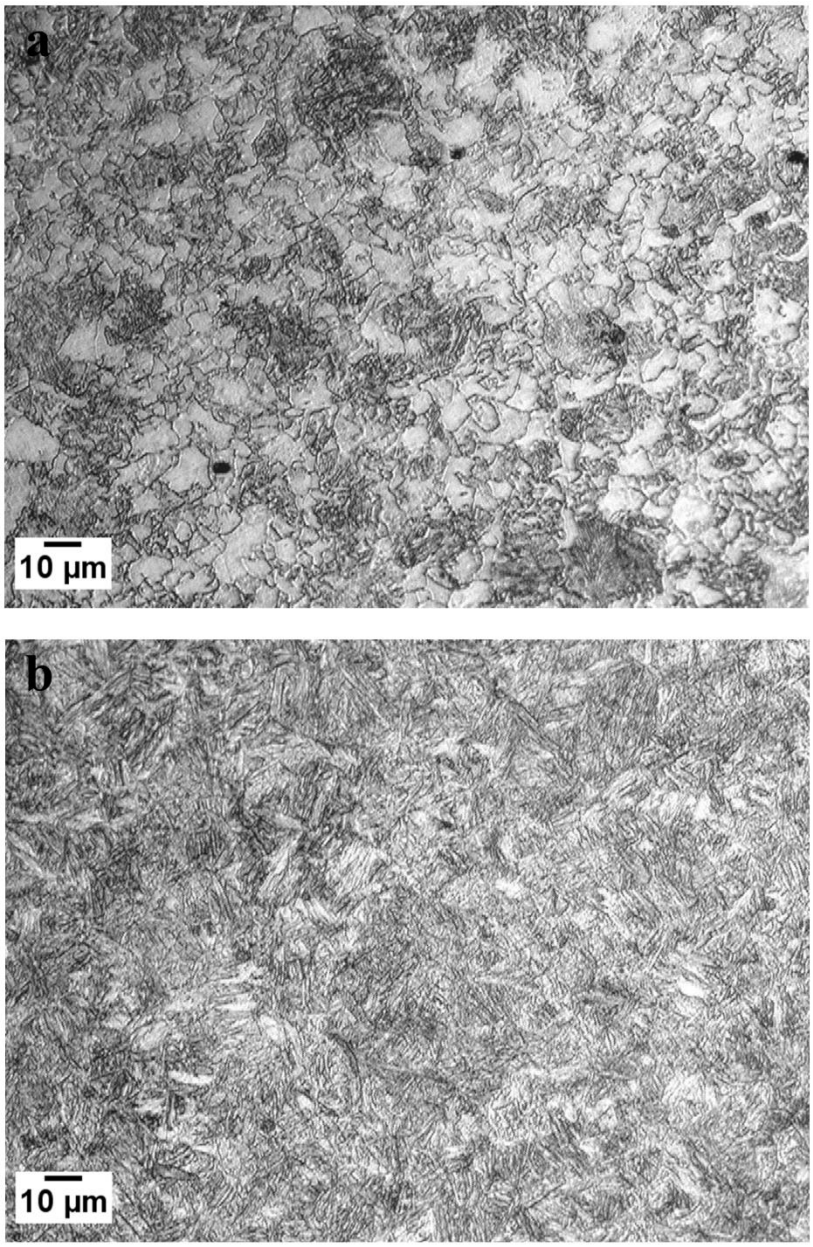

Figure 5-1: The microstructure of as-received AISI 4340 (ferrite is white and pearlite is dark gray) - (a) and hardened AISI 4340 steel with martensite microstructure- (b).

The properties of the investigated steels are presented in Table 1. The microhardness of as-received and hardened AISI 4340 steel before testing was measured according to ASTM E92 Standard. A LECO Model M400-H1 hardness

tester with a diamond-shaped indenter was used and a load of 500 gf was applied on the samples for 15 s. After the heat treatment, the microhardness of AISI 4340 steel increased significantly from 2789 ± 23 MPa to 5420 ± 45 MPa. The ultimate tensile strength (σ_u), 0.2% yield strength ($\sigma_{0.2}$), elongation (δ), true strain at fracture (δ_f), thermal conductivity at 100 °C (k), specific heat (S), and plane- strain fracture toughness (K_{IC}) are taken from [47], where corre- sponding properties of as-received and hardened AISI 4340 steel were reported.

Table 5-1: Mechanical properties of as-received and hardened AISI4340 steels [47]

Sample Type	σ_u[47] (MPa)	$\sigma_{0.2}$[47] (MPa)	δ[47] (%)	δ_f[47] (%)	k[47] (W/m·K)	S[47] (J/kg·K)	K_{IC}[47] (MPa√m)	Microhardness (MPa)
As-received	745	470	22	21	42.7	475	110	2789±23
Hardened	1980	1860	10	10	42.7	475	48	5420±45

The TWC experiments were conducted on the steel specimens with two different wall thicknesses of copper stopper tubes: 1 and 0.5 mm. These stopper tubes were collapsed into rods with different diameters; tubes with 1 mm wall thickness resulted in a “small global strain” and tubes with 0.5 mm wall thickness produced a “large global strain” in the samples. Strains were calculated assuming the global cylindrical symmetry of the deformation and using the initial radii (r_0) and final radii (r_f) of the corre- sponding points per Eq. (1), and the results are shown in Table 2,

$$\varepsilon_{\text{eff}} = \frac{2}{\sqrt{3}} \ln\left(\frac{r_0}{r_f}\right) \quad (1)$$

Images of the samples after tests are presented on Figs. 2–7. Fig. 2 presents the case of as-received AISI 4340 samples corresponding to small (Fig. 2(a)) and large (Fig. 2(b)) global strains. It is clear that the global cylindrical symmetry of the specimens was preserved and thus global strains in the inner surfaces of the collapsed samples are computed: ϵ_{eff}= 0.53, for the case of small global strain, and ϵ_{eff} = 0.80 for the large global strain. The small-diameter hole in the center of the collapsed copper stopper corresponds to the axial jetting removing only small amounts of the copper, which was verified by comparison of the final diameter of the copper stopper tube in experiments and based on mass conservation.

Table 5-2: Final diameters of the AISI 4340 samples, which have identical initial O.D. (17.02 mm) and I.D. (12.07 mm), and the corresponding effective strains (ε_{eff}).

	Final O.D. (mm)	Final I.D. (mm)	ε_{eff} (on the inner surface)	ε_{eff} (on the outer surface)
as-received (small ε)	14.22	7.63	0.53, start of shear localization	0.21
as-received (large ε)	13.44	6.05*	0.80, slight grow or shear localization	0.27
hardened (small ε)	14.11	7.42*	0.56, developed shear bands pattern	0.22
hardened (large ε)	13.36	5.86*	0.83, fragmentation of the sample	0.28

*Estimated values used initial and final radii of copper stopper tube based on mass conservation

A pattern of nucleated shear bands can be observed in the case of small global strain (Figs. 2(a) and 3(a)). In the case of larger global strain (Figs. 2(b) and 3(b)), the pattern of longer shear bands has developed closer to the inner surface of the sample. Thus, a reasonable estimate of the nucleation strain for the formation of shear band pat- terns in as-received AISI 4340 steel is ϵ_{eff} = 0.53. This value is close to the strain value of 0.5, sufficient to induce a shear instability in pearlitic AISI 4340 steel in dynamic punch-impact tests at an average strain rate of 18,000 s^{-1} [48]. It seems that the spacing along the inner radius between nucleated shear bands is smaller in the sample with smaller global strain (about 200 μm, Fig. 3(a)) compared to the spacing between longer shear bands (with lengths > 100 μm) in the sample with larger global strain (about 300 μm, Fig. 3(b)). This behavior is similar to that observed in AISI 304 steel, where the development of some shear bands arrests the growth of others due to unloading [13]. In both collapsed samples, no catastrophic failure occurred.

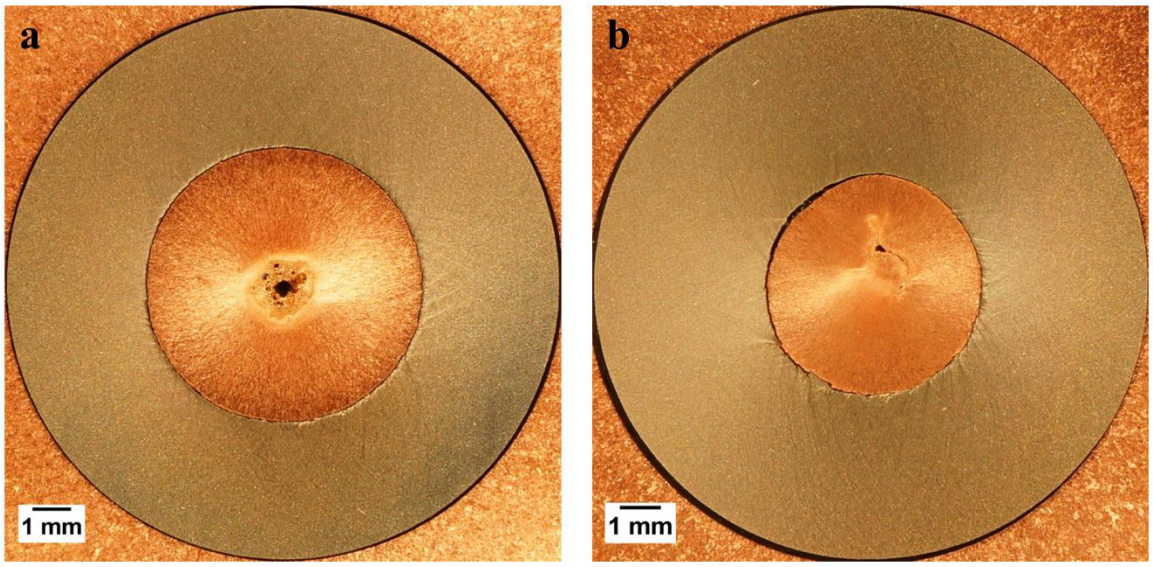

Figure 5-2: Pictures of the collapsed AISI 4340 samples (as-received) at a different strain in the inner surface: (a) strain 0.53, initial wall thickness of the copper stopper tube 1 mm and (b) strain 0.80, initial wall thickness of the copper stopper tube 0.5 mm.

The dramatically different behavior of the hardened AISI 4340 steel is presented in Fig. 4. At both tests with different wall thickness of copper stopper tubes (used to generate different global strains), well-developed shear bands are evident. From Fig. 4 it is possible to conclude that the difference in microstructure and change of the mechanical properties resulted in the creation and propagation of shear bands throughout the entire steel sample. As a result, the symmetry of the collapsed steel samples has been lost and catastrophic failure of the steel specimen happened. Still, the collapsed sample at small strains in Fig. 4(a) mostly preserved a cylindrical symmetry and thus Eq. (1) can be used to estimate the global strains in the inner surface of the sample as ϵ_{eff} = 0.56, which can be considered as being close to the nucleation strain for the formation of shear bands

in hardened AISI 4340. But comparison between Figs. 2a, 3a, and 4a demonstrate that critical strain for shear band propagation is smaller in hardened AISI 4340.

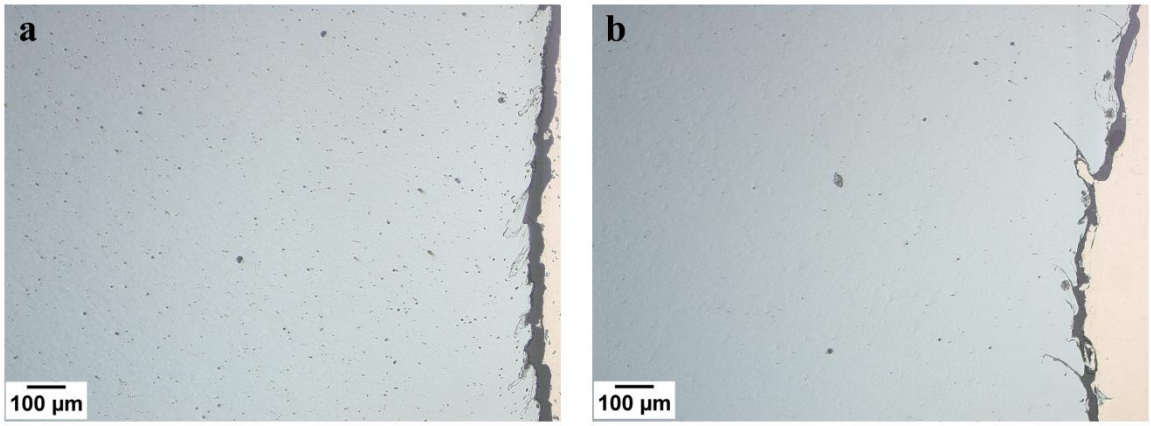

Figure 5-3: Pattern of nucleating shear bands in the vicinity of the contact with copper stopper tube in collapsed AISI 4340 (as-received) samples at different values of strain in the inner surface: (a) strain 0.53, initial wall thickness of the copper stopper tube 1 mm and (b) strain 0.80, initial wall thickness of the copper stopper tube 0.5 mm.

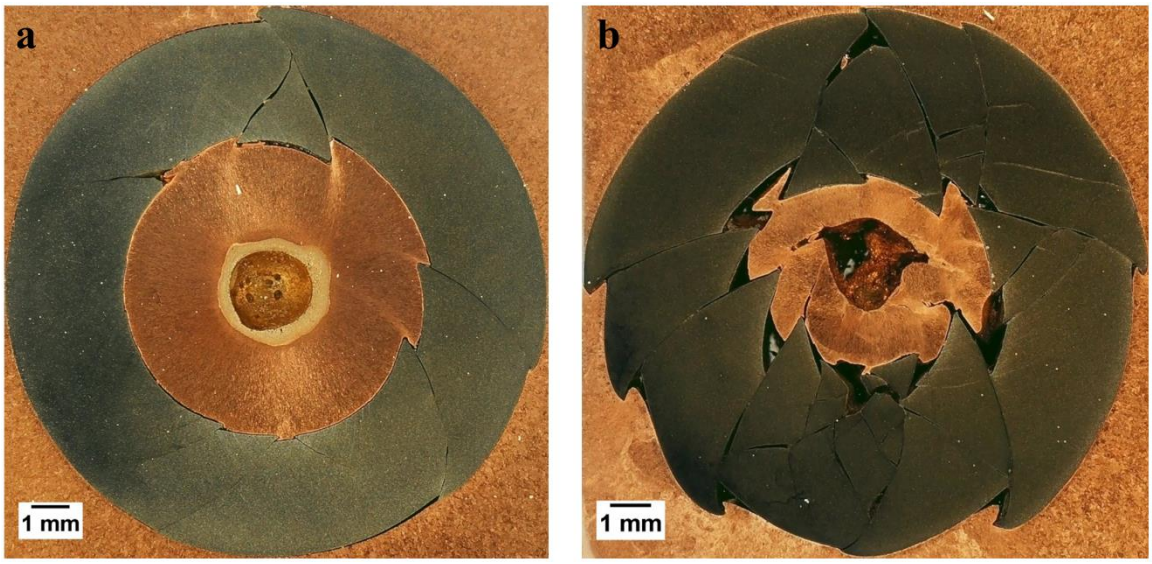

Figure 5-4: Pictures of the collapsed AISI 4340 samples (hardened) at a different strain in the inner surface: (a) strain 0.56, initial wall thickness of a copper stopper tube 1 mm and (b) collapse steel sample corresponding to the initial wall thickness of a copper stopper tube 0.5 mm.

Microstructures of the collapsed AISI 4340 (hardened) samples are shown in Figs. 5 and 6. White-etching or transformed bands were revealed by etching with 2% nital. A just-nucleated shear band without microcrack and a well-developed, partially cracked and bifurcated shear band are shown in Fig. 5(a). A larger magnification of the former is presented in Fig. 5(b) and segments of developed shear bands are shown in Figs. 5(c) and (d). The bifurcation of the shear band presented in Fig. 5(c) seems due to its interaction with the weak interface between the inclusion and the surrounding matrix. Several microcracks inside a white-etching band were observed in Fig. 5(d), which can be precursors for macrocracks. We can also observe the microcrack present between segments of white-etching band (Fig. 6), which was probably originated from an initially transformed segment of shear band.

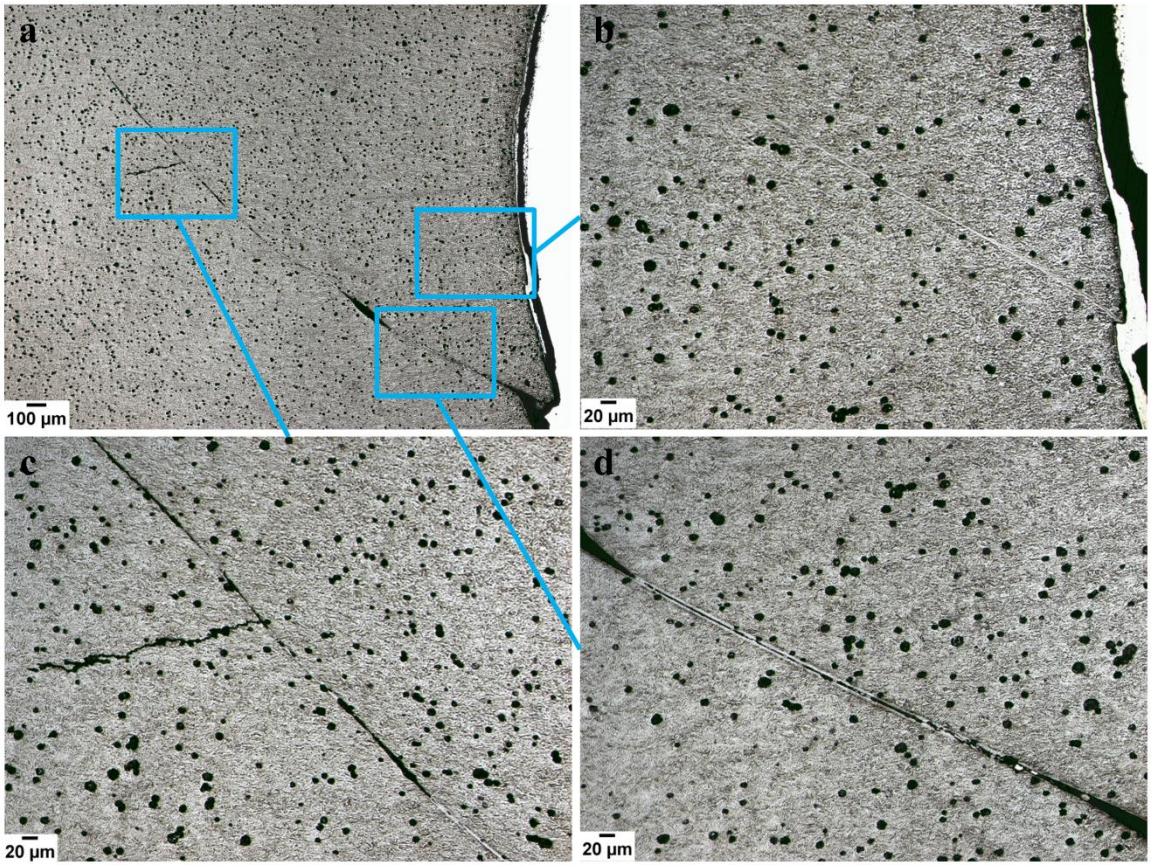

Figure 5-5: Microstructures of the collapsed AISI 4340 (hardened) sample with strain 0.56 in the inner surface (initial wall thickness of the stopper copper tube 1 mm). Just nucleated and well-developed shear bands are presented in (a); a white-etched nucleated shear band without microcrack shown in (b). Bifurcated shear band developed probably due to the weak interface between inclusions and the matrix, is shown in (c). The coalescence of microcracks into macrocrack in a white-etching band is shown in (d).

In tests with as-received AISI 4340, only deformed shear bands were observed (Fig. 7). Hardened AISI 4340 steel showed the segments of transformed (white-etching) bands presented in Figs. 5 and 6, corresponding to different global strains in tests with the wall thickness of the copper stopper tube equal to 1 and 0.5 mm. A controlled heating and cooling process of 4340 steel was used to change the microstructure and obtain higher strength and lower ductility. During this treatment, the martensite phase transformation was completed before TWC

tests. It is possible that inside well-developed shear bands, initial martensite phase was transformed to austenite due to localized heating and re- turned back to martensite with much smaller grain sizes than in the initial material due to subsequent fast quenching. This resulted in a white transformed shear bands with different appearance than the surrounding martensite matrix.

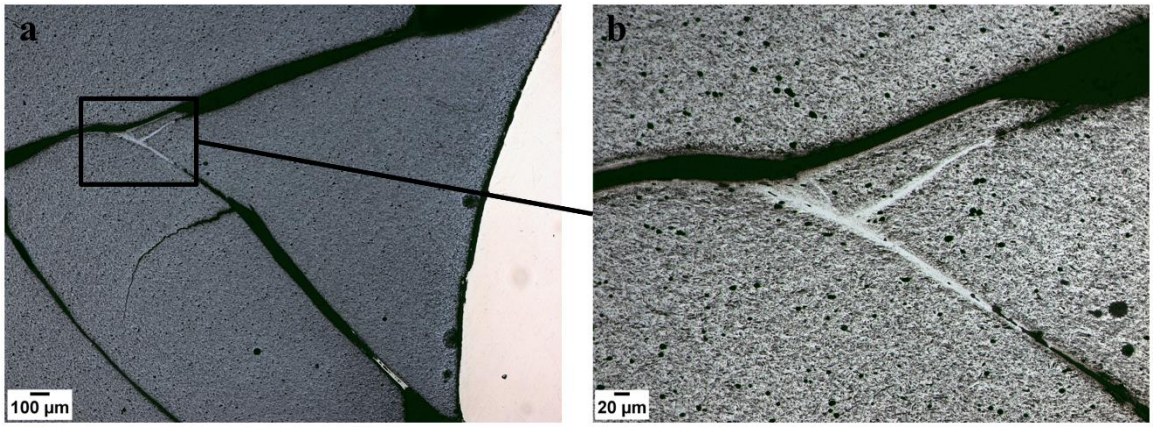

Figure 5-6: Microstructures of bifurcated shear band split into two transformed shear bands and later into crack, at different magnifications in the collapsed hardened AISI 4340 sample at strain in the inner surface 0.83 (initial wall thickness of the copper stopper tube 0.5 mm). Sample was etched with 2% nital.

The dependence of the types of shear bands on steel microstructure was observed in [49], where white-etching shear bands were only found in quenched and quenched-and-tempered steel.

We can observe microcracking inside a shear band in the area adjacent to the copper stopper tube (Fig. 7), which probably initiated at the interface between the matrix and inclusions, extending into the deformed shear bands.

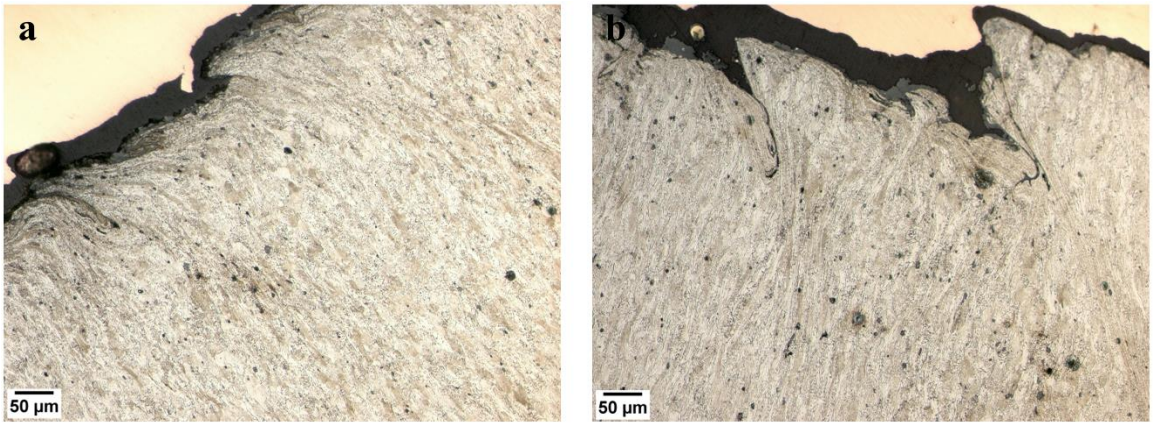

Figure 5-7: Shear bands in the collapsed AISI 4340 (as-received) sample etched with 2% natal at different values of strain in the inner surface: (a) strain 0.53, initial wall thickness of the copper stopper tube 1 mm and (b) strain 0.80, initial wall thickness of copper stopper tube 0.5 mm.

The microstructure of the shear bands in Fig. 5 suggests that the propagation mechanism of shear bands in the hardened AISI 4340 sample is related to the interfacial microcracking between the inclusions and matrix similar to [50,51] (the authors of [51] mentioned that voids are nucleated at the interface of large MnS inclusions and matrix, which then nucleated a sheet of voids on the much smaller cementite particles between the large voids formed at the MnS particles). Coalescence of voids and microcracks at the interfaces between the inclusions and matrix in the shear band can result in void sheet formation [50,51]. A similar mechanism is probably responsible for the propagation of shear bands and their bifurcation as well as a zig zag shape of bifurcated shear band in hardened AISI 4340 steel (Fig. 5(c)).

The authors of [52] emphasized that the presence of hard particles or secondary precipitates in the ferrite matrix of steel facilitates the occurrence of

ASBs. In comparison to pearlitic steels of similar hard- ness, martensitic steels have a greater tendency to form localized shear bands [53]. Different mechanical properties, owed to different micro- structures (pearlite or martensite, concentration and shape of cementite inclusion) of as-received and hardened AISI 4340, are responsible for their different behavior in our experiments.

We can speculate that the difference in post-critical behavior of as- received and hardened AISI 4340 steel results from the difference in dissipation of mechanical energy in the bulk of the samples. In the latter case, global strains are accommodated mostly by the pattern of shear bands with low shear strength inside the bands, resulting in reduced dissipation. This may explain a larger area of the central melt in the collapsed copper stopper tube caused by the concentration of the kinetic energy of the collapsing tube and axial micro jetting (compare Figs. 2 and 4).

It is interesting that spontaneous shear bands developed in hardened AISI 4340 created the forced shear bands in the copper stopper tube, evident in Fig. 4(b). In general, copper is very resistant to spontaneous shear localization due to its low strength and high heat conductivity.

5.3 Numerical calculations

Numerical calculations were performed using LS-DYNA with the Johnson-Cook [54] material model coupled with the Mie-Grüneisen equation of state. In the Johnson-Cook material model, the flow stress is given by:

$$\sigma_y = (A + B\bar{\epsilon}^{p\,n})(1 + c \ln \dot{\epsilon}^*)(1 - T^{*m}). \quad (1)$$

In this model, A, B, c, n, and m are model constants, $\bar{\epsilon}^p$ is the effective plastic strain, and $\dot{\epsilon}^*$ is the normalized effective total strain-rate. The action of the explosive was modeled using a pressure boundary condition similar to [21,30] that collapses the central cavity in about 10 μs. To capture damage, we used the approach presented in [54]:

$$D = \sum \frac{\Delta\epsilon}{\epsilon^f}, \quad (2)$$

where $\Delta\epsilon$ is the increment of equivalent plastic strain during an integration cycle and ϵ^f is the equivalent strain at fracture, when D=1, fracture occurs and the element is eroded. The general expression for the strain at fracture is given by:

$$\epsilon^f = [D_1 + D_2 \exp D_3 \sigma^*][1 + D_4 \ln \dot{\epsilon}^*][1 + D_5 T^*], \quad (3)$$

with $\sigma^* = P/\sigma_{\text{eff}}$, i.e., pressure divided by the effective stress, and $D_1 - D_5$ are experimentally determined parameters [54].

The geometry used in the numerical calculations is similar to the experimental set up and it is shown in Fig. 8(a). As mentioned before, we use a pressure boundary condition (Fig. 8(b)) to replace the ex- plosive used in the experiments; a separate calculation with the Jones- Wilkins–Lee equation of state for the explosive was made to assure a good reproduction of the experimental conditions. The process of the collapse of the steel sample was driven to the same outer radius of the samples as observed in the experiments. The mesh size used in the numerical calculations of the collapse of the AISI 4340 steel sample (shown in red in Fig. 8(a)) was about 10 μm, for the copper stopper (inner blue circle), and

the mesh size was about 15– μm and for the copper driver (outer blue circle) about 50 μm. This mesh size was selected to approximate correctly the characteristic size of shear bands observed in the experiments. All the numerical calculations were executed in plane strain conditions that correspond to the experimental conditions.

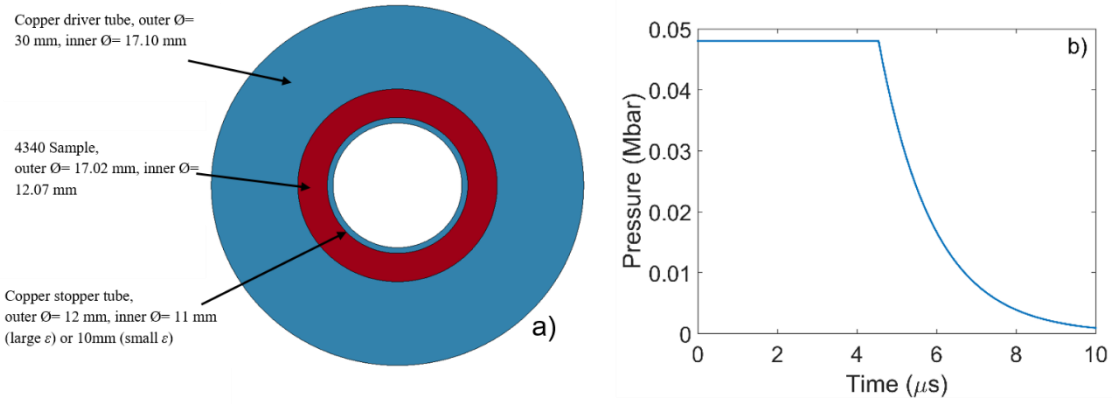

Figure 5-8: (a) Geometry of the Thick-Walled Cylinder method (b) Pressure dependence on time corresponding to the boundary conditions used in numerical calculations.

The mechanical properties of AISI 4340 steel and copper were taken from [54,55], for both cases, the reference strain rate is 1 s^{-1}. It is important to remark that the constants used in the Johnson–Cook model are selected to fit experimental stress-strain curves at different strain rates and temperatures.

Table 5-3: Material parameters for Johnson-Cook material model [54,55].

	A [GPa]	*B* [GPa]	*n*	*C*	*m*
AISI 4340	792	510	0.26	1.4×10^{-2}	1.03
4340 Hardened	2100	1750	0.65	2.8×10^{-3}	0.75
Copper	90	292	0.31	2.5×10^{-2}	1.09
	Density [kg/m^3]	Elastic Modulus [GPa]	Poisson's Ratio	Specific Heat [J/kgK]	Melting Temp [K]
AISI 4340	7830	207	0.29	477	1793
4340 Hardened	7830	207	0.29	477	1793
Copper	8960	124	0.34	383	1356
	D1	D2	D3	D4	D5
AISI 4340	0.05	3.44	-2.12	0.002	0.61
4340 Hardened	0.05	3.44	-2.12	0.002	0.61
Copper	0.54	4.89	-3.03	0.014	1.12

At first, simulations were conducted with nominal material properties corresponding to AISI 4340 and no defects were introduced. The result presented in Fig. 9 corresponds to a uniform collapse of the steel specimen without the initiation of shear localization, even though the model had softening mechanisms related to the thermal softening and damage accumulation. The same uniform collapse was observed for hardened AISI 4340. Fig. 9 shows that the inner surface was naturally subjected to the highest level of strain with the width of the heavily deformed zone increasing with decrease of the final diameter.

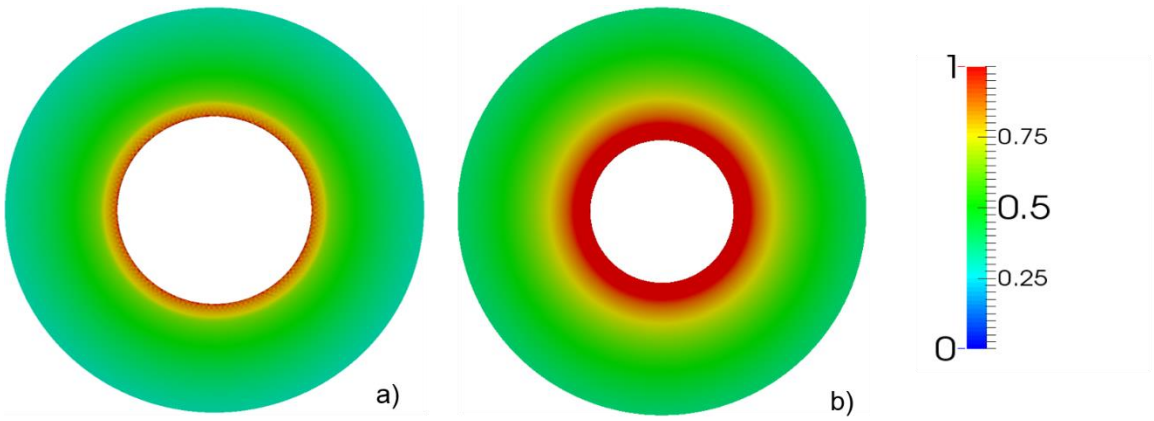

Figure 5-9: Collapsed AISI 4340 steel cylinder at (a) small global strain (1 mm wall thickness copper stopper) and (b) large global strain (0.5 mm wall thickness copper stopper). The colors on right correspond to different level of effective plastic strains.

The TWC test was designed in a way wherein the massive copper driver tube collapses the samples having different strengths with a similar strain rate. To illustrate, this point we a conducted numerical calculation of the collapse process with different strength of the samples. Fig. 10 shows the total velocity of the inner surface of the col- lapsing samples for AISI 4340 and for hardened AISI 4340.

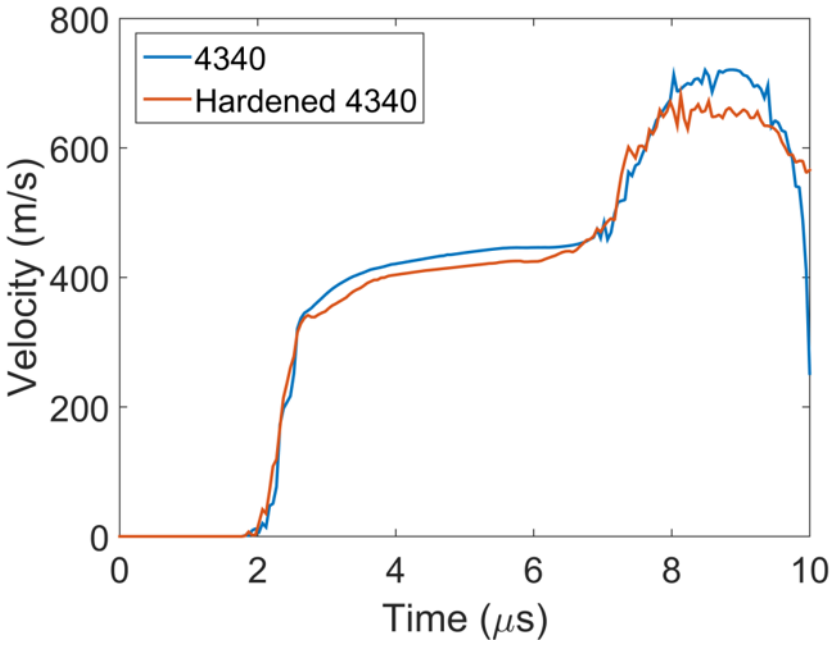

Figure 5-10: Total velocity of inner surface in numerical simulations of steel specimen on Thick-Walled Cylinder experiment of AISI 4340 (blue line) and heat treated 4340 (red line).

It is clear that the dynamics of collapse of these two samples with dramatically different strength are practically identical in the geometry of the TWC test.

5.3.1 Influence of the number of defects on shear localization and post-critical behavior of AISI 4340

The results of the numerical calculations demonstrate that high strain plastic flow, even with a softening mechanism incorporated, does not result in shear instability (Fig. 9) contrary to the experimental observations (Figs. 3–7). It should be mentioned that steel samples do have a significant number of inclusions (Figs.

5–7) whose interfaces with the surrounding matrix are potential sites for microcracking serving as a softening mechanism essential for shear localization [50,51]. This mechanism should be taken into account to explain the observed phenomena of shear instability and the pattern of shear bands.

It has been shown that the “defects” introduced in the numerical calculations have a direct effect on the number of nucleated and evolved shear bands in the steel specimen corresponding to the TWC experimental set up [31]. The authors of this paper found that smaller scatter of material properties effectively increases the number of gen- erated shear bands, but their length decreased. Thus, the interplay of material imperfections and instabilities plays a critical role in the final pattern of shear bands.

To explore the role of initial defects on nucleation and propagation of shear bands, we performed calculations corresponding to collapsed AISI 4340 samples with nominal properties (Table 3) in the majority of mesh elements and variable percentages (5%, 2.5%, 1.5%, and 0.5%) of mesh elements that have a different initial yield strength scaled by the nominal yield strength:

$$\sigma_{y_{Scaled}} = \sigma_y \cdot P. \quad (5)$$

The “defects” are randomly distributed through the steel specimen and the scaling factor P follows the following normal distribution $\mathcal{N}(0.1, 0.0025)$, the first number corresponds to the mean value of the scaling factor and the second to the square of the standard deviation. The purpose of these calculations was to determine which “defect” content is sufficient to describe the patterns of shear

bands observed in our experiments. The selected mean value of the scaling factor ensured that the results of numerical calculations were close to the experimentally observed patterns of shear bands. Fig. 11 presents the results of these calculations.

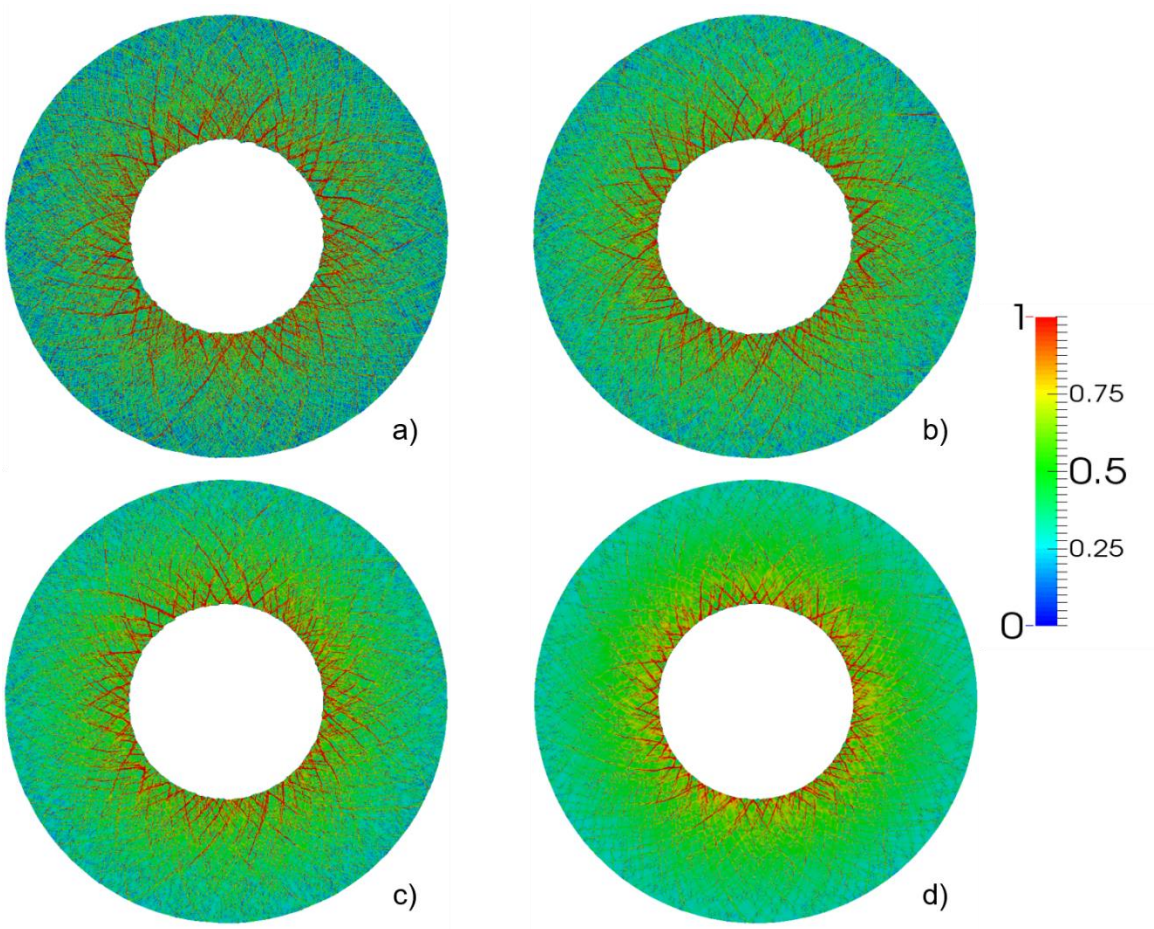

Figure 5-11: Fringe plots of effective plastic strain in the collapsed AISI 4340 samples with nominal properties in the majority of mesh elements and variable percentages (a) 5%, b) 2.5%, c) 1.5%, and d) 0.5%) of mesh elements with a different initial yield strength. Data correspond to large global strain (the test with 0.5-mm-wall copper stopper tube), outer diameter in all figures is 13.44 mm. "Defects" are randomly distributed through the specimen and follow a normal distribution $\mathcal{N}(\mathbf{0.1}, \mathbf{0.0025})$.

From the presented results, it is clear that the number of "defects" introduced in the calculations directly related to the number of nucleated shear

bands and the length of the evolved shear bands. Fig. 11(a), with 5% of mesh elements with “defects” shows a large number of shear bands that have evolved in the specimen in both clockwise and counter clockwise direction, which is contrary to what is observed in the experiments where a dominant direction is exhibited. Similarly, with 2.5% and 1.5% of “defects” (Fig. 11(b) and (c)), one cannot observe a dominant direction of shear band propagation and the number of shear bands is obviously greater then was observed in experiments.

The case with 0.5% “defects” present shear bands with significantly smaller lengths than in previous cases shown in Fig. 11(a)-(c). In Fig. 11(d), the developed shear bands only go through about one third of the specimen, and we can see much of the localization contained within this area. In the other cases, Fig. 11(a)–(c), we can see how shear bands propagate more than half way through the specimen or all the way to the outer surface. We consider that the case with 0.5% “defects” is the closest to the observed experimental behavior of AISI 4340 (Fig. 2(b))

It is important to emphasize that symmetrically-nucleated shear bands propagating in both directions at 45° to the radius lose symmetry while they propagate, with some of the shear bands developing faster, which in turn blocks shear band propagation normal to these.

We conducted numerical calculations at two different strain levels of collapsed samples by using different wall thickness of copper stopper tubes, 0.5 mm and 1 mm. The results of these calculations are presented in Fig. 12. Copper

is simulated defect-free (it is resistant to shear localization at these strains) while defects are introduced in 0.5% of the elements in AISI 4340 steel to initiate the localization process (Section 4.3.2).

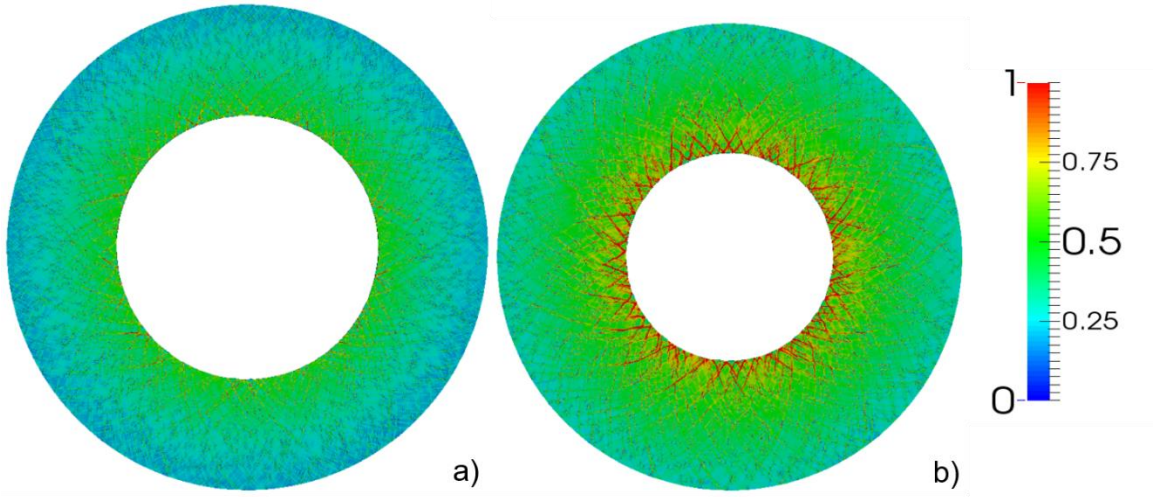

Figure 5-12: Fringe plot of the effective plastic strain in AISI 4340 Steel with (a) 1 mm and (b) 0.5 mm wall thickness of copper stopper tube corresponding to similar outer diameter of samples to experiments (see Table 2), percentage of elements with the scaled strength 0.5%. Outer diameter in (a) is 14.22 mm and in (b) 13.44 mm.

Figs. 12(a) and 12(b) represent the results of numerical calculations that correspond to similar outer diameters to those observed in experiments (Table 2). These figures should be compared to the pattern of nucleated shear bands in the experiments shown in Fig. 2. In the case of 1 mm wall thickness copper stopper tube (Figs. 2(a) vs 12(a)), the final outer diameter of steel sample in the experiments (14.22 mm) corresponds to a final inner diameter of 7.75 mm in our calculations. The measured inner diameter results in an equivalent effective strain of 0.208; this effective strain is close to the effective strain found in experiments of 0.21. The distance between shear bands that can be identified in the specimen in

the numerical calculations, denoted by red zones in Fig. 12(a), are in the range 1-1.1 mm.

For the case of 0.5mm wall thickness of copper stopper tube (Figs. 2(b) vs. 12(b)), the final diameter in experiments is 13.44 mm (Table 2), which corresponds to the final inner diameter in calculations 5.991 mm. This inner diameter is related to an effective strain of 0.2744 compared to 0.27 from the experiments. In this case, the well-established shear bands (the ones that have reached a quarter of the specimen) are spaced about 0.75 mm apart. The decrease of spacing is due to the reduced radius of the inner surface of the sample and not related to the increase of the number of shear bands. In numerical calculations, we see that some shear bands are developing faster as we observe in experiments (Fig. 2(b)).

In these numerical calculations, no clear preferential direction of the bands has been observed. Shear bands nucleated in both counter and clockwise directions, but some of the shear bands stop growing once they interact with each other.

5.3.2 Shear localization and post-critical behavior of heat treated AISI 4340

The patterns of shear bands in AISI 4340 and in the hardened AISI 4340 in the experiments were dramatically different at similar strain and strain rates. The heat treatment significantly changed the micro- structure and steel properties. In our numerical calculations, we used experimentally identified material constants in the Johnson-Cook model for hardened AISI 4340 [53]. We retained percentage of

defects equal to 0.5%, which resulted in good agreement with the observed experimental behavior of AISI 4340 (Fig. 2(b)). This allowed us to minimize the number of variable initial properties of the samples, focusing instead on the role of material constants on the pattern of shear bands.

It is important to notice, that the damage constants D1-D5 (which determine the deletion of elements) were selected the same for both steels. In a separate set of numerical calculations, we explored the case with the values of these constants being half, double, and four times larger than used in this paper. It resulted in no significant changes of the pattern of shear bands other than less or more accentuation of the shear bands. In the numerical model, these constants are used to estimate the damage on each element and to trigger their erosion (deletion), but this will not effectively cause major changes of the location of the bands. This reinforces the fact that the bands are mainly dictated by the initial number and location of defects.

Fig. 13 show the fringe plot of the plastic strain for the case of small global strains (1 mm wall thickness of the copper stopper tube) at different times. It is clear from the comparison of Figs. 12 and 13, that changing material properties resulted in the dramatic change of shear band patterns in the numerical calculations (compare Figs. 12(a) and 13(b)) taken at the similar inner diameters of the samples.

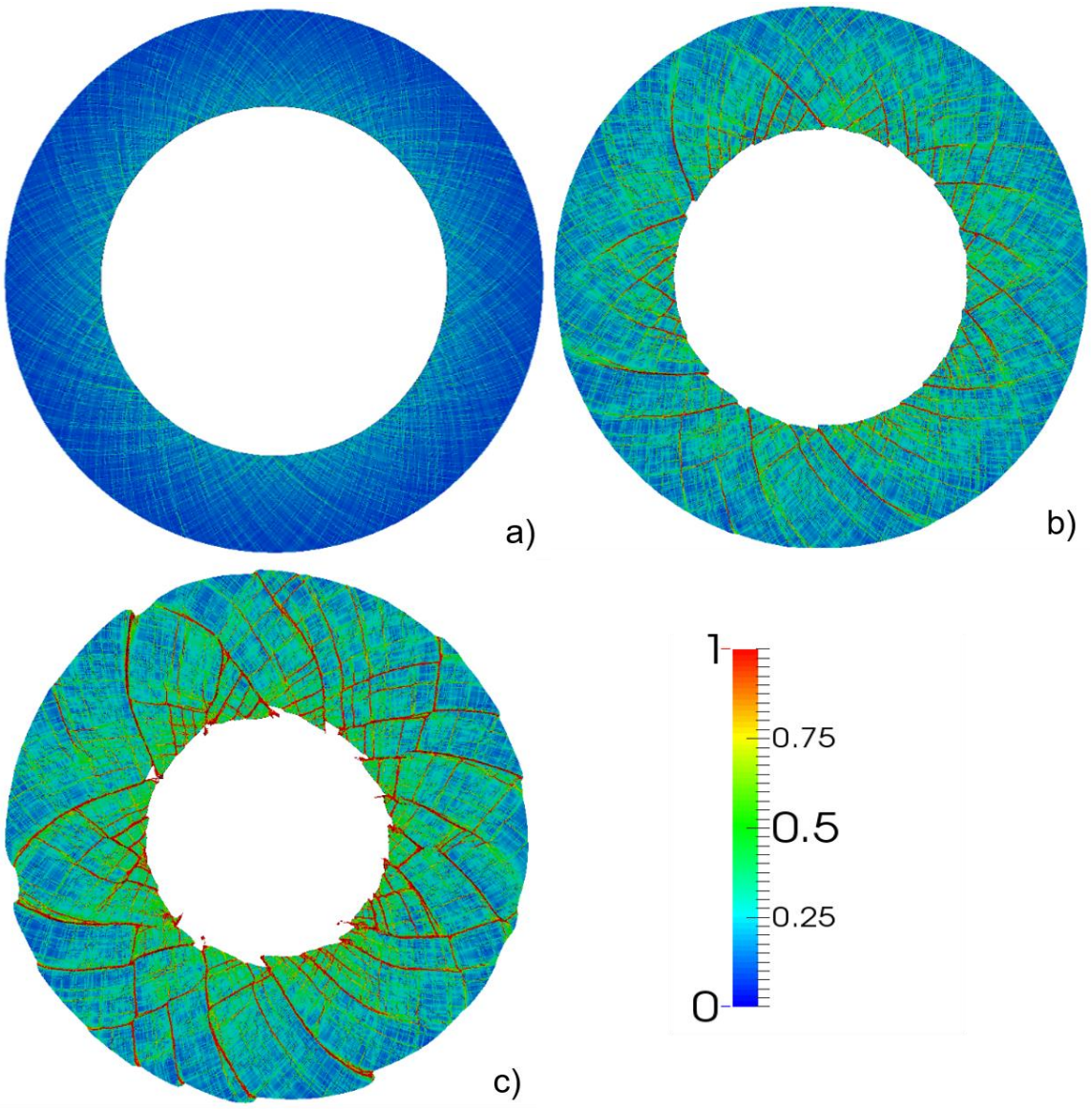

Figure 5-13: Fringe plot of the effective plastic strain on hardened 4340 Steel (percentage of defects 0.5%) with 1 mm wall copper stopper tube at different stages of collapse (a) 5 μs (b) 7.88 μs (same effective strain as Fig. 12(b)) (c) 10 μs. Outer diameters in (a) 15.71 mm, in (b) 14.22 mm and in (c) 13.28 mm.

We also observe that changes in the shear band pattern in the numerical calculations for hardened samples are similar to those observed in experiments (compare Figs. 13 and 4(a)). But in numerical calculations shear bands

propagating through the whole sample have been formed more uniformly through the sample bulk in both directions compared to the ones observed in the experiment. The possible ex- planation can be a slight asymmetry of the collapse in experiments and fast growth of individual shear bands that arrest development of more symmetric shear band patterns that are observed in numerical calculations.

If we measure the spacing between bands considering the bands that have reached or almost reached the outer surface in Figs. 12(b) and 13(b), we obtain a spacing approximately equal to 1.1 mm. The main difference between AISI 4340 as-received vs. hardened specimen was observed in their post-critical behavior. The results of numerical cal- culations coincide with catastrophic failure observed in experiments (compare Figs. 13 and 4(a)). It should be mentioned that Figs. 13(c) and 14(c) correspond to the final stage of the simulation; the boundary conditions were imposed such that the complete collapse of the specimen would take about 10 μs.

Fig. 14 presents the case of large global strain (0.5 mm wall thick- ness copper stopper), which corresponds to experimental results de- picted in Fig. 4(b). The number and location of the initial defects in- troduced in the calculations are identical to the ones corresponding to the smaller global strain (Fig. 12(b)).

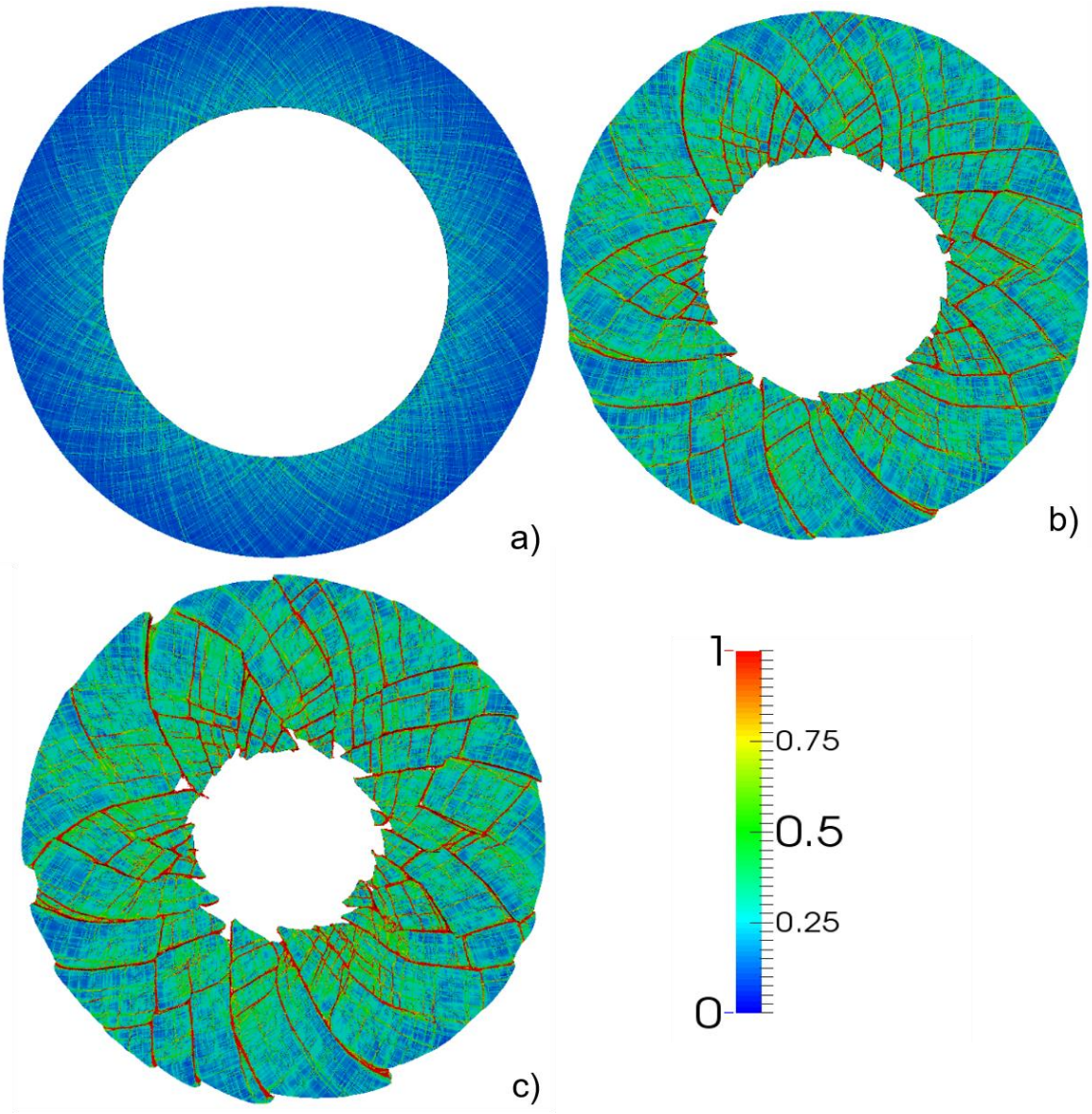

Figure 5-14: Fringe plot of the effective plastic strain on hardened 4340 Steel (0.5% defects) with 0.5 mm wall copper stopper tube at different times (a) 5 μs (b) 8.74 μs (same effective strain as Fig. 10(b)) (c) 10 μs. Outer diameters in (a) 15.58 mm, in (b) 13.44 mm and in (c) 12.7 mm.

As in the case of the small global strain, the number of observed shear bands is larger than observed in the experiments. The number of shear bands formed at earlier stages are similar to the number of shear bands in the later stages.

Thus, initially created shear bands are able to accommodate the global shear strains without generation of additional shear bands (Figs. 13 vs. 14). This means that shear bands formed at small strains dominate the final stage of collapse and post-critical behavior similar to that observed for other materials in [21]. At the same time, some shear bands in the numerical calculations propagated faster, arresting development of the neighboring shear bands and breaking a symmetric pattern on the earlier stages of collapse (Fig. 14(b)). It is important to remark that even if shear bands resulted in fracture, no preferential direction of the shear bands can be observed.

In experiments (Fig. 4) and in numerical simulations (Figs. 13, 14), corresponding to the hardened 4340 steel, secondary bands were ob- served on the post-critical stage of sample deformation probably due to violent bending of dislodged material pieces between the original shear bands. The fact that we observed it only in hardened 4340 is probably due to its lower ductility than in as-received 4340 and in other in- vestigated ductile materials, e.g., in [13,20–22]. The generation of additional damage due to bending on post-critical stages of collapsing SiC cylinders with the pattern of shear bands was reported in paper [56].

5.4 Chapter conclusions

The role of the initial microstructure, resulting in different microhardness and ductility on shear band patterning in AISI 4340 steel in the plane strain geometry of the TWC method was investigated at practically identical conditions of dynamic

deformation. It was observed that the initial hardening dramatically changes the nucleation and pattern of developed shear bands in the post-critical stage in AISI 4340 steel, mostly due to the change of material properties. The softening mechanism in both materials is probably caused by microcracking at interfaces of inclusions with the matrix. The hardening due to heat treatment of 4340 steel results in the dramatic difference in the pattern of shear bands because the initial stage of their nucleation is sensitive to material properties. A well-developed pattern of shear bands results in the reduced ability to dissipate energy on post-critical stages of high strain deformation due to low shear strength within them. Numerical modeling in the framework of the Johnson-Cook model with damage incorporating the random distribution of initial defects (by random scaling of initial yield strength in some elements) reproduced most qualitative features of the shear band patterning and its change with variation of the initial properties of materials. It is important that the material parameters of both steels were taken from independent experiments. The only fitting variable was the initial concentration of defects randomly distributed through the steel specimens modeled by mesh elements having a different initial yield strength scaled by the nominal yield strength.

The presented models verified in the experiments can be used to describe post-critical behavior of AISI 4340 steel with different initial microstructures at other dynamic conditions of loading, e.g., in target or penetrator deformation and fragmentation or in machining.

5.5 Chapter references

[1] Dodd B, Bai Y. Adiabatic shear localization: frontiers and advances eds Elsevier; 2012.

[2] Wright TW. The physics and mathematics of adiabatic shear bands. Cambridge University Press; 2002.

[3] Miguélez MH, Soldani X, Molinari A. Analysis of adiabatic shear banding in orthogonal cutting of Ti alloy. Int J Mech Sci 2013;75:212–22.

[4] Nesterenko VF. Dynamics of heterogeneous materials. Springer Science & Business Media; 2013 Chapter 4.

[5] Walley SM. Shear localization: a historical overview. Metall Mater Trans A 2007;38(11):2629–54.

[6] Zener C, Hollomon JH. Effect of strain rate upon plastic flow of steel. J Appl Phys 1944;15(1):22–32.

[7] Dodd B, Walley SM, Yang R, Nesterenko VF. Major steps in the discovery of adiabatic shear bands. Metall Mater Trans A 2015;46(10):4454–8.

[8] Kravz-Tarnavskii VP. A peculiar band discovered in steel. J Russ Metall Soc 1928;3:162–7. in Russian, (English translation of this paper can be found in Dodd B, Walley SM, Yang R, Nesterenko VF., Major steps in the discovery of adiabatic shear bands). http://arxiv.org/abs/1410.1353.

[9] Davidenkov N, Mirolubov I. Eine besondere art der stauchdeformation von stahl: Der krawz-tarnawskij effekt. Tech Phys USSR 1935;2:281–98. in German (English translation of this paper can be found in Dodd B, Walley SM, Yang R, Nesterenko VF. Major steps in the discovery of adiabatic shear bands). http://arxiv.org/abs/1410.1353.

[10] Nesterenko VF, Lazaridi AN, Pershin SA. Localization of deformation in copper by explosive compression of hollow cylinders. Fiz. Goreniya Vzryva 1989;25(4):154–5.

[11] Nesterenko VF, Bondar' MP. Localization of deformation in collapse of a thick walled cylinder. Combust Explosion Shock Waves 1994;30(4):500–9.

[12] Nesterenko VF, Bondar' MP. Investigation of deformation localization by the “thick- walled cylinder” method. DYMAT J 1994;1(3):245–51.

[13] Xue Q, Nesterenko VF, Meyers MA. Evaluation of the collapsing thick-walled cylinder technique for shear band spacing. Int J Impact Eng 2003;28(3):257–80.

[14] Nesterenko VF, Meyers MA, Chen HC, LaSalvia JC. Controlled high-rate localized shear in porous reactive media

[15] Chiu PH, Olney KL, Higgins A, Serge M, Benson DJ, Nesterenko VF. The mechanism of instability and localized reaction in the explosively driven collapse of thick walled Ni-Al laminate cylinders. Appl Phys Lett 2013;102(24):241912.

[16] Olney KL, Chiu PH, Ribero Vairo MS, Higgins A, Serge M, Benson DJ, and Nesterenko, V.F., Influence of mesoscale properties on the mechanisms of plastic strain accommodation in plane strain dynamic deformation of concentric Ni-Al laminates. J. Appl. Phys. 2015;117(4):044302.

[17] Yang Y, Zheng HG, Shi ZJ, Zhang QM. Effect of orientation on self-organization of shear bands in 7075 aluminum alloy. Mater Sci Eng A 2011;528(6):2446–53.

[18] Yang Y, Zheng HG, Zhao ZD, Zhang Q, Zhang QM, Jiang F, et al. Effect of phase composition on self-organization of shear bands in Ti-1300 titanium alloy. Mater Sci Eng A 2011;528(25):7506–13.

[19] Stokes JL, Nesterenko VF, Shlachter JS, Fulton RD, Indrakanti SS, Gu YaBei. Comparative behavior of Ti and stainless steel in a magnetically-driven implosion at the Pegasus-II Facility. In: Staudhammer KP, Murr LE, Meyers MA, editors. Proceedings of International Conference on Fundamental Issues and Applications of Shock-Wave and High-Strain-Rate Phenomena. Elsevier; 2001. p. 585–92.

[20] Lovinger Z, Rikanati A, Rosenberg Z, Rittel D. Electro-magnetic collapse of thick- walled cylinders to investigate spontaneous shear localization. Int J Impact Eng 2011;38:918–29.

[21] Lovinger Z, Rittel D, Rosenberg Z. An experimental study on spontaneous adiabatic shear band formation in electro-magnetically collapsing cylinders. J Mech Phys Solids 2015;79:134–56.

[22] Lovinger Z, Rittel D, Rosenberg Z. Modeling spontaneous adiabatic shear band formation in electro-magnetically collapsing thick-walled cylinders. Mech Mater 2017. (in press). https://doi.org/10.1016/j.mechmat.2017.01.010.

[23] Dong XL, Li LZ, Fu YQ, Zhou FH. A FEM study on adiabatic shear band formation in tube compression driven by electro-magnetic loading. Appl Mech Mater 2014;566:517–21.

[24] Cai J, Nesterenko VF. Collapse of hollow cylinders of PTFE and its mixtures with metal particles using hopkinson bar, in shock compression of condensed matter -2005, Proceedings of the Conference of the American Physical Society Topical Group on Shock Compression of Condensed Matter, AIP Conference Proceedings 845, edited by M.D. Furnish, M. Elert, T.P. Russel, and C.T. White, American Institute of Physics, Melville, New York, pp. 793–796, 2006.

[25] Winter RE, Stirk SM, Harris EJ, Chapman DJ, Eakins DE. A technique for studying the response of materials to high rate, high strain deformation. Int J Impact Eng 2016;97:116–26.

[26] Grady DE, Kipp ME. The growth of unstable thermoplastic shear with application to steady-wave shock compression in solids. J Mech Phys Solids 1987;35(1):95–119.

[27] Grady DE, Asay JR, Rohde RW, Wise JL. Microstructure and mechanical properties of precipitation hardened aluminum under high rate deformation. Material behavior under high stress and ultrahigh loading rates. Springer US; 1983. p. 81–100.

[28] Wright TW, Ockendon H. A scaling law for the effect of inertia on the formation of adiabatic shear bands. Int J Plasticity 1996;12(7):927–34.

[29] Molinari A. Collective behavior and spacing of adiabatic shear bands. J Mech Phys Solids 1997;45(9):1551–75.

[30] Liu M, Guo Z, Fan C, Tang T, Wang X, Hu H. Modeling spontaneous shear bands evolution in thick-walled cylinders subjected to external high-strain-rate loading. Int J Solids Struct 2016;97:336–54.

[31] Rabczuk T, Areias PMA, Belytschko T. A simplified mesh-free method for shear bands with cohesive surfaces. Int J Numerical Methods Eng 2007;69(5):993–1021.

[32] Zhou F, Wright TW, Ramesh KT. A numerical methodology for investigating the formation of adiabatic shear bands. J Mech Phys Solids 2006;54(5):904–26.

[33] Zhou F, Wright TW, Ramesh KT. The formation of multiple adiabatic shear bands. J Mech Phys Solids 2006;54(7):1376–400.

[34] Tan ZH, Han X, Zhang W, Luo SH. An investigation on failure mechanisms of ceramic/metal armour subjected to the impact of tungsten projectile. Int. J. Impact Eng. 2010;37(12):1162–9.

[35] Frew DJ, Hanchak SJ, Green ML, Forrestal MJ. Penetration of concrete targets with ogive-nose steel rods. Int J Impact Eng 1998;21(6):489–97.

[36] Littlefield DL, Anderson CE, Partom Y, Bless SJ. The penetration of steel targets finite in radial extent. Int J Impact Eng 1997;19(1):49–62.

[37] Schroeder T, Hazra J, von Turkovich BF, Flom DG. On the catastrophic shear instability in high-speed machining of an AISI 4340 steel. J Eng Ind 1982;104:121–31.

[38] Hou ZB, Komanduri R. Modeling of thermomechanical shear instability in machining. Int J Mech Sci 1997;39(11):1273–314.

[39] Guo YB, Yen DW. A FEM study on mechanisms of discontinuous chip formation in hard machining. J Mater Process Technol 2004;155:1350–6

[40] Lee WS, Yeh GW. The plastic deformation behaviour of AISI 4340 alloy steel subjected to high temperature and high strain rate loading conditions. J Mater Process Technol 1997;71(2):224–34.

[41] Wittman CL, Meyers MA, Pak HR. Observation of an adiabatic shear band in AISI 4340 steel by high-voltage transmission electron microscopy. Metall Trans A 1990;21(2):707–16.

[42] Mason C, Worswick MJ. Adiabatic shear in annealed and shock-hardened iron and in quenched and tempered 4340 steel. Int J Fracture 2001;111(1):29–51.

[43] Odeshi AG, Bassim MN, Al-Ameeri S, Li Q. Dynamic shear band propagation and failure in AISI 4340 steel. J Mater Process Technol 2005;169(2):150–5.

[44] Owolabi G, Odoh D, Odeshi A, Whitworth H. Occurrence of dynamic shear bands in AISI 4340 steel under impact loads. World J Mech 2013;3:139–45.

[45] Lee WS, Yeh GW. The plastic deformation behavior of AISI 4340 alloy steel subjected to high temperature and high strain rate loading conditions. J Mater Process Technol 1997;71(2):224–34.

[46] Yiadom SB, Khan AK. Bassim, Effect of microstructure on the nucleation and initiation of adiabatic shear bands (ASBs) during impact. Mater Sci Eng A 2014;615:373–94.

[47] Washko SD, Aggen G. Wrought stainless steels. 10th ASM international 1. Metals Handbook; 1990. p. 841–907.

[48] Zurek AK. The study of adiabatic shear band instability in a pearlitic 4340 steel using a dynamic punch test. Metall Mater Trans A 1994;25:2483–9.

[49] Meyers MA, Wittman CL. Effect of metallurgical parameters on shear band formation in low-carbon (~0.20 Wt Pct) steels. Metall Trans A 1990;21:3153–64.

[50] Antolovich SD, Armstrong RW. Plastic strain localization in metals: origins and consequences. Progress Mater Sci 2014;59:1–160.

[51] Cox TB, Low Jr JR. An investigation of the plastic fracture of AISI 4340 and 18 Nickel–200 grade maraging steels. Metal Trans 1974;5:1457–70.

[52] Bassim MN, Odeshi AG. Shear strain localization and fracture in high strength structural materials. Archives Mater Sci 2008;70:69–74.

[53] Barry J, Byrne G. TEM study on the surface white layer in two turned hardened steels. Mater Sci Eng Struct Mater Properties Microstruct Process 2002;325(12):356–64.

[54] Johnson GR, Cook WH. Fracture characteristics of three metals subjected to various strains, strain rates, temperatures and pressures. Eng Fracture Mech 1985;21(1):31–48.

[55] Gray GT, Chen SR, Wright W, Lopez MF. Constitutive equations for annealed metals under compression at high strain rates and high temperatures. Los Alamos National Laboratory 1994. LA-12669-MS, Los Alamos.

[56] Shih CJ, Nesterenko VF, Meyers MA. High-strain-rate deformation and comminution of silicon carbide. J Appl Phys 1998;83(9):4660–71.

Chapter 5, in full, is a reprint of the material as it appears in International Journal of Impact Engineering, Franco Navarro, P., Chiu, P.H., Higgins, A., Serge, M., Benson, D.J. and Nesterenko, V.F., Elsevier 2018. The dissertation author was the primary investigator and author of this paper.

Chapter 6 : Conclusions

Numerical simulations of diverse dynamic events of heterogeneous materials, such as impact loading of an Al-W laminate and Thick-Walled Cylinder experiments of an Al-W granulate material as well as for 4340 steel with different microstructures were conducted to help explain the mechanisms of localization. Numerical simulations were compared to experimental results or developed phenomenological models when possible.

For the case of the Al-W laminate, numerical simulations revealed that a new qualitatively phenomenon of solitarylike waves, that arises from the balance of nonlinearities and dispersion, is possible when the duration of the loading pulse is comparable to the size of the unite cell in the laminate. These qualitatively new waves can be described by a phenomenological approach developed based on the weekly nonlinear Kortweg-de Vries equation. With the analytical solutions of the approach, important space scale characteristics of the wave can be approximated, and important information can be obtained, e.g. maximum amplitude, rise time and width of the wave. It was also demonstrated, that when the duration of a high amplitude loading pulse is much longer compared to the unit cell size, the resulting pulse in the laminate can be a train of solitarylike waves or a quasisteady shockwave. When the latter one is observed, the inclusion of a dissipative viscous term to the phenomenological model allows to determine characteristics of the quasisteady shock, such as the shock front width and period of oscillations behind the front.

The explosive collapse of Al-W granular material in Thick-Walled Cylinder experiments showed a stable cavity collapse within the explored grain sizes. Numerical simulations helped explore the influence of porosity and grain size in the stability of collapse. It was shown, that bigger grain sizes helped create kinks that promote instabilities of the collapsing cavity, these kinks seem to be the result of softer Al jetting through harder W particles. More importantly, fully dense samples showed the formation of strain localization that closely resemble shear bands. This strain localization is observed to occur mostly in the Al particles. Moreover, porous samples showed the advantage to delay the localization of strain in these shear instabilities.

Explosively driven Thick-Walled Cylinder tests in steel 4340 with different microstructures, revealed the importance of material microstructure in post-critical behavior. It was shown, that 4340 in as-received conditions was resilient to shear band formation, while the heat-treated sample catastrophically failed at same levers of global strain. The main cause appeared to be appearance of inclusions which promoted the concentration of strain and serving as nucleation sites for shear band formation. Numerical simulations showed that the proper consideration of these inclusions, coupled with right material constants are necessary for the reproduction of experimental results and that the development of complex failure criteria is not always necessary. These results can be used to help tune numerical simulations of projectile penetration or other shear intensive phenomena.